UNIVERSITÀ DEGLI STUDI DI BOLOGNA

FACOLTÀ DI SCIENZE MATEMATICHE FISICHE E NATURALI

ANNO ACCADEMICO 2006/2007

DOTTORATO DI RICERCA IN FISICA

XIX CICLO

IMPROVEMENTS AND CALIBRATIONS OF NUCLEAR TRACK DETECTORS FOR RARE PARTICLE SEARCHES AND FRAGMENTATION STUDIES

PRESENTED: SHAHID MANZOOR

SUPERVISORS:

PROF. GIORGIO GIACOMELLI

PROF. IMTINAN E. QURESHI

DOTT.SSA LAURA PATRIZII

COORDINATOR:

PROF. FABIO ORTOLANI

BOLOGNA, MARCH 2007

Dedication

This thesis is dedicated to my parents, to my wife Alia and to the two sweet daughters, Sidra and Areeba without whom none of this would have been even possible. It is also dedicated to those who speak the truth to power and make it their business to do so.

In remembrance to my late sweety, Yusho, She was my own ''soul out of my soul,'' you are always with me, please forgive me.....

Contents

1. Introduction

D.A. Young [1] was the first to observe tracks in LiF crystals. Later, Silk and Barnes [2] made direct observations of heavy charged particles tracks in mica using a transmission electron microscope. The pioneers in the nuclear track detector field, P. B. Price, R. M. Walker and R. L. Fleischer [3], made extensive developments of the technique, observing nuclear tracks in dielectric solid crystals, plastics and glasses. Because of their properties, like lightweight, large geometrical factor, simplicity, flexibility and the ability to discriminate against lightly ionizing particles, in certain fields of physics, these detectors have potential advantages over other detectors [4-8]. In NTDs, the path of an individual heavily ionizing charged particle is revealed by a suitable chemical etching of the damaged trail.

Cartwright et al, [9] first discovered the CR-39 polyallyldiglycol carbonate a NTD; CR stands for Columbia Resin. CR39 has the widest dynamic range for detecting charged particles for a large range of Z values, and from low energy protons to relativistic U ions. For the registration of heavy ions in a wide angular range, NTDs have marked advantages over other detectors. A single CR39 NTD can be used to detect nuclei in a wide range of charges down to $Z = 5e$, even in the relativistic energy region. This needs a carefully designed calibration procedure based on high energy heavy ions and their fragments. Tarlè et al. [10] demonstrated that for high Z nuclei CR39 has a charge resolution superior to scintillators, nuclear emulsions and ionization chambers of equivalent thickness. CR39 has an intrinsic charge resolution of $\sigma_z \sim 0.2 - 0.3$e on a single sheet diameter measurement [11]; the charge resolution can be improved to a value of $\sigma_z \sim 0.05$e by measuring the tracks on many sheets [12]. It should, however, be noted that the particle detection characteristics of CR-39 depend strongly on the etching and measuring procedures. NTDs should be carefully calibrated before using them for quantitative measurements.

CR39 and Makrofol NTDs have been used successfully for many years as charged particle detectors. The knowledge of the relationship between the response of the detectors and the energy deposition by a charged particle is important to fully characterise the particle registration process that takes place in the detector. The dynamics of nuclear track formation in polymers is quite complex and depends on the charge and energy of the incident particles. Benton proposed the Restricted Energy Loss (REL) model to explain the formation of the track core of relativistic high and low energy heavy ions; it uses a cut-off delta ray energy (200 eV for CR39 and 350 eV for Makrofol), considering that the outer part of the track does not take part in the etching process and does not contribute to the track formation [13].

The study of the fragmentation properties of high energy atomic nuclei is of relevance for nuclear physics, cosmic ray physics and astrophysics. For instance, fragmentation cross sections are needed to evaluate the changes in composition undergone by cosmic ray particles in the collisions with the interstellar medium.

The fragmentation of relativistic heavy ions from accelerators has been studied by many research groups using NTDs [14-18]. Several heavy ion experiments at relativistic energies have been performed with Si (14.6A GeV/c) and Au (11.6A GeV/c) ions at the BNL-AGS and with O (200A GeV/c), S (200A GeV/c) and Pb (158A GeV/c) ions at the CERN-SPS.

Heavy ion reactions like relativistic Pb^{82+} in different targets are of great interest since various reaction products covering a wide range of mass and charge are emitted after the fragmentation of beam ions. Experimental studies of energetic Fe^{26+} ions are of interest for space radiation research, especially to quantify the risk related to the exposure to the galactic cosmic radiation [34-38]. The reactions of light ion beams C^{6+}, Si^{14+} with light targets like CH_2 offer favourable conditions for the study of fragmentation in the treatment of deep-seated tumours in cancer therapy [39-40]. Thus, fragmentation processes of atomic nuclei induced by energetic ions have recently been getting more attention then ever.

The response of NTDs exposed to a wide spectrum of charges and energies has been established in many papers [7, 12, 18]. The major focus in this work lies in the

identification of charged fragments produces in the collisions of relativistic heavy ions with thick targets. Such identification leads to the determination of the total and partial charge-changing fragmentation cross sections, useful for applications in different disciplines [18-24].

H. Dreschel et al. [25] used NTDs as targets and detectors to measure the mean free path of relativistic heavy ions. A. Noll and collaborators [26-27] developed an automatic scanning system for applications in high energy heavy ions for calibrating NTDs, for measuring the total and partial charge changing fragmentation cross section relevant in nuclear and cosmic ray physics, and for radiobiological studies [28-30]. Westphal et al. used BP-1 glass detectors calibrated with relativistic gold and lead beams (the detector provided charge resolutions of $0.3 < \sigma_z < 0.4$) for the analysis of cosmic ray composition [31-33].

In this thesis, after a theoretical introduction, I shall first discuss the improvements made on etching and measuring methods for CR39 and Makrofol nuclear track detectors. Then their calibrations performed with different ions of different energies are considered in detail.

The use of CR39 and Makrofol detectors in the search for intermediate mass magnetic monopoles, nuclearites and q-balls in a large area experiment at high altitudes (SLIM) is then discussed, and strong limits are presented. Finally the measurements of the fragmentation cross sections of different ions of various energies in different targets are considered and the results obtained are discussed.

2. Nuclear Track Detectors

2.1 Introduction

When an ion crosses a nuclear track detector foil, it produces damages at the level of molecular bonds (~ few tens of nm) along its trajectory, as a result of the excitation and ionization of atoms, forming the so called “latent track”. In crystals, the latent tracks consist of atomic displacements whereas in plastic materials the damage is due to broken molecular chains which produce free radicals (see Fig. 2.1). By a suitable chemical etching of the detector, etch-pit cones are formed.

A charged particle can transfer its energy to the insulating material in the following ways

- Ionization and excitation of the material atoms and molecules by electron displacements
- A nuclear interaction elastic and inelastic with the target atoms causing recoil tracks

A suitable chemical solution enlarges latent tracks so as they can be seen under a laboratory optical microscope. This procedure is called ‘‘detector etching’’ or track visualization.

The most common etchants for plastics are aqueous solutions of NaOH or KOH with concentrations ranging from 1-12 N and temperatures in the range between 40-90 ^{o}C [3]. Somogyi et al., used the PEW (15 wt% KOH + 65 wt% C_2H_5OH + 20 wr% H_2O) solution as an etchant to reduce the threshold value of polycarbonate detectors (Lexan and Makrofol). They also observed that the addition of alcohol in an NaOH solution for CR39 the threshold increases [41-43]. Glasses, mica and minerals were mainly etched with 47% HF acid. Short etching times are

adequate for the observation of high REL particles and long etching times are required for low REL particles [44].

CR39 NTDs were successfully applied to observe nuclei with Z/β values from 5 to 83 [7-8]. The sensitivity, resolution and optical properties of CR39 are the best among other track recording detectors. Even after dissolving 500 μm thickness by etching, the surface of the detector remains smooth. It is widely used in heavy ion research, e.g. composition of cosmic rays, heavy ion nuclear reactions, radiation dose due to heavy particles, explorations of extra heavy elements and search for magnetic monopoles, etc.

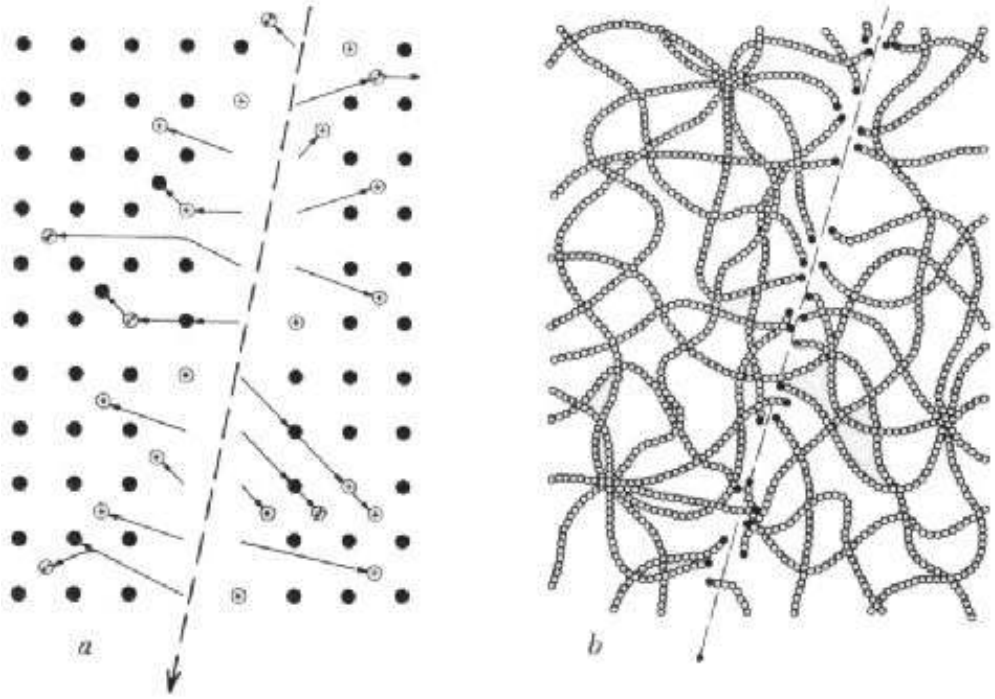

Fig. 2.1 A latent track is formed in (a) inorganic solids by the ionization and production of dense positive ions along the ion path and (b) the breakage of polymeric chains by the passage of charged particle.

CR39 ®		**MAKROFOL ®**
Poly-allyl-diglycol-carbonate		Polycarbonate films
Composition:	$C_{12}H_{18}O_7$	$C_{16}H_{14}O_3$
Density:	1.32 (g cm^{-3})	1.29 (g cm^{-3})
Refrective index (η):	1.504	1.584
High light transmission,		High light transmission
		High surface uniformity

Table 2.1 Etching conditions for some commonly used nuclear track detector.

Material	Etching Condition	Time	
Crystals:			
gadolinium gallium garnet	25% HNO_3/25% CH_3COOH/50% H_2O	70°C	30 min
muscovite mica	48% HF	20°C	20 min
quartz	(a) KOH (aq)	150°C	3 h
	(b) 48% HF	23°C	24 h
Glasses:			
lead phosphate glass	1 ml 70% HNO_3/3 ml H_2O		2–20 min
phosphate glass	48% HF		5–20 min
quartz glass	48% HF		1 min
soda lime glass	(a) 48% HF		5 s
	(b) 24% HBF_4/5% HNO_3/0.5% acetic acid		1 h
Polymers:			
allyl diglycol carbonate	NaOH,KOH ≤ 40%	≤ 70°C	
cellulose acetate	1 ml 15% NaClO/2 ml 6.25*N* NaOH	40°C	1 h
cellulose acetate butyrate	6.25*N* NaOH	70°C	12 min
cellulose nitrate	≤ 16*N* LiOH,NaOH,KOH	≤ 50°C	≤ 6 h
polyamide	(a)$KMnO_4$ (25% aq)	100°C	1.5 h
	(b)6*N* NaOH		
polycarbonate	6.25*N* NaOH	50°C	20 min
polyethylene terephtalate	6.25*N* NaOH	70°C	10 min
polyimide	$KMnO_4$ in H_2O		
polystyrene	(a) sat. $KMnO_4$	85°C	2.5 h
	(b) 10 g $K_2Cr_2O_7$/35 ml 30% H_2SO_4	85°C	3 h
polyvinylidene fluoride	5–12*N* NaOH	65–85°C	≤ 100 h

Makrofol polycarbonates manufactured by a casting process into the form of thin sheets by Bayer AG of Leverkussen, West Germany, have the same chemical composition ($C_{16}H_{14}O_3$) as Lexan, a polycarbonate manufactured by the General Electric Co. of USA. The shape of tracks produced by heavy ions and fission fragments in Makrofol are needle like with a slight spread towards their tail. They also offer a very convenient way of detecting heavy ions in the study of the

composition of very heavy cosmic rays, heavy ion nuclear reactions, exploration of super heavy elements, etc.

The shape of an etched track in a certain NTD depends on the charge, mass and velocity of the incident particle and also on the track detection conditions, the type of chemical solution, normality and temperature of the etchant. A comprehensive summary of the materials that show the track effect is given in Table 1 [45].

2.2 Track Registration Mechanisms

Many track registration criteria have been proposed for the formation of an etchable latent track in the detector material, which mainly depends on the charge, mass and velocity of the incoming particle plus the detector characteristics i.e. the density and chemical composition. Here we quote briefly only three of them.

2.2.1 Total Energy Loss (dE/dx)

According to this criterion the formation of an etchabale track is possible if the total energy loss $(dE/dx)_{>critical}$ exceeds a certain critical value which depends on the detector material. Fleischer et al., [46], first proposed it; they used different projectiles having different Z/β values in mica and polycarbonate detectors. The criterion explains the track formation for low energy ions but at high energy it seems to fail to reproduce some experimental data. The main shortcoming of this criterion is that it neglects the primary ionization for the track formation.

The total energy loss is given by [46]

$$\frac{dE}{dx} = 4\pi N_A m_e c^2 r_e^2 \frac{Z_2}{A_2}\frac{Z_1^2}{\beta^2}\left[\ln\left(\frac{2m_e c^2\beta^2\gamma^2}{I}\right) - \beta^2 - \frac{\delta}{2} + \Delta L\right] \qquad (2.1)$$

where

N_A = Avogadro's number

r_e = classical electron radius

Z_2 = Target atomic number

A_2 = target mass number

I = mean ionization potential of the target material

Z_1 = effective charge of the incident ions; $Z_1 = Z_1\left[1 - \exp\left(-130\beta / Z_1^{2/3}\right)\right]$

δ = correction for the density effect

ΔL = sum of corrections needed for precision measurements

2.2.2 Primary Ionization loss (J)

A new criterion was proposed by Fleischer et al., [47]: the δ-rays are produced directly by the incident ion and this is based on the ion explosion spike model. The material can record an etchable track only if the linear ion density produced by the primary particle along its trajectory is greater than a critical value for that material. The primary ionization (dJ/dx) is given by [47]

$$\frac{dJ}{dx} = 2\pi N_A m_e c^2 r_e^2 \frac{Z_2}{A_2}\frac{Z_1^2}{\beta^2}\frac{f_{outer}}{I_{outer}}\left[\ln\left(\frac{2m_e c^2\beta^2\gamma^2}{I_{outer}}\right) - \beta^2 - \delta + K\right] \qquad (2.2)$$

where

I_{outer} = binding energy of the outermost electron (~2 eV)

f_{outer} = fraction of electrons in the outer state (0.05)

K = constant for target properties (3.04)

The other quantities have the same meaning as in eq. (2.1). Primary ionization fits the experimental data for heavy ions, but it is subjected to the following criticisms:

- It does not take into account the primary ionization for the emission of very low energy δ-rays.
- The value $I_{outer} \simeq 2$ eV may be sufficient to excite the atoms but not enough to ionize the atoms. To ionize an atoms one needs about 10-15 eV.

- The model neglects the higher order of ionization produced by the δ-rays (which is controversial).

2.2.3 Restricted Energy Loss (REL)

Benton et al., [13] proposed in 1955 that only the δ-rays emitted with an energy less than a value ω_o contribute to the track formation. An etchable track is formed only if the REL exceeds a critical value of the detecting material. The REL (MeV cm^2 g^{-1}) is calculated as [13]

$$REL = \left(\frac{dE}{dx}\right)_{\omega<\omega_o} = 4\pi N_A m_e c^2 r_e^2 \frac{Z_2}{A_2}\frac{Z_1^2}{\beta^2}\left[\ln\left(\frac{2m_e c^2\beta^2\gamma^2\omega_o}{I^2}\right) - \beta^2 - \frac{\delta}{2}\right] \qquad (2.3)$$

where

ω_o = the energy cut-off value; $\simeq$ 200 eV in CR39 and $\simeq$ 350 eV in Makrofol or Lexan. The other quantities have the same meaning as in eq. (2.1).

The REL model fits better the experimental data at low and relativistic energies for a wide range of incident ions [7, 8, 12].

2.3 Methodology of Track Detection and Visualization

2.3.1 Track detection

The latent damage trail formed in NTDs may be enlarged and detected by preferential chemical etching or electrochemical etching.

The shape of a track formed by a charged particle is governed by the simultaneous actions of the etchant along the latent track and on the bulk material. A schematic diagram of chemical etching of a charged particle in a NTD is shown in Figure 2.1. For reproducibility of results, the quality of etchant should be controlled

carefully: fresh etchants and uniform stirring should be used to avoid deposits of etch products on the detector surface and in its build up inside the solution [48-49].

2.3.2 Bulk etch rate (v_B)

The bulk etch rate v_B is defined as the rate at which the undamaged material of the detector is etched out. It depends on the types of the etching condition; it may vary with depth below the original surface.

Generally, the following techniques are employed for the measurement of the bulk etch rate of the detector:

i. Thickness measurement method
ii. Track diameter method
iii. Change in detector mass method

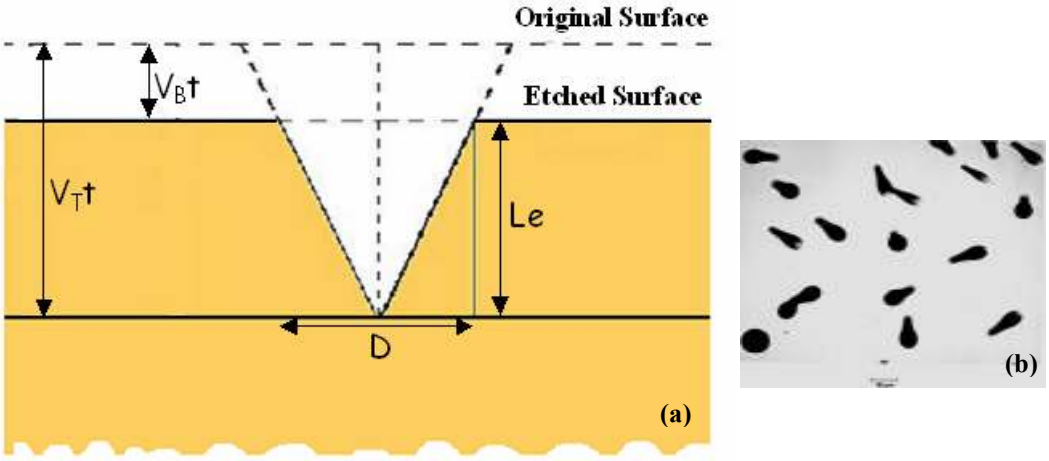

Fig. 2.2 (a) Sketch of a NTD track and (b) etched α tracks in a CR39 detector.

2.3.2.1 Thickness measurement method

For the determination of v_B the thickness of the detector is measured in selected points. The detector is then etched for fixed intervals of time Δt and the thickness is measured after each successive etching step. The bulk etch rate is given by

$$v_B = \Delta x / 2\Delta t \tag{2.4}$$

where Δx is the thickness variation after etching time Δt. It is assumed that the bulk etching is the same on both sides of the detector. By plotting Δx as a function of etching time t and by a given it of the data points the bulk etch rate can be determined.

2.3.2.2 Track diameter measurement method

If $v_T/v_B >> 1$ as in the case of fission fragments from a ^{252}Cf source in CR39, the track diameter measurement technique can be applied for the determination of v_B as [44].

$$D_{ff} = 2h\sqrt{\frac{p-1}{p+1}} \tag{2.5}$$

where D_{ff} is the diameter of fission fragments, $p = v_T/v_B$ and h is the thickness removed from both sides of the detector during an etching time t. If $p >> 1$ the above eq. can be written as

$$D_{ff} \cong 2h \ (h = v_B t)$$

$$D_{ff} \cong 2\ v_B t$$

$$v_B = D_{ff}/2t \tag{2.6}$$

2.3.2.3 Mass Change method

The bulk etch rate may be determined from the change in the mass of the detector Δm before and after etching. From the measurements of Δm and the density of the detector material, v_B can be calculated as

$$v_B = \frac{\Delta m}{2A\rho t} \tag{2.7}$$

where A is the surface area, ρ is the density of the detector and t is the etching time. Care must be taken in determining Δm of the same relative humidity.

2.3.3 Track etch rate (v_T)

The track etch rate v_T is defined as the rate at which the detector material is chemically etched along the damage trail of the particle trajectory, i.e. as the rate at which the tip of the etch cone moves along the latent track during the etching process. The track etch rate depends on the energy loss of the incoming particle, the temperature and concentration of the etchant.

2.3.4 Critical angle of etching (θ_c) and registration efficiency (η)

Fig. 2.3a shows the trajectory of a charged particle incident at an angle θ with respect to the detector surface. After an etching time t, the etched track length along the particle trajectory is $v_T t$ and the thickness of the bulk material removed is $v_B t$; the trajectory is observed as an etched cone if the vertical component of $(v_T t)_\perp > v_B t$. For $(v_T t)_\perp = v_B t$ one has the critical angle θ_c; measured with respect to the detector surface. Particles incident with $\theta < \theta_c$ cannot be detected. θ_c is an important parameter for NTDs, since it is connected with the detector efficiency. The track registration efficiency existence strongly depends on the critical angle.

NTDs have low critical angles for high REL nuclei like fission fragments and large critical angles for low REL particles, like protons and low Z nuclei (for these in CR39 θ_c varies from 2^o to 5^o) [50, 51].

The track registration efficiency η of NTDs is defined as

$$\eta = 1 - \sin\theta_c \tag{2.8}$$

From this expression it is clear that for small critical angles one has large track registration efficiencies. High registration efficiencies (85-99%) are found for most plastic NTDs having critical angles of 2 - 5^o.

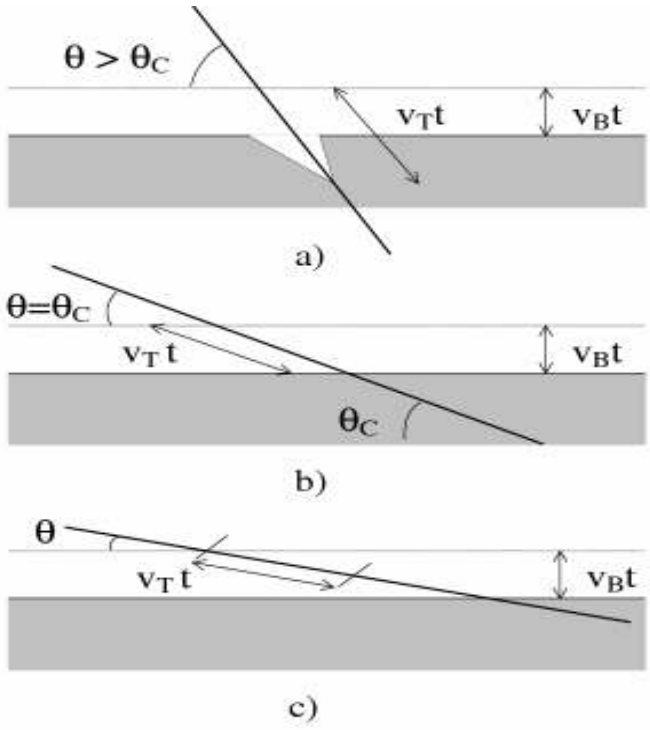

Fig. 2.3 Track geometry at different dip angle conditions: (a) formation of the post etched cone for a particle with an incident angle $\theta > \theta_c$ ($v_T t > v_B t$), (b) limiting case when the incident angle $\theta = \theta_c$ ($v_T t \geq v_B t$) and (c) no track is detected if the incident angle $\theta < \theta_c$ ($v_T t \leq v_B t$).

2.3.5 Track geometry at normal incidence

Fig. 2.4 shows the track geometry in NTDs for particles at normal incidence and constant REL: the basic quantities are the base cone diameter, major and minor axes, the cone height of the etched track, the "bulk" etch rate "v_B" and the track-etch rate v_T. The ratio of track-etch rate to bulk-etch rate is the "signal" or sensitivity "p" of the detector material ($p = v_T/v_B$). In general the chemical solution etches the surface of the detector material at a lower rate (v_B at both sides of the detector) compared to the damaged region where the etchant attacks at faster rate v_T. Since it is difficult to measure the track etch rate during etching, its value is determined from the geometry of an etch-pit [43].

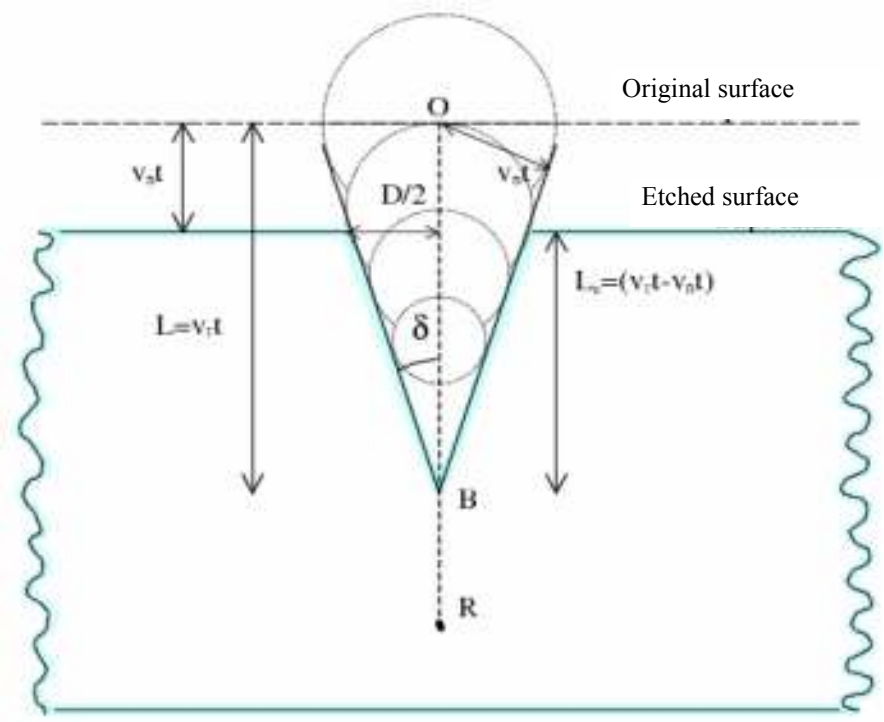

Fig. 2.4 Track geometry for a charged particle impinging at normal incidence in a nuclear track detector.

The following relations hold for normal incidence geometry (Fig. 2.4):

$$L_e = (v_T - v_B)t \tag{2.9}$$

$$v_B = \Delta x / 2\Delta t \tag{2.10}$$

The semi cone angle δ of the etched cone is

$$\sin\delta = \frac{v_B}{v_T} = \frac{1}{p} \tag{2.11}$$

From eq. 2.9 the track etch rate v_T is

$$v_T = v_B + \frac{L_e}{t} \tag{2.12}$$

The relations between 'D' 'v_T', 'v_B' and 'p' are

$$D = 2v_B t\sqrt{\frac{(v_T - v_B)}{(v_T + v_B)}} \tag{2.13}$$

$$p = \frac{1 + \left(D / 2v_B t\right)^2}{1 - \left(D / 2v_B t\right)^2} \tag{2.14}$$

$$p = \frac{1 + A/(\pi v_B^2 t^2)}{1 - A/(\pi v_B^2 t^2)} \tag{2.15}$$

The error on p can be calculated from the following relations

$$\Delta p = \frac{\Delta L_e}{v_B t}$$

$$\Delta p = \frac{D.\Delta D}{v_B^2 t^2 \left(1 - \frac{D^2}{4v_B^2 t^2}\right)^2} \tag{2.16}$$

$$\Delta p = \frac{2.\Delta A}{\pi v_B^2 t^2 \left(1 - \frac{A}{\pi v_B^2 t^2}\right)^2}$$

Eq. 2.9-2.15 are apply to any particle of constant energy loss such as relativistic ions, magnetic monopoles and nuclearites.

2.3.6 Track Geometry at Oblique Incidence

Fig. 2.5 shows the geometry of a particle incident at an angle θ w.r.t. the detector surface and constant REL. The following geometrical relations can be deduced from Fig. 2.5:

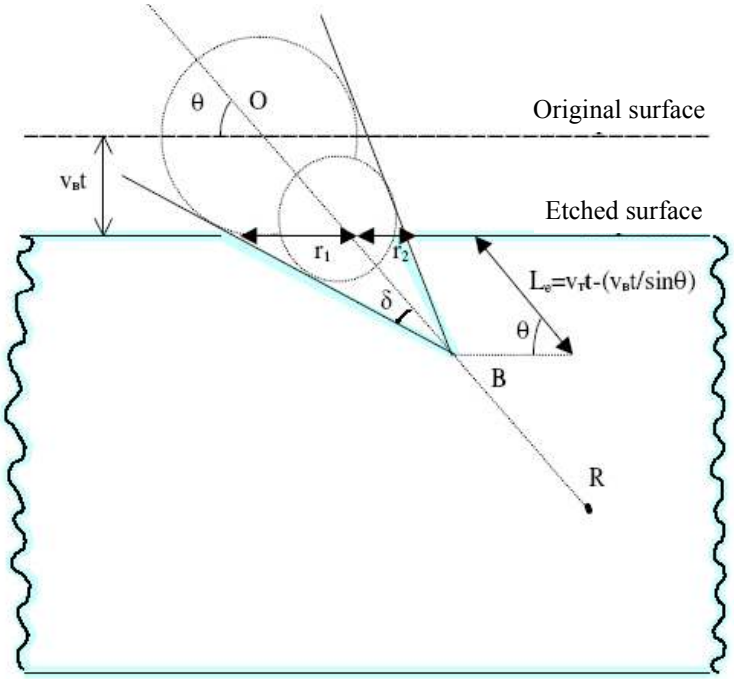

Fig. 2.5 Geometry of a particle incident at an angle θ with respect to the detector surface.

$$r1 = \frac{\tan\delta\left[v_T - v_B/\sin\theta\right]t}{\sin\theta - \cos\theta\tan\delta}$$
$$r2 = \frac{\tan\delta\left[v_T - v_B/\sin\theta\right]}{\sin\theta + \cos\theta\tan\delta} \tag{2.17}$$

From eq. (15) we deduce the relations for D, d and p,

$$D = 2v_B t\frac{\sqrt{\left(p^2-1\right)}}{\left(p\sin\theta+1\right)} \tag{2.18}$$

$$d = 2v_B t\sqrt{\frac{\left(p\sin\theta-1\right)}{p\sin\theta+1}} \tag{2.19}$$

$$p = \sqrt{1 + \frac{4A^2}{\left(1 - B^2\right)^2}} \tag{2.20}$$

where A = ($D/2v_Bt$) and B = ($d/2v_Bt$) and

$$\theta = \arcsin\left(\frac{1}{p} . \frac{1 + B^2}{1 - B^2}\right) \tag{2.21}$$

3. Magnetic Monopoles and Nuclearites

3.1 Magnetic Monopoles

In 1931, P.A.M. Dirac proposed that particles with magnetic charge could exist and that the existence of these particles would in turn imply quantization of electric charge [52]. He established a relation between the elementary electric charge 'e' and a basic magnetic charge 'g':

$$eg = n\hbar c/2 \tag{3.1}$$

$$\frac{ge}{\hbar c} = \frac{n}{2} \quad \Leftrightarrow \quad \frac{g}{e} = \frac{n}{2\alpha} \approx 68.5n$$

Dirac magnetic monopoles lose much energy in matter because of the large value of the charge 'g'; n is an integer, n = 1, 2, 3,…

There was no prediction for the MM mass; a rough estimate, obtained assuming that the classical monopole radius is equal to the classical electron radius, yields $m_M \simeq g^2 m_e / e^2 \simeq n\ 4700\ m_e \simeq n\ 2.4\ GeV/c^2$. From 1931 searches for "classical Dirac monopoles" were carried out at every new accelerator using simple setups, and recently also large collider detectors.

Electric charge is naturally quantized in Grand Unified Theories (GUT) of the basic interactions; they imply the existence of GUT monopoles with calculable properties. The MMs appear in the Early Universe at the phase transition corresponding to the breaking of the unified group into subgroups, one of which is U(1) [53]. The MM mass is related to the mass of the X, Y carriers of the unified interaction, $m_M \geq m_X/G$, where G is the dimensionless unified coupling constant at the energy $E \simeq m_X$. If $m_X \simeq 10^{14}$ - 10^{15} GeV and $G \simeq 0.025$, $m_M > 10^{16}$ - 10^{17} GeV.

This is an enormous mass: GUT MMs cannot be produced at any man made accelerator, existing or conceivable. They may have been produced only in the first instants of our Universe.

Intermediate Mass Monopoles (IMMs) with $m_M \sim 10^7 \div 10^{13}$ GeV may have been produced in later phase transitions in the early Universe and may be accelerated to relativistic velocities in one galactic coherent magnetic field domain. Relativistic IMMs could yield the highest energy cosmic rays [54-58].

The lowest mass MM is stable, since magnetic charge is conserved like electric charge. Thus the poles produced in the Early Universe should still exist as cosmic relics; their kinetic energy was affected by the Universe expansion and by travel through galactic and intergalactic magnetic fields. GUT poles are best searched for underground in the penetrating cosmic radiation (CR). IMMs may be searched for at high altitude laboratories.

3.1.1 Properties of Magnetic Monopoles

The main properties of MMs are obtained from the Dirac relation:

Magnetic Charge: If n =1 and the basic electric charge is that of the electron, then the basic magnetic charge is $g_D = \hbar c/2e = 137e/2$; the charge is larger if n > 1 and if the basic electric charge is e/3, see eq. 3.1.

Magnetic Coupling Constant: Similarly the fine structure constant, $\alpha = e^2/\hbar c \simeq 1/137$, the dimensionless magnetic coupling constant is obtained as $\alpha_g = g^2_D/\hbar c \simeq 34.25$.

Energy: In a magnetic field B, a MM can gain the energy $W = ng_D B\ell = n\ 20.5$ keV/G cm. In a coherent galactic length ($\ell \simeq 1$ kpc, $B \simeq 3\ \mu$G), the energy gained by a MM with $g = g_D$ is $W \simeq 1.8 \times 10^{11}$ GeV. Classical poles and IMMs in the CR may be accelerated to relativistic velocities.

Energy Losses of Fast MMs: A fast MM with magnetic charge g_D and velocity $v = \beta c$ behaves like an electric charge $(ze)_{eq} = g_D\beta$

Energy Losses of Slow MMs: ($10^{-4} < \beta < 10^{-2}$) MMs may lose energy by ionization or excitation of atoms and molecules of the medium ("electronic" energy loss) or to recoiling atoms or nuclei ("atomic" or "nuclear" energy loss). Electronic energy loss predominates for $\beta > 10^{-3}$.

Energy losses of very low velocities MMs: MMs with $v < 10^{-4}c$ may lose energy in elastic collisions with atoms or with nuclei. The energy is released to the medium in the form of elastic vibrations and/or infra–red radiation [59]. Fig. 3.1 shows the energy loss in liquid hydrogen of a $g = g_D$ MM vs β [55].

Energy Loss of MMs in Celestial Bodies: For $\beta < 10^{-4}$ the dE/dx in the Earth is due to pole-atom elastic scattering, eddy currents, and nuclear stopping power. MMs may be stopped by celestial bodies if they have velocities less than the escape velocity for:

Moon: $\beta \leq 5 \times 10^{-5}$, Earth: $\beta \leq 10^{-4}$, Sun: $\beta \leq 10^{-3}$.

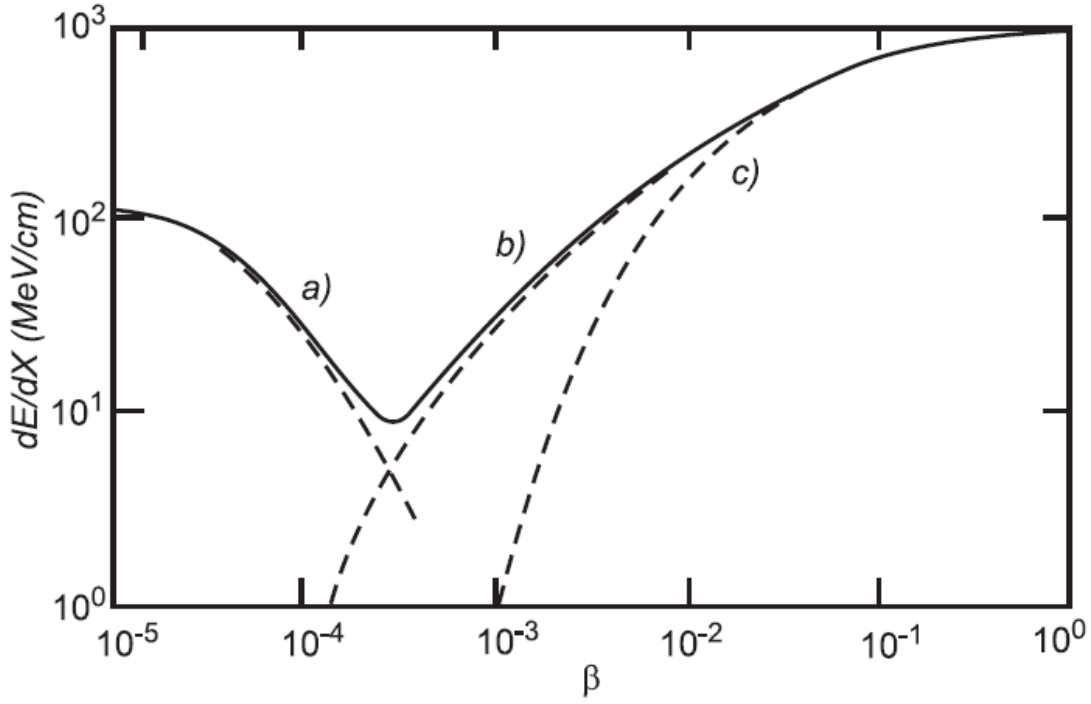

Fig. 3.1 The energy losses, in MeV/cm, of $g = g_D$ MMs in liquid hydrogen vs β. Curve a) corresponds to elastic monopole–hydrogen atom scattering; curve b) to interactions with level crossings; curve c) describes the ionization energy loss.

3.2 GUT Magnetic Monopoles

According to the standard model of the Big Bang, the Universe started as a very small size state of extremely high density and high temperature. As time progressed, the dimension of the Universe increased, the density and temperature decreased, while the particle composition changed. The Grand Unification of strong and electroweak interactions ended when the temperature dropped below ~10^{32} K (~10^{16} – 10^{17}GeV). At that moment, ~10^{-35}s after the Big Bang, the phase transition is thought to have occurred during which the GUT monopoles were created as topological defects.

The simplest GUT theories yield too many monopoles, while the inflationary scenario leads to a very small number of monopoles.

$$SU(5) \xrightarrow{10^{15}\,GeV} SU(3)\times(SU(2)_L \times U(1)_Y) \xrightarrow{10^{2}\,GeV} SU(3)_c \times U(1)_{em}$$

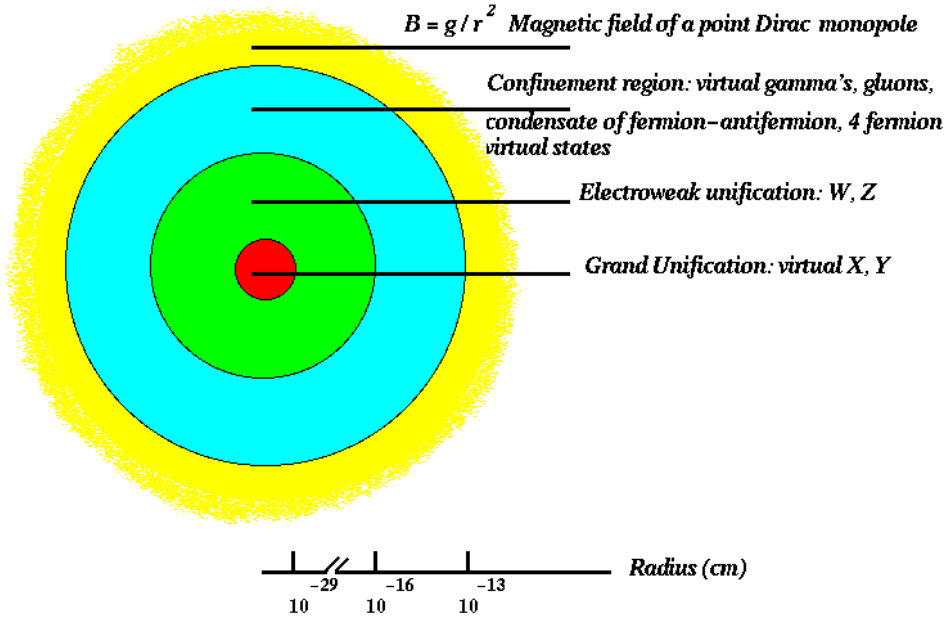

Fig. 3.2 *A massive GUT MM structure with different regions (for details see text).*

GUT MMs can be searched for as remnant particles in the penetrating cosmic radiation.

The spatial structure of a GUT pole (with $m_M \sim 10^{19}$ GeV) may be pictured as (see Fig. 3.2): i) a core with radius $r_c \approx 1/m_X \approx 10^{-29}$ cm, virtual X and Y particles are inside this region; ii) a region up to $r \approx 10^{-16}$ cm, where virtual W^+ , W^- and Z^0 may be present; iii) a confinement region with $r_{conf.} \approx 1$ fm; iv) a fermion–antifermion condensate region up to $r_f = 1/m_f$; the condensate may contain 4-fermion baryon number violating terms; v) for $r \geq 3$ fm a GUT MM behaves as a point particle which generates a field $B = g/r^2$.

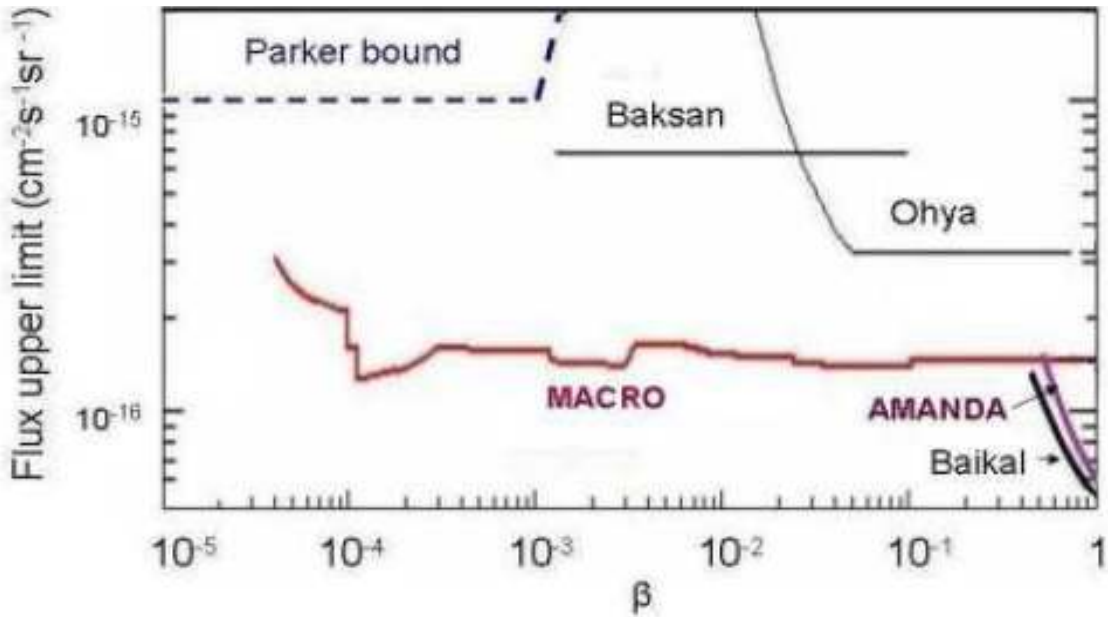

Fig. 3.3 The experimental 90% C.L. upper flux limits for magnetic monopoles obtained with MACRO electronic and passive detectors; also the results obtained by other experiments, are shown.

A flux of GUT MMs may reach the Earth with a velocity spectrum in the range $4 \times 10^{-5} < \beta < 0.1$, with possible peaks corresponding to the escape velocities of the Earth, Moon, Sun and the Galaxy. Searches have been performed for MMs in the

cosmic radiation with superconducting devices; a combined 90% C.L. upper limit (β independent) of 2 x 10^{-14} cm^{-2} s^{-1} sr^{-1} was achieved [5].

Many direct and indirect searches for GUT MMs have been made [65, 60-63], the flux upper limits obtained with different techniques are shown in Fig. 3.3. The MACRO detector has set the best limits, using three different types of detectors; the 90% C:L. flux upper limits are at the level of 1.4 x 10^{-16} cm^{-2} s^{-1} sr^{-1} for $\beta > 4$ x 10^{-5} [60]. The limits obtained from the Ohya [61], Baksan [62], Baikal and AMANDA [63] experiments are also shown. Fig. 3.4 shows the MACRO limits obtained using the CR39 NTDs [60].

Indirect GUT MM searches used ancient mica samples (high Z/β threshold). It is assumed that a MM passing through Earth captures an Al nucleus and drags it through subterranean mica causing a trail of lattice defects, which survive as long as the mica is not reheated. Few sheets of small sizes were analyzed (13.5 x 18 cm^2) which had an exposure time of 4÷9 x 10^8 years. They obtained a flux limit at the level of ~10^{-7} cm^{-2} s^{-1} sr^{-1} [64].

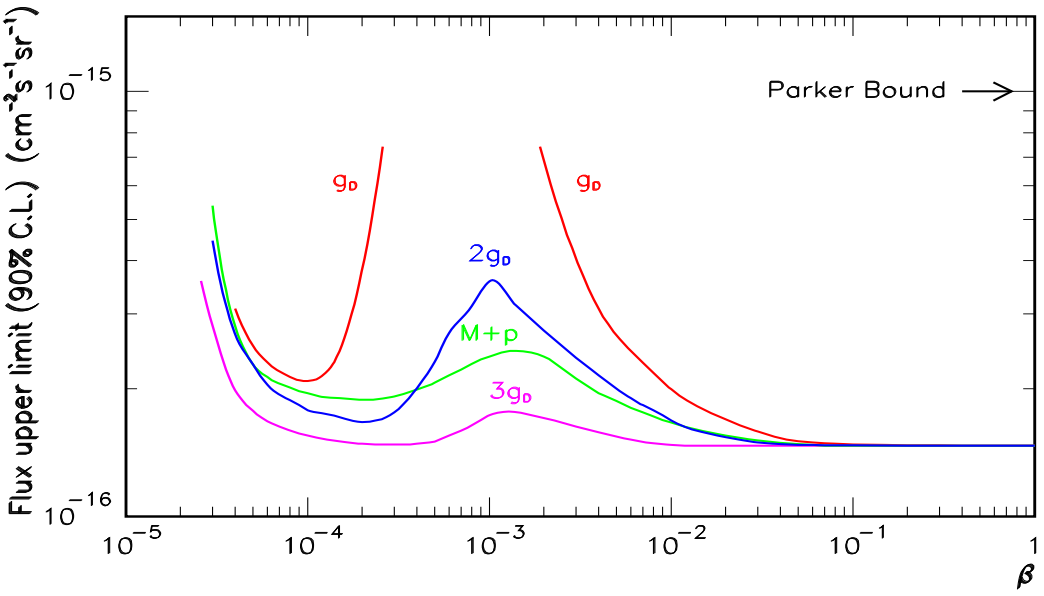

Fig. 3.4 90% C.L. flux upper limits obtained with the MACRO CR39 nuclear track detector for MMs with different magnetic charges, g =g_D, 2g_D, 3g_D and for M+p (dyon).

Detectors at the earth surface could detect the MMs coming from above with masses larger than 10^5 to 10^6 GeV [59]. Lower mass MMs can be detected with detectors installed at the high altitudes, with balloon experiments and in space. Few experimental results are available, The SLIM experiment will provide the best limits for the detections of IMMs for $g = g_D$ in the β range $4 \times 10^{-5} < \beta < 3 \times 10^{-}4$ and for $\beta > 2 \times 10^{-3}$, and for $g > 2g_D$ for all beta range.

3.3 Intermediate Mass Monopoles (IMMs)

IMMs with masses $10^5 - 10^{13}$ GeV may have been produced in later phase transition in the early Universe [65-66]. The IMMs may be accelerated to relativistic velocities by the galactic magnetic field in one coherent domain. The structure of a IMMs would be similar to that of a GUT monopole and is shown in Fig. 3.5, the core would be much larger (since $R \sim 1/m_M$) and the outer cloud would not contain 4-fermion baryon-number-violating terms.

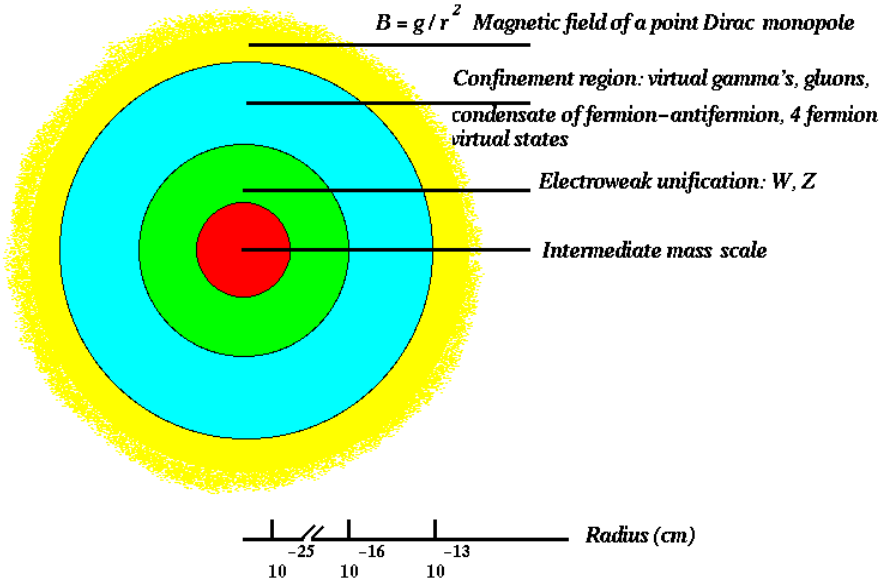

Fig. 3.5 *The different regions of an Intermediate mass monopole.*

3.4 Astrophysical and Cosmological Limits

Rough upper limits for a GUT monopole flux in the CR were obtained on the basis of cosmological and astrophysical considerations.

Mass Density Limit: Flux limits for GUT monopoles are obtained assuming that the magnetic monopoles are uniformely distributed in the universe and their mass density does not exceed to the critical mass density of the universe. For m_M $\sim 10^{17}$ GeV one has the limit:

$\Phi = \frac{n_M c}{4\pi} \beta < 3 \text{ x } 10^{-12} h_o^2 \beta \ (\text{cm}^{-2} s^{-1} sr^{-1})$. It is valid for poles uniformly distributed in the Universe. If poles are clustered in galaxies the limit is weaker [58].

Parker Limit: The ~3 μG magnetic field in our Galaxy is probably due to the non–uniform rotation of the Galaxy, which generates a field with a time–scale of the order of the rotation period of the Galaxy ($\tau \sim 10^8$ yr). An upper bound for the MM flux is obtained by requiring that the kinetic energy gained per unit time by MMs be less than the magnetic energy generated by the dynamo effect; one obtaines: $F < 10^{-15}$ cm^{-2} s^{-1} sr^{-1} [68]; taking into account the almost chaotic nature of the field, with domains of $\ell \sim$ 1 kpc, the limit becomes mass dependent [69]. An "extended Parker bound", obtained by considering the survival of an early seed field [68], yields $\Phi \sim 1.2 \times 10^{-16}$ ($m_M/10^{17}$GeV) cm^{-2} s^{-1} sr^{-1}.

3.5 Monopole Detectors

Monopole detectors are based on MM properties given by the Dirac relation.

Superconducting induction devices are sensitive to MMs of any velocity [57]. A moving MM induces in a ring an electromotive force and a current change (Δi). For a coil with N turns and inductance L, $\Delta i = 4\pi N n g_D / L = 2\Delta i_o$, where Δi_o is the current change corresponding to a change of one unit of the flux quantum of superconductivity. This method of detection is based only on the long–range

electromagnetic interaction between the magnetic charge and the macroscopic quantum state of a superconducting ring.

Scintillation counters for MMs have a threshold $\beta \sim 10^{-4}$, above which the light signal is larger than that of a minimum ionizing particle [59, 70].

Gaseous detectors of various types have been used. MACRO used a gas mixture of 73% helium and 27% n–pentane [70]. This allows exploitation of the Drell [71] and Penning effects [58]: a MM leaves a helium atom in a metastable state (He*) with excitation energy of ~20 eV, which is transferred as ionisation to a large organic molecule.

It was shown that both the electronic and the nuclear energy losses are effective in producing etchable tracks in the CR39 NTD [73]; CR39 allows to search for MMs with $g = g_D$ for β around 10^{-4} and $> 10^{-3}$, the whole β-range of $4 \times 10^{-5} < \beta < 1$ for MMs with $g \geq 2g_D$ [72]. The Lexan and Makrofol polycarbonates are sensitive for $Z/\beta \geq 50$ [73].

3.6 Interaction of Magnetic Monopoles with Matter

There is interest to know whether the quantity and quality of energy lost by magnetic monopoles in the detectors is adequate for their detection. Classical poles and IMMs can be accelerated to relativistic velocities. For such velocities the energy losses are $(g/e)^2 \simeq 4700$ times the energy loss of a minimum ionizing electric charge. Thus, the energy loss of a classical monopole would be enormous, more than enough to be easily detected with almost any kind of particle detectors. Instead GUT poles have large masses and are expected to have relatively low velocities, $10^{-4} < \beta < 10^{-1}$. The study of energy losses of slow moving monopoles is thus of great practical interest.

The interaction with matter of fast poles having velocities $> 10^{-2}$ c is well understood; a monopole with magnetic charge g behaves as an equivalent electric charge $(Ze)^2 = g^2 \beta^2$. The ionization energy losses may be described by the Bethe-

Bock formula as corrected by Ahlen [74, 75]; For an incoming particle with electric charge Ze one has

$$\left(\frac{dE}{dx}\right)_e = \frac{4\pi N_e Z^2 e^4}{m_e c^2 \beta^2}\left[\ln\frac{2m_e c^2 \beta^2 \gamma^2}{I_e} - \beta^2 - \delta_e/2 - B_e\right] \tag{3.2}$$

and for a magnetic monopole in a non conducting material

$$\left(\frac{dE}{dx}\right)_m = \frac{4\pi N_e g^2 e^2}{m_e c^2}\left[\ln\frac{2m_e c^2 \beta^2 \gamma^2}{I_m} - \frac{1}{2} + \frac{K_m}{2} - \delta_m/2 - B_m\right] \tag{3.3}$$

where $K_m = 0.406$ for poles with $g = g_D$ (0.346 for $g = 2g_D$), $\beta = v/c$, $\gamma^2 = 1/(1 - \beta^2)$, N_e is the number density of electrons, m_e is the electron mass, $I_{e,m}$ and $\delta_{e,m}$ are the mean ionization potential and density effect corrections for the electric and magnetic projectiles.

For slow monopoles ($10^{-4} < \beta < 10^{-2}$), it is important to distinguish the energy lost in ionization or excitation of atoms and molecules of the medium ("electronic" energy loss) from that lost to yield kinetic energy to recoiling atoms or nuclei ("atomic" or "nuclear" energy loss). Electronic energy loss predominates for electrically or magnetically charged particles for $\beta > 10^{-2}$. The dE/dx of MMs with $10^{-4} < \beta < 10^{-3}$ is mainly due to excitations of atoms.

Energy losses of very low velocity monopoles, i.e. with $\beta < 10^{-4}$, cannot excite atoms; they can only lose energy in elastic collisions with atoms or with nuclei.

3.6.1 Energy losses of magnetic monopoles in the Atmosphere

We use the same approach as the one used by the MACRO collaboration for their detection in the streamer tubes. This approximation can be reasonable for the lowest layers of atmosphere where the density is of the same order as in the steamer tube one.

At high velocities: $\beta > 0.05$, the formula that holds for the MM ionization energy losses is the usual one, used by Derkaoui et al. [59]

$$-\frac{dE}{dx} = \frac{4\pi N_e g^2 e^2}{m_e c^2}\left[Ln\left(\frac{2m_e c^2 \beta^2\gamma^2}{I}\right) - \frac{1}{2} + \frac{k}{2} - B_m \right] \tag{3.4}$$

where N_e is the density of electrons in the medium, m_e the electron mass, g the magnetic charge of the monopole ($g = n \times g_D$) and I the mean ionization potential in air. The QED correction k and the Block correction B_m parameters are given by [59].

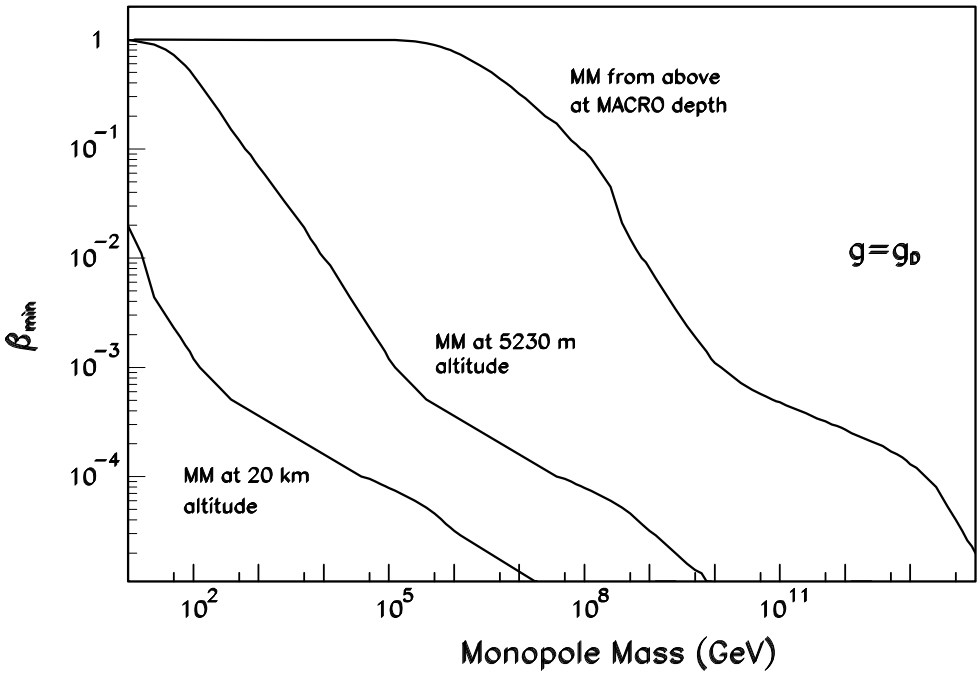

Fig. 3.6 The downgoing MMs accessible mass regions in the plane (mass, β) for g = g_D at an altitude of 20 km, for an experiment at 5230 m (SLIM) and for an underground experiment (MACRO) [59].

The computations of Ref. [76] show that only heavy monopoles can traverse the Earth: for instance for $g = g_D$ and $\beta = 10^{-3}$ only MMs with $m_M > 10^{14}$ GeV can traverse the Earth. Fig. 3.6 shows the accessible mass region for MMs of different

velocities coming from above; for g = g_D and β = 10^{-3} a MM must have $m_M > 10^{10}$ GeV, 10^5 GeV, 10^2 GeV in order to reach the underground MACRO detector; the SLIM detector at 5230 m altitude and for a detector at a height of 20 km, respectively [77, 78, 29].

3.6.2 Energy losses of magnetic monopoles in CR39

The REL in CR39 has been calculated for MMs [88, 31]. For $\beta > 0.05$, the REL for MMs are obtained excluding the energy transfer due to high energy δ-rays.

$$REL = \begin{cases} \dfrac{\omega_p^2 g^2}{c^2}\left[Ln\left(\dfrac{1.123\beta c\gamma\sqrt{\varepsilon-1}}{b\omega_p}\right) - \dfrac{1}{2}\right] & if\ \beta < 1/\sqrt{\varepsilon} \\ \dfrac{\omega_p^2 g^2}{c^2}\left[Ln\left(\dfrac{1.123 c}{b\omega_p}\right) - \dfrac{1-1/\beta^2}{2\,(\varepsilon-1)}\right] & if\ \beta > 1/\sqrt{\varepsilon} \end{cases} \tag{3.5}$$

where ω_p is the plasma frequency given by: $\omega_p^2 = 4\pi N_e \dfrac{e^2}{m_e}$, N_e is the electronic density in the medium and m_e the electron mass. ε is given by $\sqrt{\varepsilon/\varepsilon - 1} = 0.562\ I/\hbar\omega_p$, I being the mean ionization potential, $b = \dfrac{1.123\hbar c}{\sqrt{2m_e c^2 \omega_0}}$ is the minimum impact parameter below which production of δ-rays occur. For CR39: ω_0 = 200 eV, I = 73 eV, $\varepsilon = 1.6$ and ρ = 1.32 g/cm^3.

For β < 0.05 there are two contributions to the restricted energy loss: the contribution due to *ionization* and the contribution due to *elastic recoils*. In the range $3\times10^{-4} < \beta < 10^{-2}$, the Ahlen-Kinoshita formula [78] for non conductors is used:

$$\frac{dE}{dx} = \frac{2\pi N_e g^2 e^2 \beta}{mcv_F}\left[\ln\frac{2m_e v_F a_0}{\hbar} - 0.5\right] \tag{3.6}$$

where N_e is the density of electrons, a_0 is the Bohr radius and $v_F = \frac{\hbar}{m_e}\left(3\pi^2 N_e\right)^{1/3}$ is the Fermi velocity of the free electrons in the medium. For Lexan, $v_F \sim 2.59\times10^8$ cm/s. The result in REL vs β is shown in Fig. 3.7. The bump in REL is due to elastic recoil contribution at low velocity

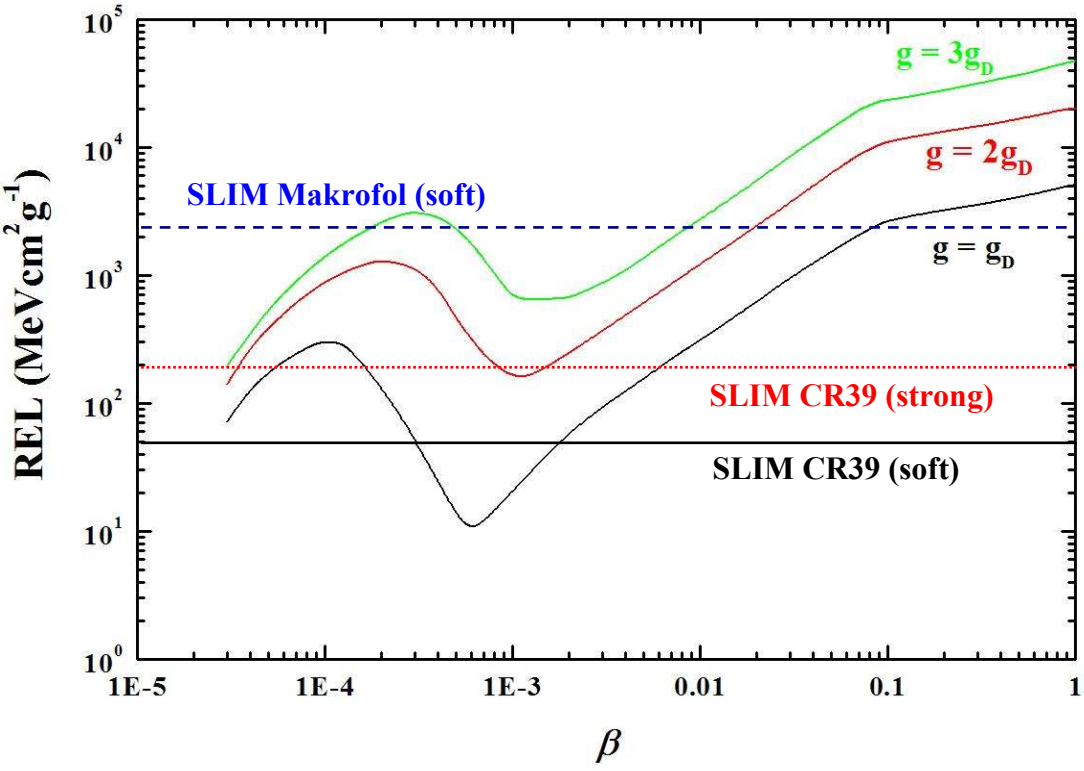

Fig. 3.7 The Restricted energy loss of MMs vs β in CR39 NTDs. The solid and doted lines show the different detector threshold.

3.7 Nuclearites (Strange Quark Matter)

Witten proposed the possible existence of the Strange Quark Matter (SQM) [79]; namely an aggregate consisting of approximately equal numbers of u (up), d (down) and s (strange) quarks. SQM has an integer electric charge which is

neutralised by an electron cloud surrounding it and forming a sort of atom, see Fig. 3.8.

SQM could have been produced in the early Universe just after the Big Bang and may have survived as remnant or it may also be produced in violent astrophysical processes such as in neutron stars collisions and quarks stars [80-83]. Their existence may address the problem of cold dark matter and of exotic events in the cosmic radiation, also other possibilities have been mentioned [37]

SQM is expected to have a density slightly larger than ordinary nuclear matter; the relation between the mass M of SQM lumps and their baryonic number A (one third of the number of constituent quarks) would be

$$M(GeV) \leq 0.93A \tag{3.7}$$

An upper limit for the flux of SQM in the CR (also called nuclearite) may be obtained assuming that they represent the main contribution to the local Dark Matter (DM) density,

$$\Phi_{\max} = \frac{\rho_{DM} v}{2\pi M} \tag{3.8}$$

where v and M are the nuclearite average velocity and mass, respectively and the density of the dark matter is $\rho_{DM} \approx 10^{-24} g/cm^3$

Searches for nuclearites were performed by different experiments [61-64]. The best flux upper limit was set by the MACRO experiment: for nuclearites with $\beta \sim 10^{-3}$, the 90% C.L. upper limit is at the level of 2×10^{-16} $cm^{-2}sr^{-1}s^{-1}$ for the mass range 10^{14} GeV < M < 10^{22} GeV [60,61].

If R_N is the radius of the nuclearite core the system core + electronic cloud (nuclearite) should have a constant radius of ~ 1 Aº for $R_N \leq 1 \mathring{A}$. For greater radii all electrons must be inside the quark bag, see Fig. 3.8.

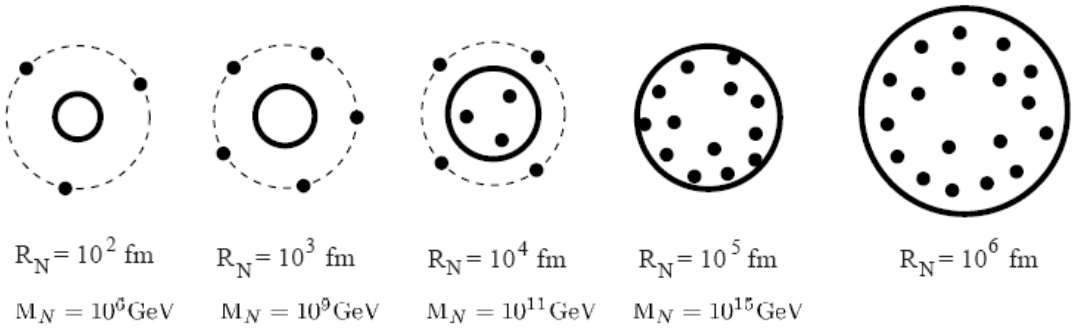

Fig. 3.8 The quark bag radius (R_N) and the core-electron system for nuclearites. For nuclearite masses smaller than 10^9 GeV/c^2, the whole electron cloud is outside the quark bag, the global size of the whole system is approximately 10^5 fm = 1 °A; for $10^9 < M_N < 10^{15}$ GeV/c^2 the electrons are partially inside the core; for $M_N > 10^{15}$ GeV/c^2 all electrons are inside the core. The black dots indicate the electrons, the quark bag border is indicated by the solid lines; the border of the core+electronic cloud system for relatively small masses is indicated by the dashed lines.

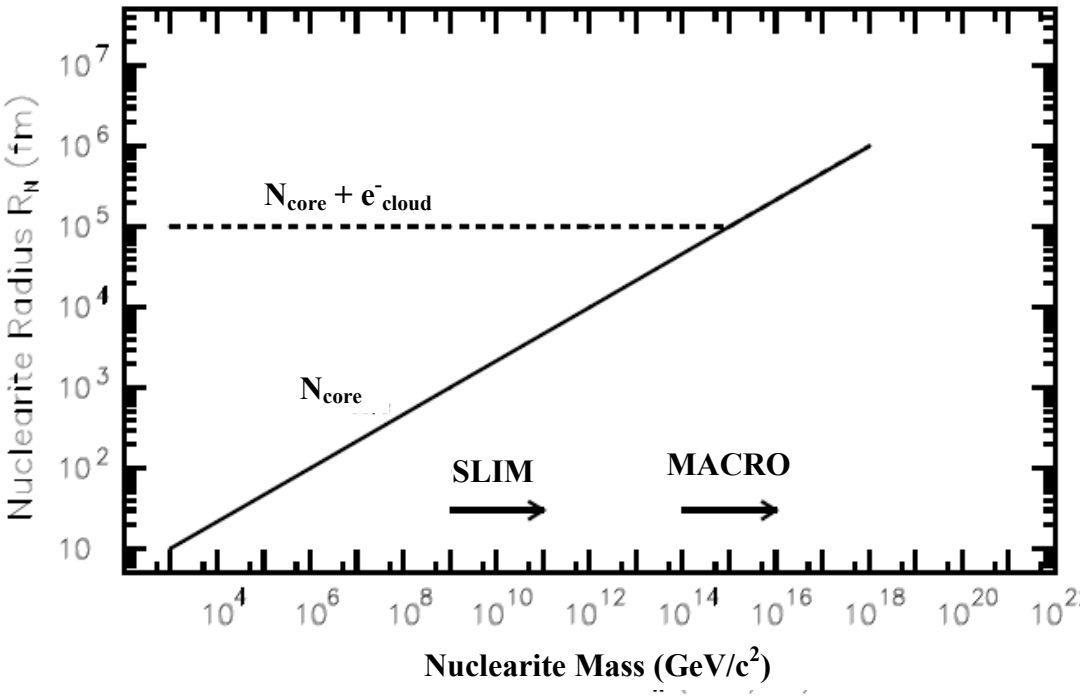

Fig. 3.9 The solid line shows the nuclearite R_N radius for different nuclearite mass M_N. The dashed line shows the radius of the whole nuclearite system (core + electron). Accessible mass region for the MACRO and SLIM experiments are also indicated.

The radius of the nuclearite core can be computed as follow:

$$R_N = \left(\frac{3M_N}{4\pi\rho_N} \right)^{1/3} \tag{3.9}$$

where M_N is the Nuclearite mass. For $M_N = 1.5 \times 10^{-9} g$ the nuclearite should have a radius of 1 Å.

Nuclearites should be stable for any baryon number A in the range between ordinary heavy nuclei and neutron stars ($A \approx 10^{57}$).

3.7.1 Energy Loss of Nuclearites in the Atmosphere

Nuclearites of galactic velocities are protected by their electron atmosphere and coulomb repulsion from direct nuclear interactions with the atoms they may hit along their path and the same for nuclearites that have come to rest in matter [84]. Thus, he considers that the principal energy-loss mechanism for a nuclearite passing through matter is that of atomic collisions. These collisions are mainly elastic or quasi-elastic for velocities ~10^{-3}c and the rate of energy loss for a massive nuclearite is [84]:

$$\frac{dE}{dx} = -\sigma \rho v^2 \tag{3.10}$$

where σ is the effective cross-section of the nuclearite, v its velocity and ρ the density of the medium. Considering what was discussed above concerning nuclearites dimensions, one will have [84]:

$$\sigma = \begin{cases} \pi A^{\circ 2} \; for R \le 1A^{\circ} (M \le 1.5ng) \\ \pi \left(\dfrac{3M}{4\pi\rho_N} \right)^{2/3} \; for R \ge 1A^{\circ} (M \ge 1.5ng) \end{cases} \tag{3.11}$$

3.7.2 Accessibility region of Nuclearites

For galactic nuclearites, the velocity decreases exponentially with distance L:

$$v(L) = v(0)\exp\left(-\frac{M}{\sigma}\int_0^L \rho dx\right) \tag{3.12}$$

where M is the mass of nuclearite and $v(0)$ its velocity at the top of the atmosphere.

The range of nuclearite can be computed considering that the nuclearite is quickly brought to rest when its velocity becomes smaller than velocity of sound in the medium $v_c = \sqrt{\varepsilon/\rho}$, so the material will resist interpenetration; $\varepsilon \sim 10^9$ ergs/cm^3 ~ 0.1 MeV per molecular bound, is the structural energy density for integrity of rocks (Young's modulus). The range of nuclearites is given by

$$\int_0^L \rho dx = \frac{M}{\sigma} Ln\left(\frac{v(0)}{v_c}\right) \tag{3.13}$$

We consider the parameterization of the standard atmosphere from [85]:

$$\rho(h) = ae^{-\frac{h}{b}} = ae^{-\frac{H-h}{b}} \tag{3.14}$$

where the constants are a = 1.2 × 10^{-3}g cm^{-3} and b ≈ 8.57 × 10^5 cm; H is the total height of the atmosphere (≈ 50 km). The integral in eq. 34 may be solved analytically

$$\int_0^L \rho dx = abe^{-\frac{H}{b}}\left(e^{\frac{H=h}{b}-1}\right) \tag{3.15}$$

Fig. 3.10 shows the accessible region of nuclearites in the (mass,β) plane at different experimental depths for their detections. Typical balloon experiments (CAKE, 40 km), civilian airplanes (11 km), the Chacaltaya high altitude laboratory (SLIM, 5.23 km), at sea level and experiment at underground

laboratory (MACRO at a depth of 3400 mwe) are also included. The CR39 and Makrofol detection thresholds for the SLIM NTDs corresponding to REL = 300 MeV g^{-1} cm^2 and 2500 MeV g^{-1} cm^2 values are also shown as dashed curves [86,87].

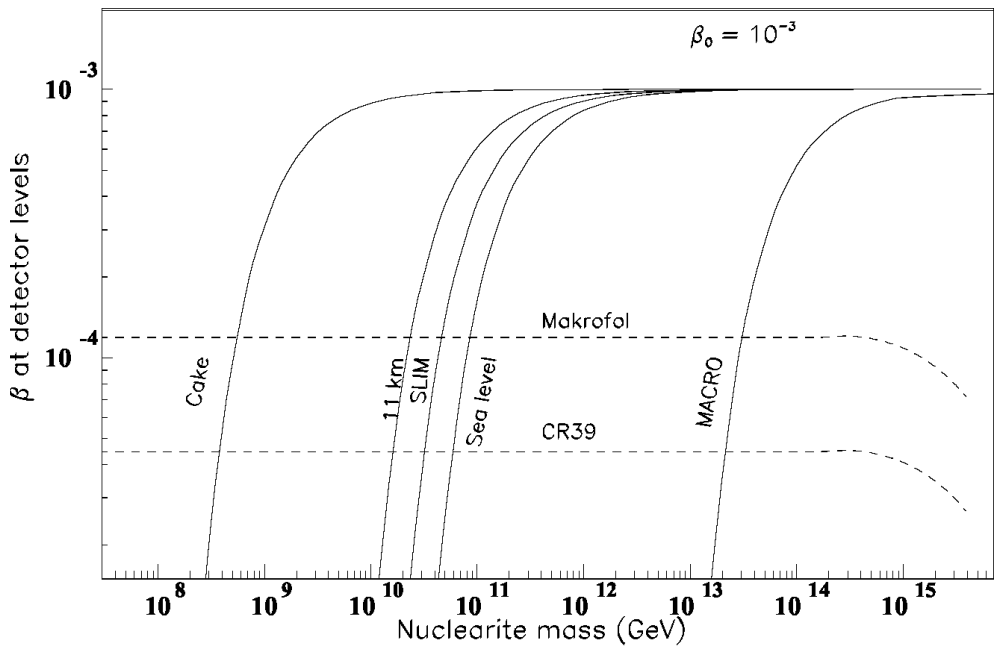

Fig. 3.10 Accessibility region in the (mass, β) plan for Nuclearites at different depths, assuming the initial velocity of the outer atmosphere of $\beta = 10^{-3}$ (Chatalcaya altitude, 5230m (540 g/cm^2); sea level (1033 g/cm^2) and MACRO depth (3700 hg/cm^2). The detection thresholds of CR39 and Makrofol NTDs are shown with the dashed lines.

The decrease of the velocity thresholds for nuclearite masses larger than 8.4×10^{14} GeV is due to the change in the nuclearite cross section, according to eq. 3.12.

An experiment at the Chacaltaya altitude lowers the minimum detectable nuclearite mass by a factor of about 2 with respect to an experiment performed at sea level. If the mass abundance of nuclearites decreases strongly with increasing mass this could yield an important increase in sensitivity.

4 Experimental

4.1 Calibration

The identification of a relativistic charged fragment with the help of a NTD relies on two sources of information. First, we have a fairly good knowledge of how a charged ion loses energy while propagating in a stopping medium of well-known chemical and physical properties. Secondly, the ion trajectory leaves a physically observable signature that can be experimentally observed with a high degree of accuracy. The first of these inputs is derived from the expression of Relative Energy Loss (as discussed in section 2.2.3), which is a function of Z/β, and the second input is obtained through the measurement of the reduced etch-rate of the ion. A correlation between the two quantities constitutes the 'calibration curve'. With the help of this curve, a purely geometrical measurement (i.e the cone-length of a track or the area of its base) can be translated into a physical parameter, namely, the charge of the ion (if all fragments are highly relativistic). In this chapter, the methodology and results of the calibration in two different detector systems are described, by using data based on the exposures of detectors to a variety of relativistic energy ion beams and their fragments.

4.1.1. Chemical etching

An important item is the determination of the optimal etching conditions to achieve the best surface quality and reduce the number of fake tracks in CR39 and Makrofol NTDs used in the SLIM experiment as well as in other experiments. Previously we used aqueous solutions of NaOH and KOH. Extensive studies have been done on the improvements of etching conditions with improved stirring and temperature control of the etching solution and with addition of fraction percentages

of ethyl alcohol. The addition of ethyl alcohol in the etchant improves the etched surface quality and reduces the number of surface defects and background tracks.

A stack composed of CR39 NTDs of size 11.5 x 11.5 cm^2 with 1 cm thick lead target was exposed to the CERN-SPS lead beam (158 A GeV Pb^{82+}) ions (see Fig 4.1 & 4.3). Stacks composed of CR39 of the same size with 1 cm thick polyethylene (CH_2) target were exposed to 5 AGeV Fe^{26+} and 1 A GeV Fe^{26+} and Si^{14+} ions in 2005 at BNL, USA (see Fig. 4.4). More stacks of CR39 detectors were exposed to 0.41 AGeV Fe^{+26} and 0.29 A GeV C^{6+} beams at HIMAC, Japan (see Fig. 4.5). Most of the exposures were carried out at normal incidence and with a nominal density of 1500 to 2000 ions/cm^2. The CR39 material was manufactured by Intercast Europe Co., Parma, Italy using a specially designed line of production. The CR39 thickness was 700 μm or 1400 μm. The Makrofol detectors were manufactured by Bayer A.G., Germany. The Makrofol thickness was 500 μm; CR39 and Makrofol detector sheets were covered by a 30 μm plastic film to protect them from exposure to ambient radon. The protective layers were removed before etching the NTDs.

The etchants used were water solutions of: 6N NaOH, 6N KOH at 70 and 60 ^oC, respectively, with different fractions of ethyl alcohol. These are called “soft” (normal) etching conditions. We also used “strong” etching conditions in order to fastly reduce the thickness of the detectors for the analysis of the SLIM CR39 and Makrofol NTDs. For strong etching, we used mainly 8N NaOH, 7N KOH, 8N KOH water solution at 75 and 77 ^oC, with the addition of different fractions of ethyl alcohol in the solution.

To avoid the deposit of etched products on the detector surfaces and to have homogeneous solution, the stirring was kept constant during etching. After etching the bulk etch velocity v_B was measured (from the change-in-thickness method) for all the detectors, and also by another method (measuring the track cone height and diameter) for those detectors having tracks of measurable cone length.

For the study of the bulk etch velocity variations and of the effects from stirring and evaporation of alcohol we used unexposed Makrofol and CR39 detectors of various thicknesses and sizes.

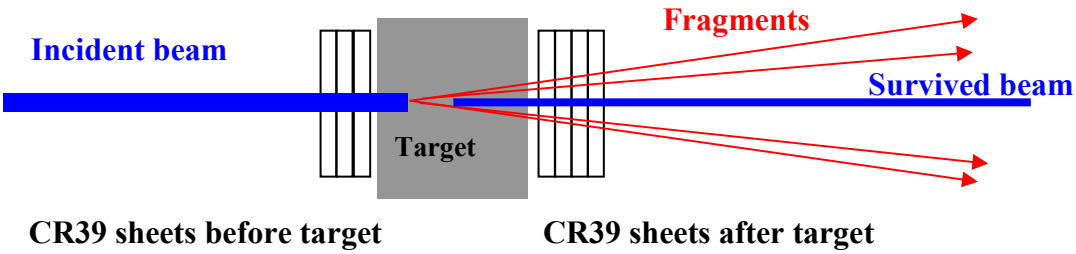

Fig. 4.1 Exposure set-up for the calibration of CR39 and Makrofol NTDs to relativistic ions.

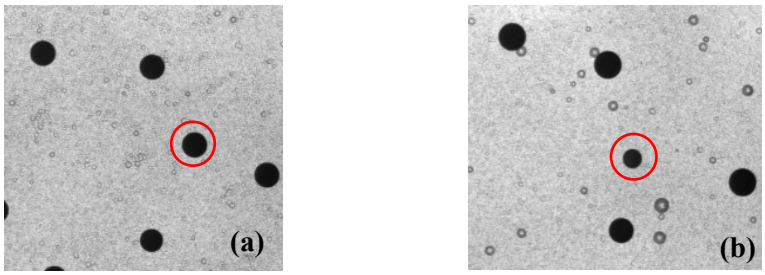

Fig. 4.2 (a) Tracks of beam ions before the target and (b) beam and fragment tracks after the target (from the 0.41 A GeV Fe^{26+} exposure). The tracks marked with a red circle are from a Iron nuclei (a) and its fragment (b), respectively.

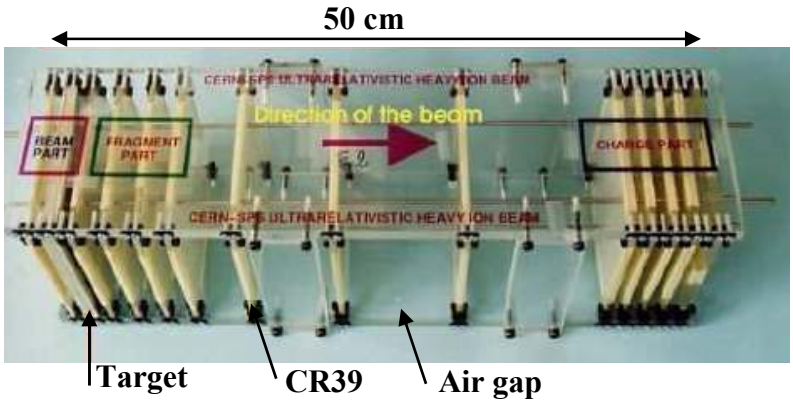

Fig. 4.3 Photograph of the detector stacks exposed at the CERN 158 A GeV Pb^{82+} beam.

BNL Exposure set up

NSRL (a) **AGS (b)**

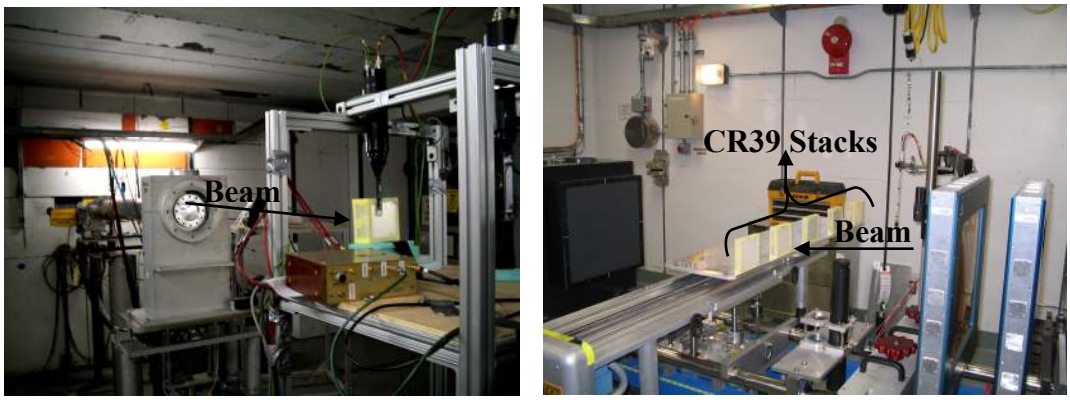

Fig. 4.4 The BNL exposure set-up at two beam lines, a) NSRL and b) AGS.

HIMAC Exposure set up

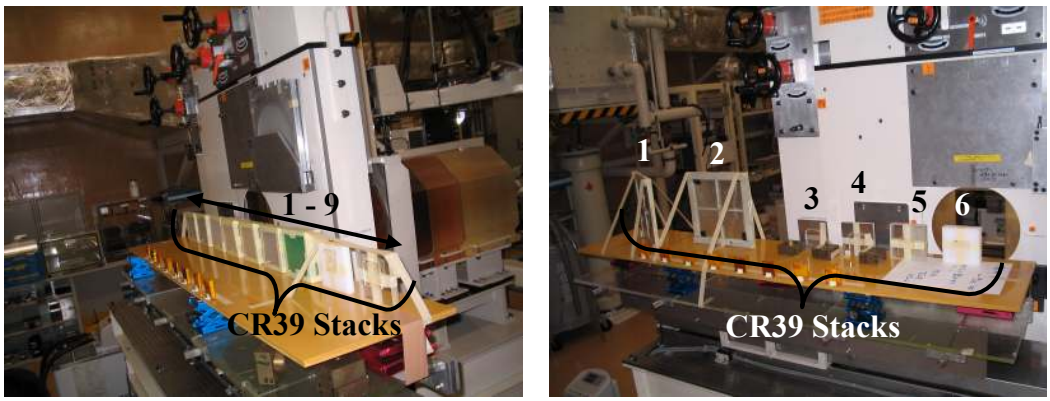

Fig. 4.5 Exposure set-up for the stacks of CR39 and Makrofol NTDs at HIMAC, Chiba, Japan.

Most of the tests were aimed at determining the best fraction of ethyl alcohol in the etchant solution and to obtain the optimal etching conditions for surface quality and background reduction. Experimental details are given in the sections 5.2 and 5.3 for "soft" and "strong" etching of CR39 and Makrofol.

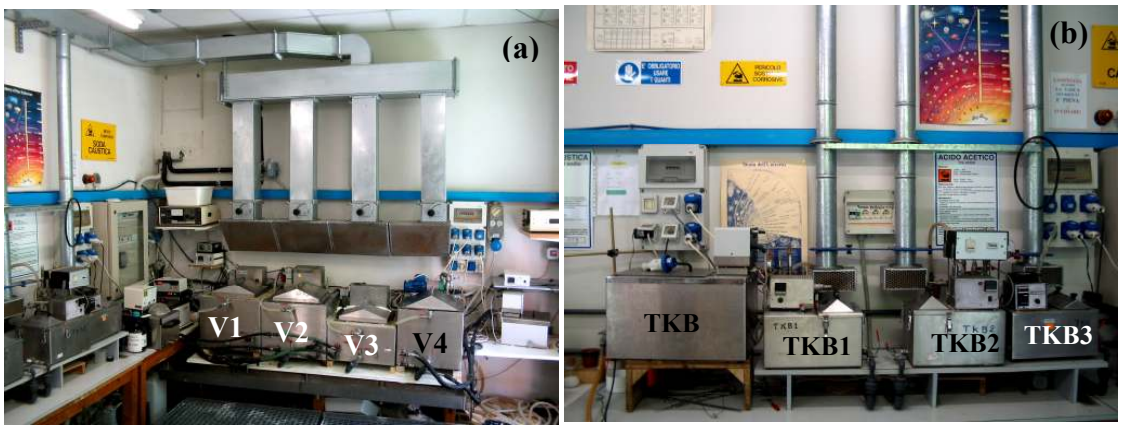

Fig. 4.6 Tanks used for the etching of CR39 and Makrofol NTDs; (a) the V2 & V4 tanks are used for the etching of SLIM NTDs, V3 is used for calibration purposes, and V1 is used for the washing of the NTDs after etching. (b) The TKB tank is used for pre-soaking; TKB1 & TKB2 are used for etching few detectors for calibrations and tests; TKB3 is used for cleaning the NTDs.

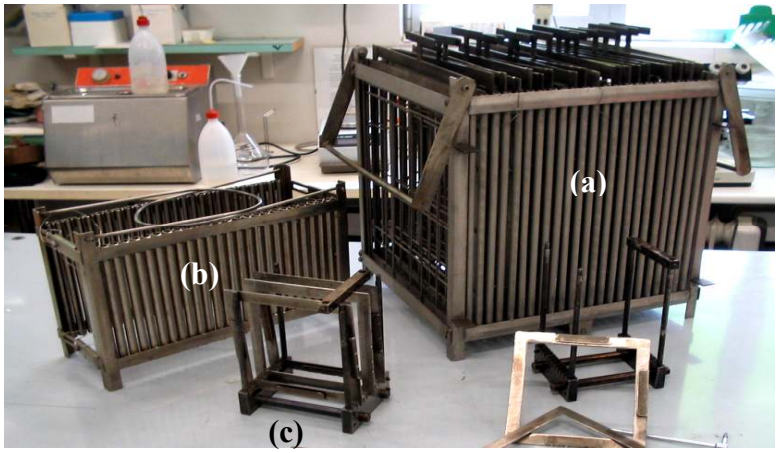

Fig. 4.7 Stainless steel supporting racks used for etching of CR39 and Makrofol NTDs. (a) Rack used for strong and soft etching of the SLIM NTDs in the V2 and V4 tanks (see Fig. 4.5a); (b) rack used for etching in the V3 tank for calibrations; (c) rack used for etching of NTDs in the TKB1 and TKB2 tanks.

Chemical etchings were performed in stainless steel tanks: two large tanks (40 x 52 x 40 cm^3, named V2 or V4), a medium tank (40 x 40 x 26 cm^3, named V3) and two small tanks (22 x 34 x 16.5 cm^3, TKB1 and TKB2) having different types of improved stirring and heating systems, and of temperature control (see Fig. 4.6). The large tank is equipped with a heating system composed of an oil circuit external to the tank. The large and medium tanks also have a stirring-head with motorized pumps and an internal thermo-resistance with digital controlled system. The temperature controlled system guarantees the stability of the temperature throughout the solution to within ± 0.01 ^oC. The small tank was equipped with only internal thermo resistances and a motorized stirring head. The stability of the temperature was within ± 0.1 ^oC. Detector foils were placed in the stainless steel detector holders (see Fig. 4.7).

4.2 Chemical Etching of CR39 NTDs

4.2.1 "Soft" Chemical Etching

Previous standard etching conditions for CR39 were 6N NaOH water solution. In order to improve the surface quality of the post-etched detectors, we made a series of tests adding alcohol in the preparation of etching solution. In Table 4.1 the "soft" etching conditions used for CR39 sheets exposed to the 158 A GeV Pb^{82+} and In^{49+} ions are listed.

The CR39 etched in 10 % ethyl alcohol, 6N KOH solution at 70 ^oC, Fig. 4.8b, was transparent and fake track density was much lower compared to the detector etched without ethyl alcohol (Fig. 4.8a), but the threshold was higher ($Z/\beta \geq 30$ instead of 5). For this etching condition, it was not possible to measure the tracks automatically with the ELBEK system because of the lower contrast of the detector surfaces. In order to improve surface contrast we etched the CR39 in 3 % ethyl alcohol in 6N KOH at 60 ^oC. There was a significant decrease of fake tracks due to surface defects and an increased contrast on the detector surface (see Fig. 4.8c); it

was thus possible to measure the tracks with the ELBEK system, but the detection threshold is still too high ($Z/\beta \geq 21$). In order to reduce the detection threshold the CR39 NTDs were etched in 1% ethyl alcohol solution of 6N NaOH for an etching time of 40 hr (see Fig. 4.8d). The etching time was increased from 30 h to 40 h in order to enlarge the base cone areas of small nuclear fragments.

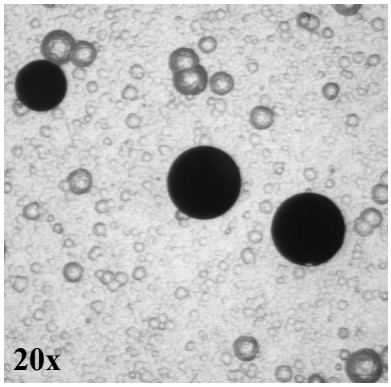

(a) 70 ^{o}C, 6N NaOH, 30 h

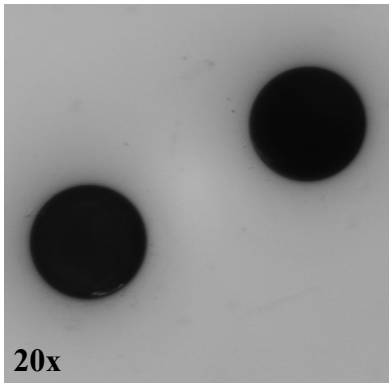

(b) 70 ^{o}C,6N KOH + 10 % ethyl alcohol, 3h

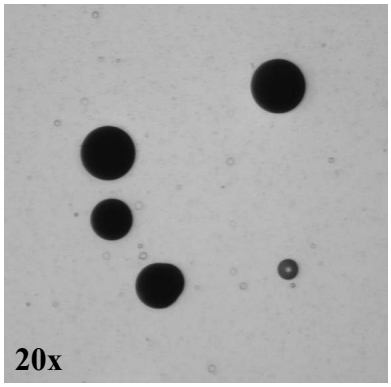

(c) 60 ^{o}C, 6N KOH + 3% ethyl alcohol, 30 h

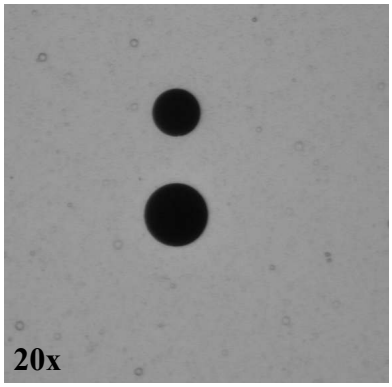

(d) 70 ^{o}C, 6N NaOH + 1 % ethyl alcohol, 40 h

Fig. 4.8 Tracks in CR39 of 158 A GeV Pb^{82+} ions and their fragments (a, b, c) and (d) tracks of 158 A GeV In^{49+} ions and their fragments etched under different etching conditions.

In order to study the bulk etching rate vs time with this new etching conditions, we selected four sheets of CR39 ~1400 μm thick and etched them in 6N KOH with 3 % ethyl alcohol by volume at 60 ^{o}C for 30 h in 5 steps of 6 h intervals. For shorter etching times the thickness is affected by detector swelling. For etching

times larger than 12 h we did not observe any depth dependence of the bulk etch rate, see Fig. 4.9. The identical procedure applied for etching detectors with 1% ethyl alcohol; we observed the same swelling effect for shorter etching time.

Table 4.1. "Soft" etching conditions and bulk etch rates v_B for CR39 obtained with the standard method using 25 thickness measurements for each final data point. The errors are statistical standard deviations of the mean.

S.N.	Etching Conditions	v_B (μm/h)
1	6N NaOH, 70 ^oC, 30 h	1.15 ± 0.03
2	6 N NaOH + 1 % alcohol, 70 ^oC, 40 h.	1.15 ± 0.03
3	6 N KOH + 3 % alcohol, 60 ^oC, 30 h.	1.43 ± 0.03
4	6 N KOH + 10 % alcohol, 70 ^oC, 30 h.	9.3 ± 0.2

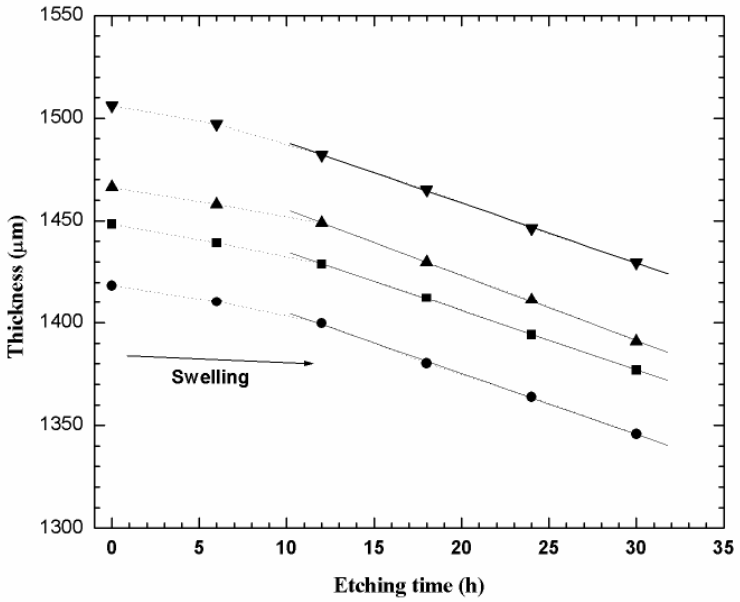

Fig. 4.9 Thickness versus etching time of three different CR39 detectors etched in 6N KOH + ethyl alcohol (3 % by volume) at 60 ^oC. The solid lines are linear fits to the data; the dashed lines only connect the data points (notice the swelling effect for etching times smaller than 12 h).

4.2.2 "Strong" Chemical Etching

Preliminary etching of CR39 foils exposed at Chacaltaya to cosmic rays and to 1 A GeV Fe^{26+} ions were made in 8NaOH at 90 ^{o}C. We found several background tracks of 10-17 μm range due to carbon, oxygen and proton recoils produced in the interactions of ambient neutrons; see Figure 4.10a, b: the surface quality of both sheets was poor. In these conditions, it would be difficult to scan the detectors. In order to improve the surface quality and to eliminate recoil tracks, extensive tests were made by etching the SLIM CR39 sheets in 3%, 1.25% and 1.5% ethyl alcohol in 8N and 7N KOH solution. The CR39 sheets were etched with 8N KOH + 1.5% ethyl alcohol at 75 ^{o}C for 30 hr (see Figure 4.10c, d).

The "strong" etching conditions and the bulk etch velocities of the SLIM CR39 are given in Table 4.2.

Table 4.2. "Strong" etching and bulk etch rates v_B for CR39 obtained with the standard methods using 9 measurements for each final data point. The errors are statistical standard deviations.

S.N.	Etching Conditions	v_B (μm/h)	Threshold (Z/β)
1	8N NaOH, 90 ^{o}C, 50 h	8 ± 0.5	~7
2	8 N NaOH + 3 % alcohol, 70 ^{o}C, 24 h.	15 ± 0.8	~21
3	8 N KOH + 1.25 % alcohol, 77 ^{o}C, 30 h.	6.8 ± 0.3	~15
4	8 N KOH + 1.5 % alcohol, 75 ^{o}C, 30 h.	8 ± 0.5	~17

The surface quality of the etched SLIM CR39 sheets improved and most of the recoil tracks were removed. Moreover the detector is transparent and scanning is easier. The tracks of the relativistic iron ions and their fragments have sharp contours and can be easily measured with the automatic image analyzer system "ELBEK".

The detector threshold is Z/β ~17, compare to Z/β ~7 without alcohol. In 30h the thickness was reduced from ~1400 μm to ~ 900 μm (bulk etching rate of ~8 μm/h).

In order to test if any evaporation effect was still present, we etched the CR39 sheets in tanks of different air tightness; the etching time was 30 h, in steps of 5 h intervals. After each step we measured the thickness of the detectors. The same solution was used throughout all the etchings in each tank. A constant evaporation effect was observed in the tank not perfectly airtight, while there was no observable effect in the perfectly tight tank. Therefore tightness of the medium and large tanks was improved by pasting silicon gel to reduce evaporation.

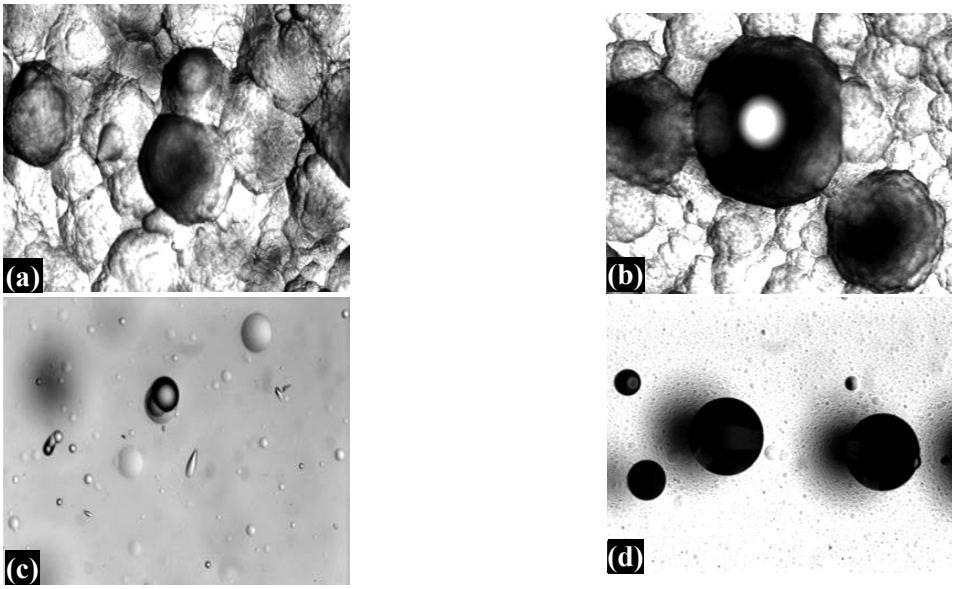

Fig. 4.10 (a) SLIM CR39 sheet, (b) tracks of 1 A GeV Fe^{26+} ions and their fragments in CR39 using 8N NaOH 90 ^{o}C without alcohol, (c) SLIM CR39 sheet and (d) the tracks of 1 A GeV Fe^{26+} ions and their fragments in CR39 with "strong" etching, 1.5% alcohol at 75 ^{o}C.

4.3 Chemical Etching of Makrofol NTDs

4.3.1 "Soft" Chemical Etching

Many tests have been performed with the Makrofol detector to obtain sharp tracks and low background. This was achieved by etching Makrofol detectors in a

water solution of 6N KOH at 50 ^{o}C with 20% ethyl alcohol for an etching time of 8 h; uniform stirring and a tight etching bath was used to minimize evaporation of alcohol during the etching cycle. We obtained tracks, which were suitable for the ELBEK automatic measuring system.

The effect of pre-soaking for Makrofol in a perfectly closed small tank using regular stirring was also studied. For this purpose, we used 9 unexposed detectors 11.5 cm x 11.5 cm in size, 500 μm thick; 4 of them were pre-soaked in de-ionized water for 1 h, raising the temperature from room temperature up to 50 ^{o}C. All the samples were etched in a 6N KOH solution with 20 % ethyl alcohol at 50 ^{o}C for 4 h. The same steps were repeated five times using every time a fresh solution, in order to avoid possible effects for evaporation of ethyl alcohol. The bulk etching rate v_B was determined using thickness measurements after each etching step. Within our uncertainties, we observed no difference between the 4 pre-soaked and the 5 non-pre-soaked sheets.

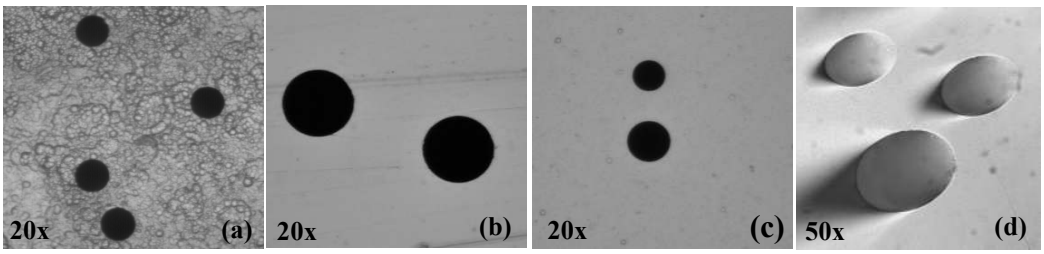

Fig. 4.11 Base areas of the "tracks" from 158 A GeV Pb ions in Makrofol at normal incidence (a) 6N NaOH 50^{o}C, 95 h, (b) 6N KOH + 30 % ethyl alcohol 45 ^{o}C, 10 h, (c) 6N KOH + 20 % ethyl alcohol 50 ^{o}C, 8 h and (d) The tracks of Pb ions and their fragments in Makrofol at 45^{o} incident angle (etching conditions as in c).

For the study of depth dependence few unexposed detectors 500 μm thick were etched in 6N KOH solution with 20 % ethyl alcohol at 50 ^{o}C for a total of 30 h in five steps of 6 h each. In Fig. 4.12 the averaged detector thickness is plotted versus etching time. A constant bulk-etching rate in all the steps within our experimental

uncertainties was observed. No depth dependence of the bulk etching rate and no swelling effects were observed.

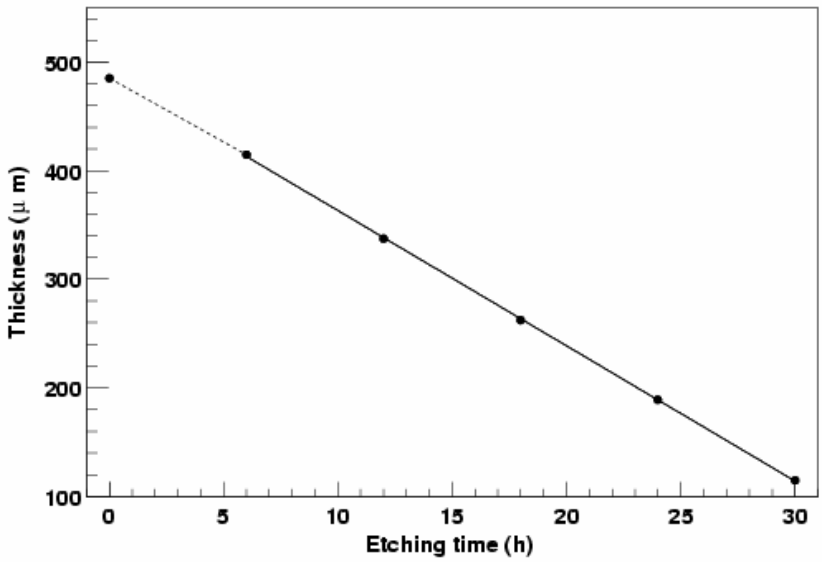

Fig.4.12 Thickness versus etching time for Makrofol foils etched in 6N KOH + 20 % ethyl alcohol (by volume) at 50 °C. Each point is the average of 4 measured sheets. The red solid line is a linear fit. There are no indications of swelling effects at short etching times.

4.4 Response Curves for CR39 and Makrofol NTDs

Several calibrations were performed with relativistic heavy ions in order to determine the thresholds and sensitivity of CR39 and Makrofol NTDs.

After exposures, CR39 sheets located after the target were etched in 6 N NaOH + 1 % ethyl alcohol at 70 °C for 40 h (for the In exposure) and 6N NaOH 70 °C for 30 h (for the Pb, Fe, Si and C exposure). The Makrofol sheets located after the target were etched in 6 N KOH + 20 % ethyl alcohol at 50 °C for 8 h (for the Pb exposure).

We recall that the etched cones are formed because the track etching rate v_T along the damaged track is larger than the bulk etch rate v_B. The size of the etched cone depends on the REL of the particle. For CR39 detectors, etch-pit base diameters

and heights of In ions and their fragments were measured with a Leica optical microscope. For Makrofol, Pb ions and their high Z fragments made through-holes in the detector sheets; thus the cone length L_e was measured only for high Z fragments that have sharp etch-cone tips (no holes). Nuclear fragments with charges $78 \leq Z \leq 82$ were identified by etching Makrofol sheets from the same stack in the same conditions for only 5 hours.

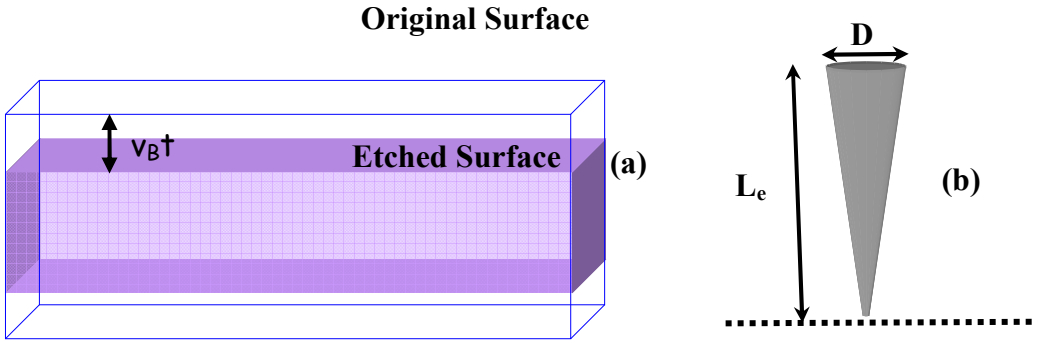

Fig. 4.13 The bulk etch rate measurement methods (a) from the change in the detector thickness and (b) from the measurement of the cone height and diameter of the etched tracks.

4.4.1. "Standard" measurement of v_B

The standard determination of v_B is based on the measurement of the thickness of the detector after different etching times, see Fig. 4.13a. The thickness is measured with an electronic micrometer of 1 μm accuracy in 25 positions on the detector foil. The average bulk-etch velocity is $v_B = \Delta x / 2\Delta t$, where Δx is the mean thickness difference after a Δt etching time. For CR39, at etching times shorter than 10 hours the thickness is affected by detector swelling [11-13]. The bulk etch-rate must be determined by a linear fit of Δx vs Δt for etching times longer than 10 h. For Makrofol no significant swelling effect was observed.

4.4.2. The v_B measurements from the cone height and base diameter

The track etch rate v_T can be considered constant for relativistic heavy ions. For normally incident particles, the measurable quantities are the cone base diameter D, and the height L_e, see Fig. 4.13b [88, 89]. L_e is obtained by multiplying the measured cone height using an optical microscope by the refractive index n of the etched detector material. The refactive index 'n' is obtained from the ratio of the actual thickness (which we measure with an electronic micrometer with a precision of 1 μm) to the apparent thickness measured with an optical microscope (precision of 1 μm) [$n_{CR39} = 1.55 \pm 0.01$; $n_{Makrofol} = 1.69 \pm 0.01$].

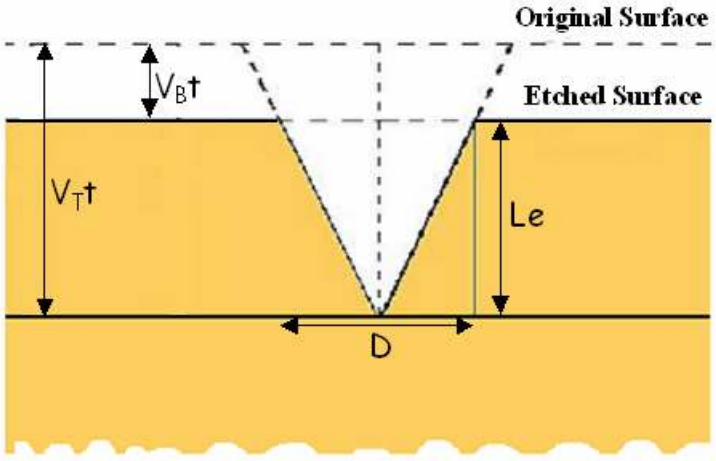

Fig. 4.14 Sketch of an "etched track" and its etched track parameters for a normally incident ion.

The following relations hold:

$$L_e = (v_T - v_B)t \tag{4.1}$$

$$D = 2v_B t\sqrt{\frac{(v_T - v_B)}{(v_T + v_B)}} \tag{4.2}$$

From the above relations, the following quadratic equation in v_B is obtained

$$\left(\frac{L_e}{t}\right)v_B{}^2 - \left(\frac{D^2}{2t^2}\right)v_B - \left(\frac{D^2 L_e}{4t^3}\right) = 0 \qquad (4.3)$$

The real solution for v_B is

$$v_B = \frac{D^2}{4tL_e}\left[1 + \sqrt{\left(1 + \frac{4L_e{}^2}{D^2}\right)}\right] \qquad (4.4)$$

From eqs. 4.1 and 4.2, the reduced etch rate is

$$p = \left(\frac{v_T}{v_B}\right) = 1 + \frac{L_e}{v_B t} = \frac{1 + (D/2v_B t)^2}{1 - (D/2v_B t)^2} = \frac{1 + A/(\pi v_B^2 t^2)}{1 - A/(\pi v_B^2 t^2)} \qquad (4.5)$$

The bulk etch rate v_B and the reduced etch-rate p may by determined by measuring the track parameters L_e (precision of ~1 μm) and D (precision of 0.5 μm).

Eqs. 4.4 & 4.5 were tested with relativistic Pb and In ions and their nuclear fragments. We selected only tracks for which precise measurements of the cone height and diameter could be performed (for example we cannot measure the track cone heights for low Z fragments, for which the microscope image may be affected by shadow effects). Using eq. (4.4) we computed the bulk-etch rate for CR39 and Makrofol. Batches of measurements were made by different operators, and the average v_B's and their statistical standard deviations were computed, see Table 4.3. By this method we obtain v_B values with accuracies of 0.01 ÷ 0.05 μm/h. The v_B values obtained for the same foils using detector thickness measurements are also given in Table 4.3.

we can effectively make measurements with the available measuring instruments using the new method only for intermediate z-values because at low and high z we do not have enough precision for measuring L_e and D, respectively.

The base area of each etch-pit cone, its eccentricity and central brightness were measured with the ELBEK automatic image analyzer system [12], which also provides the absolute coordinates of the etched tracks; this allows the tracking of the beam ions and of their fragments through the CR39 detectors.

In the following sections new response curves for CR39 and Makrofol, based on the new determination of the bulk etch-rate are discussed.

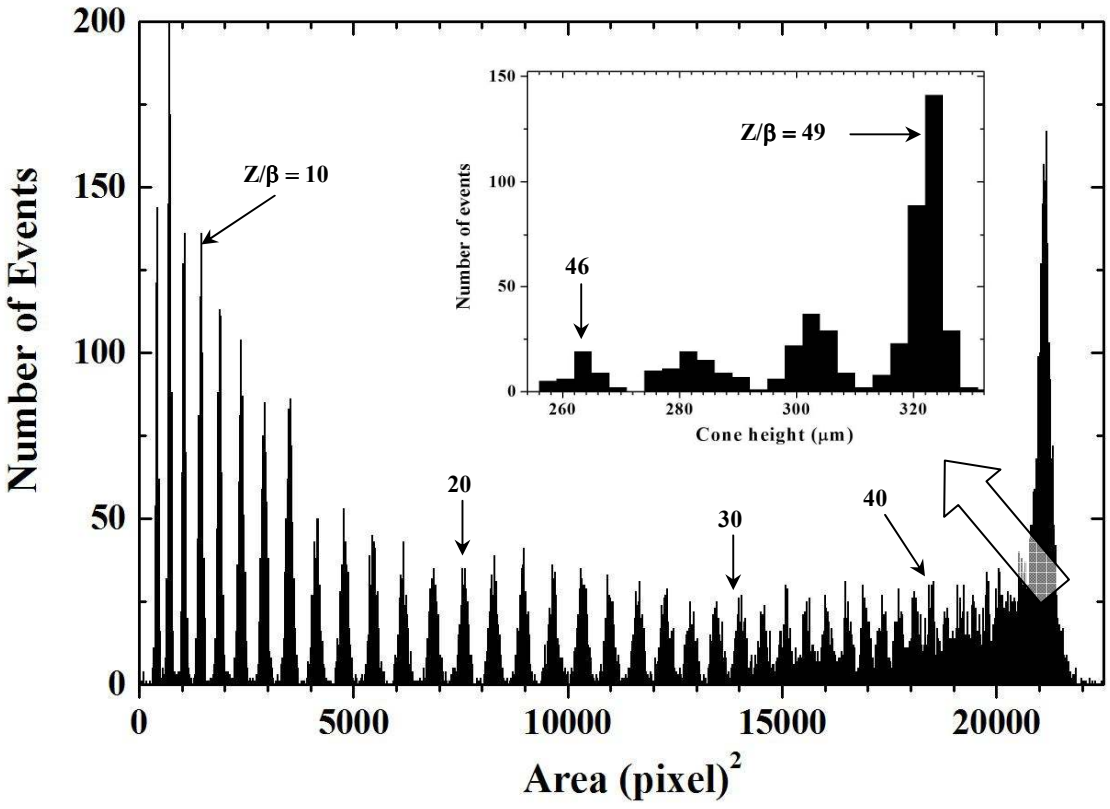

Fig. 4.15 (a) Base area distribution of etched cones in CR39 from 158 A GeV In^{49+} ions and their fragments (averages of 2 front face measurements); (b) cone height distribution for $46 \leq Z/\beta \leq 49$ (single measurements). Soft etching: 6 N NaOH + 1 % alcohol, 70 °C, 40 h.

4.5 Response Curves for CR39

Fig. 4.15 shows the etch-pit base area distribution for Indium ions and their fragments in CR39; averages were computed from measurements made on the "front sides" of two detector sheets. The peaks are well separated from Z/β ~7 to 45; the charge resolution for the average of two measurements is σ_z ~0.13e at Z/β ~15. The charge resolution close to the Indium peak (Z ~49) can be improved by measuring the heights of the etch pit cones [12]. The heights of 1000 etch-cones with diameter larger than 48 μm (corresponding to nuclear fragments with Z > 45) were measured with an accuracy of ± 1 μm with a Leica microscope coupled to a CCD camera and a video monitor. The corresponding distribution is shown in the inset in Fig. 4.15; each of the 4 peaks is well separated from the others, and a charge can be assigned to each one. The charge resolution for a single measurement of different nuclear fragments is given in Table 4.4; it is σ_z ~0.22e at Z/β ~48. The charge resolutions σ_Z may be computed from

$$\sigma_Z = \frac{\sigma_A}{\delta A / \delta Z} \qquad \text{(a)}$$

$$\sigma_Z = \frac{\sigma_{L_e}}{\delta L_e / \delta Z} \qquad (b) \qquad (4.6)$$

where σ_A and σ_{Le} are standard deviations [8], A is the mean base area and L_e the mean height of the etched cones. See Table 4.4 for the numerical results.

For each detected nuclear fragment from Z = 7 to 48 and Indium ions (Z = 49) we computed the corresponding REL values and the reduced etch rate $p = v_T/v_B$ using eq. (4.5). The sensitivity p vs REL for CR39 is plotted in Fig. 4.16. The CR39 detection threshold is at REL ~50 MeV cm^2 g^{-1}, corresponding to a relativistic nuclear fragment with Z ~ 7.

Table 4.3 Bulk etch rates v_B for CR39 and Makrofol NTDs obtained with the new and with the standard methods using 25 measurements for each data point. The errors are statistical standard deviations of the mean.

Detector (beam)	Z-Range	Etching Conditions	v_B (μm/h) New Method	v_B (μm/h) Standard Method
CR39 (In03)	44 - 49	6 N NaOH +1 % alcohol, 70 °C, 40 h.	1.25 ± 0.01	1.15 ± 0.03
CR39 (Pb96)	75 - 80	6 N NaOH, 70°C, 30 h.	1.10 ± 0.02	1.15 ± 0.03
CR39 (Pb96)	78 - 82	6 N NaOH, 45 °C, 268 h.	0.16 ± 0.01	0.17 ± 0.03
Makrofol (Pb96)	75 - 78	6 N KOH + 20 % alcohol, 50 °C, 8h.	3.44 ± 0.05	3.52 ± 0.13

Table 4.4 Assigned charges and computed charge resolutions for In^{49+} and Pb^{82+} ions and their fragments in CR39 and Makrofol detectors. Charge resolution is estimated from eq. 4.6a but the last row was computed from eq. 4.6b.

CR39 Detector		Makrofol Detector	
Charge	*Charge Resolution*	*Charge*	*Charge Resolution*
Z = 8 to 11	0.12e	Z = 51 to 58	0.18e
Z = 12 to 21	0.13e	Z = 51 to 66	0.19e
Z = 22 to 31	0.16e	Z = 59 to 66	0.21e
Z = 32 to 41	0.20e	Z = 59 to 69	0.22e
Z = 32 to 45	0.22e	Z = 70 to 74	0.31e
Z = 42 to 49	0.28e	Z = 75 to 77	0.37e
Z = 46 to 49 ***(by cone height)***	0.22e	Z = 79 to 82 ***(by cone height)***	0.18e

The same analysis procedure was applied for CR39 NTDs etched under strong etching conditions. Previously exposed to relativistic In^{+49} (158 A GeV) and Fe^{+26} (1 A GeV) beams and their fragments.

Fig. 4.17 shows the tracks of relativistic In^{+49} ions and nuclear fragments of S^{16+} and Kr^{36+} ions in CR39 sheets etched with strong and soft etching conditions. Kr^{36+} and high fragments produced through holes with the strong etching condition.

Fig 4.18a shows the mean area distribution of five CR39 independent measurements (detector etched in 8N KOH + 1.25% alcohol at 77 ^{o}C). All peaks with Z/β = 15 to 49 are well separated; the response p vs REL is shown in Fig. 4.19. The detection threshold is at Z/β ~ 15, corresponding to REL ~200 MeV cm^2 g^{-1}.

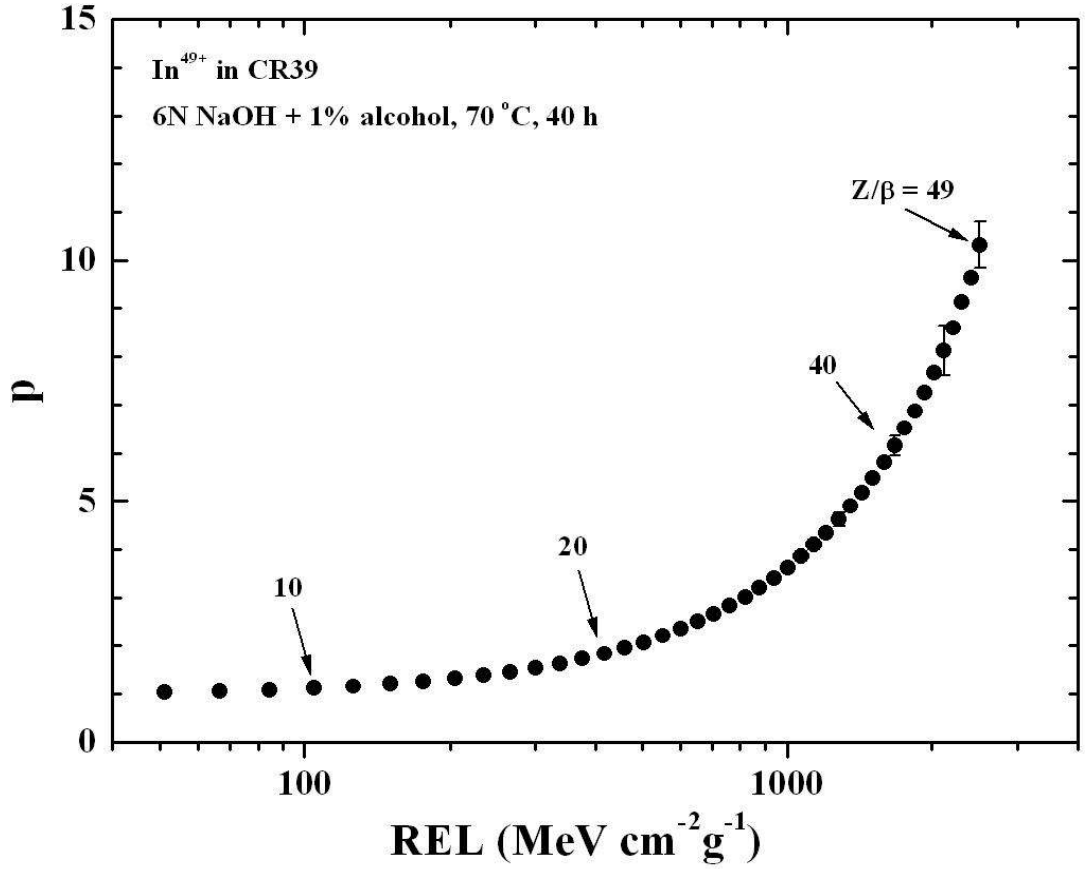

Fig. 4.16 The etch rate ratio p plotted as a function of REL for CR39 detectors exposed to relativistic Indium ions using v_B evaluated with the new method. Typical statistical standard deviations are shown at Z/β = 40, 45, 49; for Z/β ≤ 37 the errors are inside the black points.

For comparison in Fig. 4.18a shows the same mean area distribution of 158 In^{49+} and their fragments obtained by etching the NTDs in 8N NaOH at 90 ^{o}C. Notice that the threshold is at Z ~7, (compared to Z ~15 in the bottom figure). The charge peaks from Z = 8 to 20 are well seen and well separated; instead the peaks from Z

~20 to 35 are not separated well as is the case for the etching in alcohol (8N KOH + 1.25% ethyl alcohol, 77 ^{o}C, bottom figure).

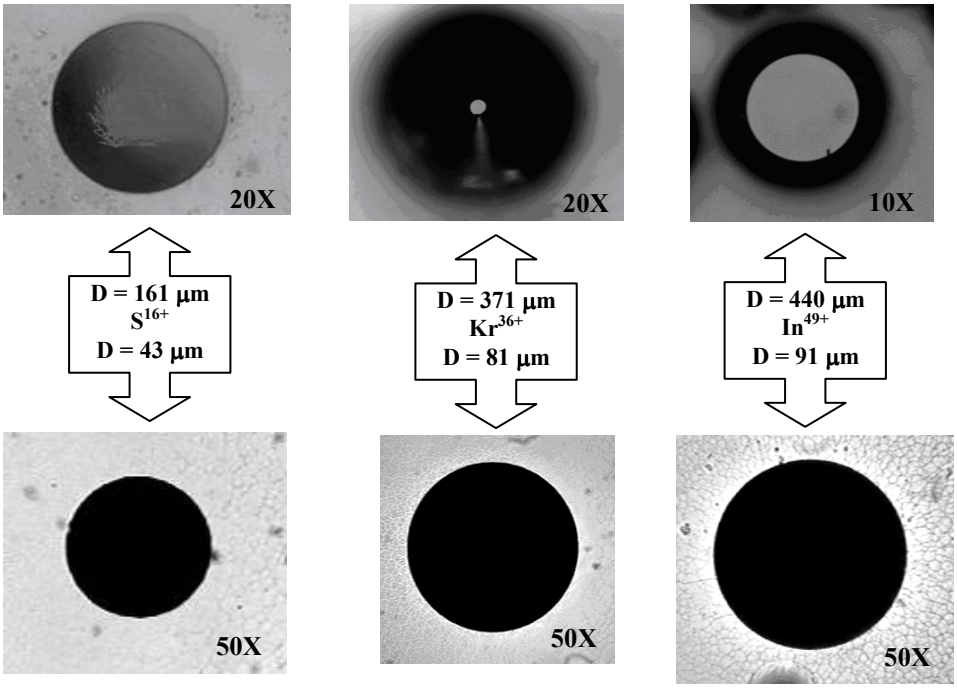

Fig. 4.17 The surface tracks of Indium and their fragments in CR39. On top, the detector was etched in "strong" etching condition for 24 h; the bottom, the same tracks etched in "soft" condition.

In order to achieve low background, high contrast and an "acceptable" threshold for the SLIM experiment, The CR39 sheets were etched in 8N KOH + 1.5% alcohol at 75 ^{o}C for 30 h. The strong calibration was obtained by etching two CR39 sheets exposed to 3 A GeV Fe^{26+}; the detector thickness was reduced from 1400 μm to ~900 μm at the rate of 8 μm/h. Fig. 4.20 shows p vs REL for CR39 etched strongly, the detector threshold is at 300 MeV cm^2 g^{-1} which corresponds to Z/β ~ 17. This is the etching condition for the SLIM CR39 NTDs (see also Fig. 4.10 c,d).

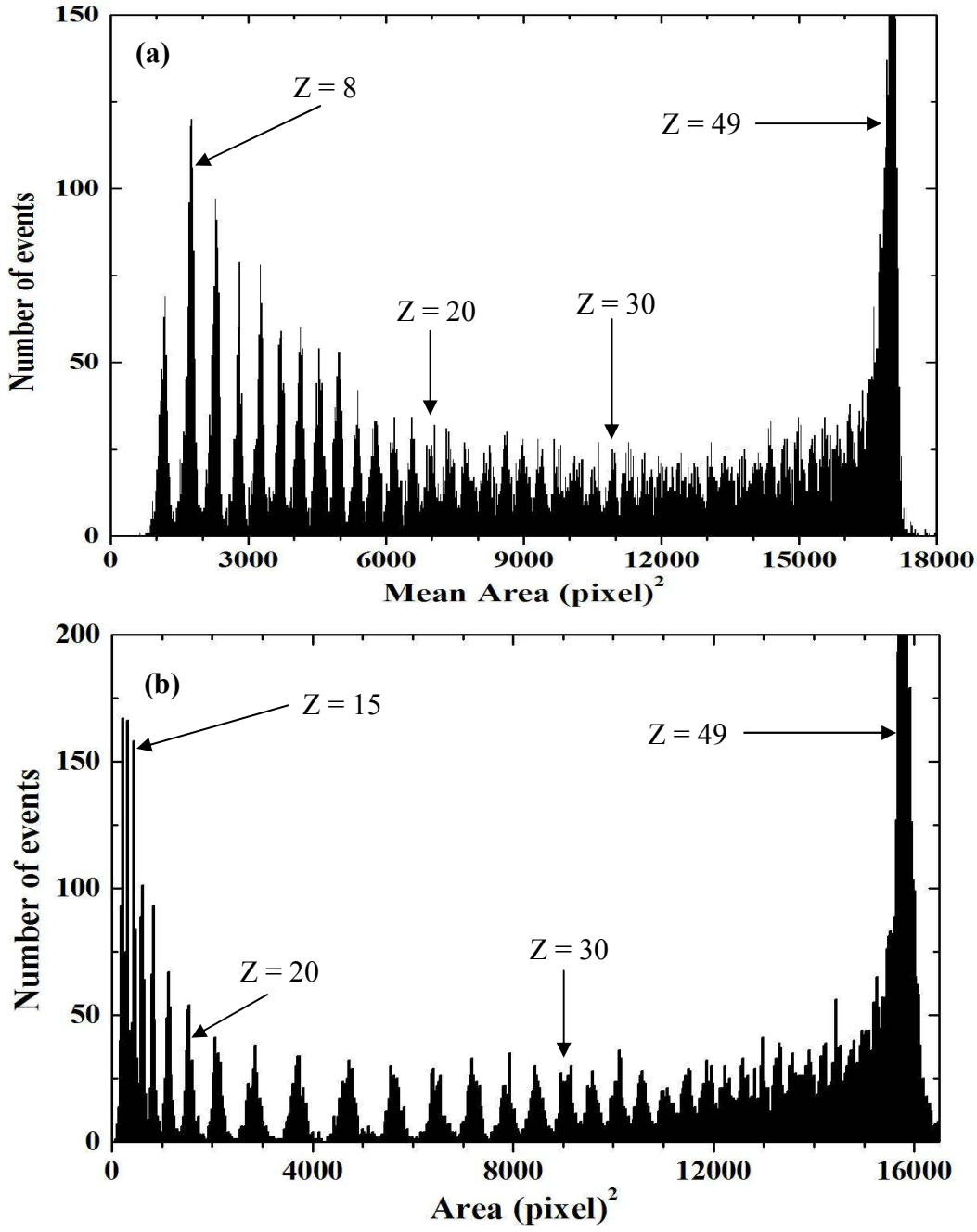

Fig. 4.18 "Strong" etching; mean area distribution (4 faces out of 5) of 158 A GeV In^{49+} ions and their fragments in CR39 after 5.50 h: etching in (a) 8N NaOH 90 °C and (b) 8N KOH + 1.25 % Ethyl Alcohol at 77 °C, respectively.

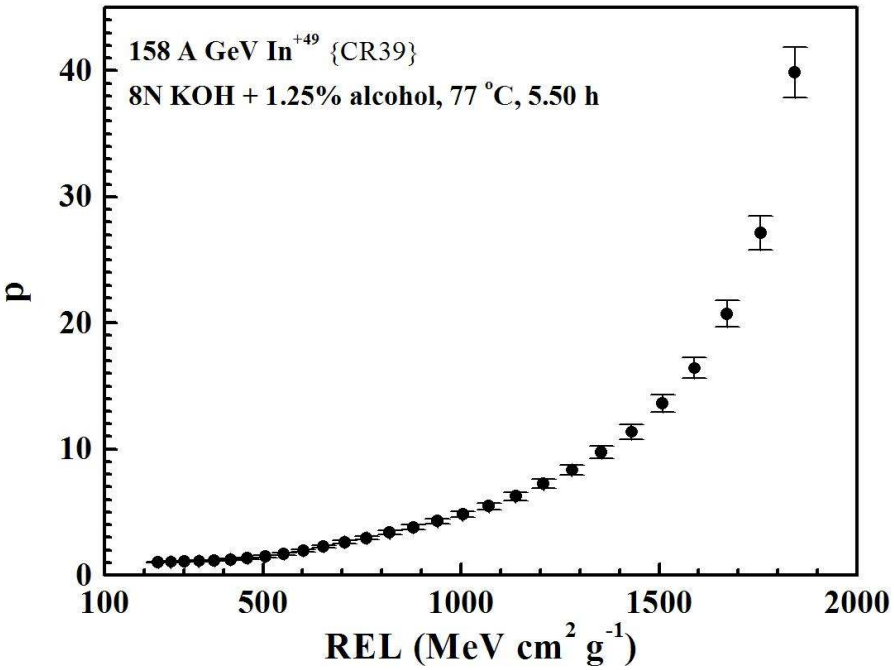

Fig. 4.19 p vs REL for the CR39 detectors exposed to relativistic indium ions and their fragments, etched in "strong" conditions.

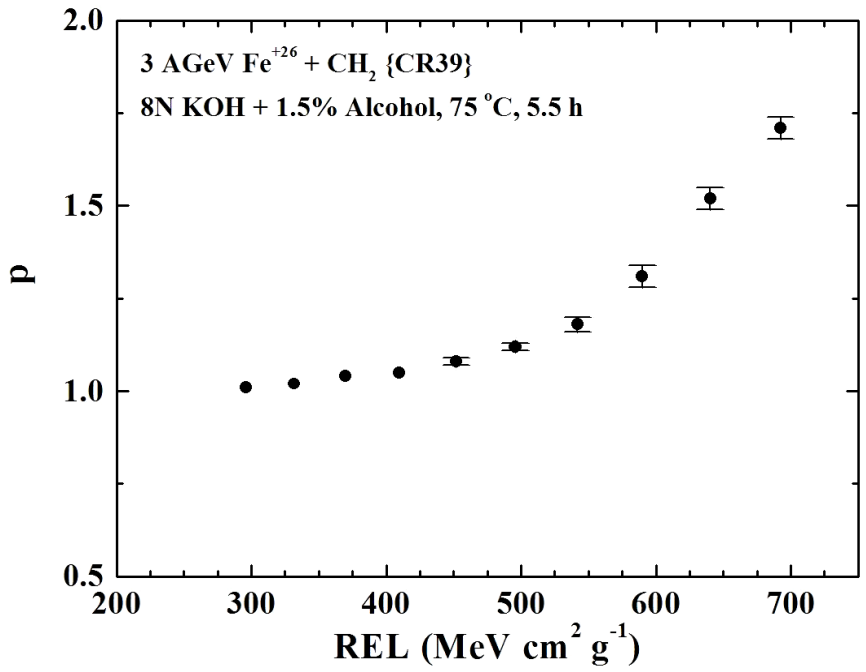

Fig. 4.20 p vs REL for the CR39 detectors exposed to relativistic iron ions and their fragments, etched in "strong" conditions.

4.6 Response Curve for Makrofol

Fig. 4.21 shows the etch-pit base area distribution for lead ions and their fragments in Makrofol NTDs. The resolution of the base area measurement become worse as the charge of the fragment increases, because for high charges the base diameter of the etch pit cone changes slowly compared to the cone height increases sharply. The effect is qualitatively described in Fig 4.22.

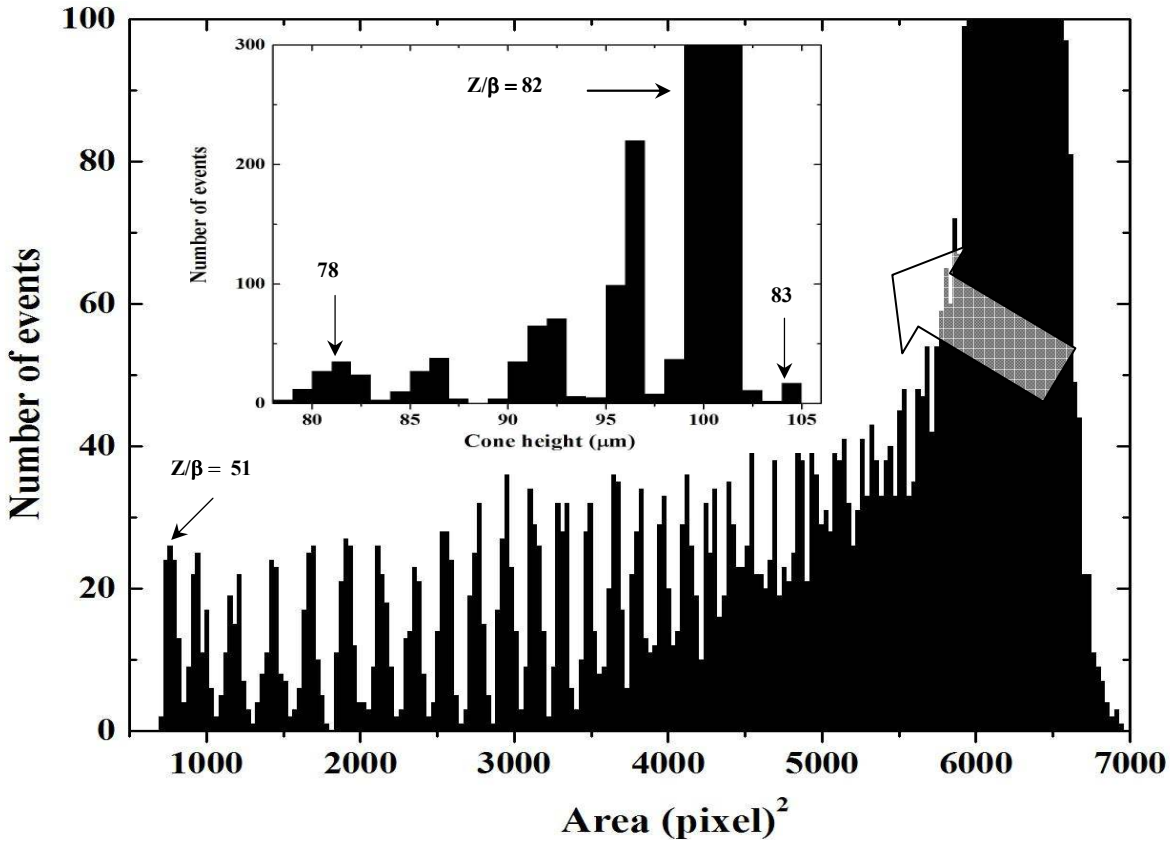

Fig. 4.21 Cone base area distribution (average of 2 measurements on two front faces) of 158 A GeV Pb ions and fragments in Makrofol after 8 h etching, in 6N KOH + Ethyl Alcohol (80 : 20 % by volume) at 50 °C (Inset single measurements of cone heights).

The changes δD and δL_e with respect to δp can be obtained by differentiating eqs. 4.1 and 4.2 with respect to p [101]:

$$\frac{\delta D}{\delta p} = 2 v_B t \sqrt{\frac{p+1}{p-1}} \frac{1}{(p+1)^2} \tag{4.7}$$

$$\frac{\delta L_e}{\delta p} = v_B t \tag{4.8}$$

At large p values, $\delta D / \delta p$ is smaller than $\delta L_e / \delta p$; for high REL it is difficult to obtain a charge resolution <1e from base diameter measurements. From Figs. 4.15 and 4.21 it is apparent that at high Z/β, the base area distribution does not give well separated peaks; instead the peaks are well separated by cone height measurements.

Two Makrofol foils exposed at 90^o and at 45^o with respect to the detector surface, respectively were etched in 6N KOH + 20 % ethyl alcohol. The heights of more than 4000 etch pit cones on each foil were measured with an accuracy of ± 1μm. The cone height distributions are shown in Fig. 4.23(a,b); each peak is well separated from the others, and a charge can be assigned to each. Notice the Z=83 peak which is due to a charge pick-up reaction.

For each charge, the REL and p values have been calculated for the Makrofol detector with the same procedure used for the calibrations of CR39 NTDs (see Fig. 4.24). The Makrofol detection threshold is at REL ~2700 MeV cm^2 g^{-1}, corresponding to a nuclear fragment with Z/β ~50.

As evident in Figs. 4.16 and 4.24 the reduced etch-rate p is a non-linear function of REL. For example for CR39 up to REL ~500 MeV cm^2 g^{-1}, p changes slowly with REL, while a rapid increase is observed at larger values.

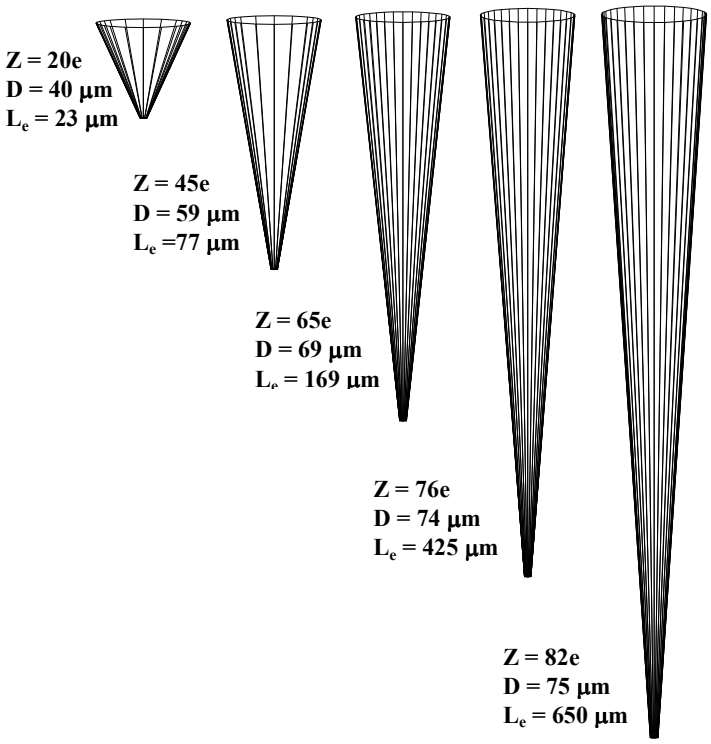

Fig. 4.22 The variation of cone height L_e and of the base diameter D for relativistic lead ions and their fragments measured in one sheet of CR39 [12].

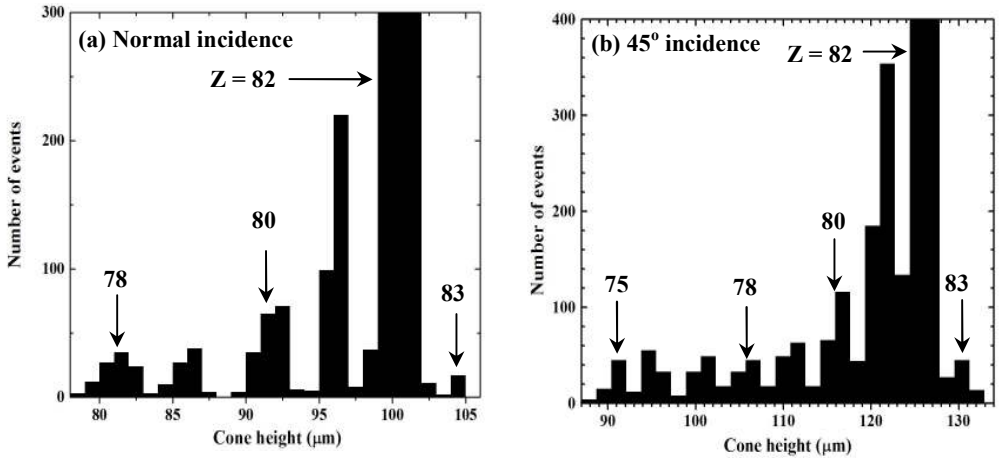

Fig. 4.23 Cone height distributions in Makrofol NTDs for 158 A GeV Pb^{82+} beam exposure for (a) normal incidence and (b) 45^o incidence angle (single measurements).

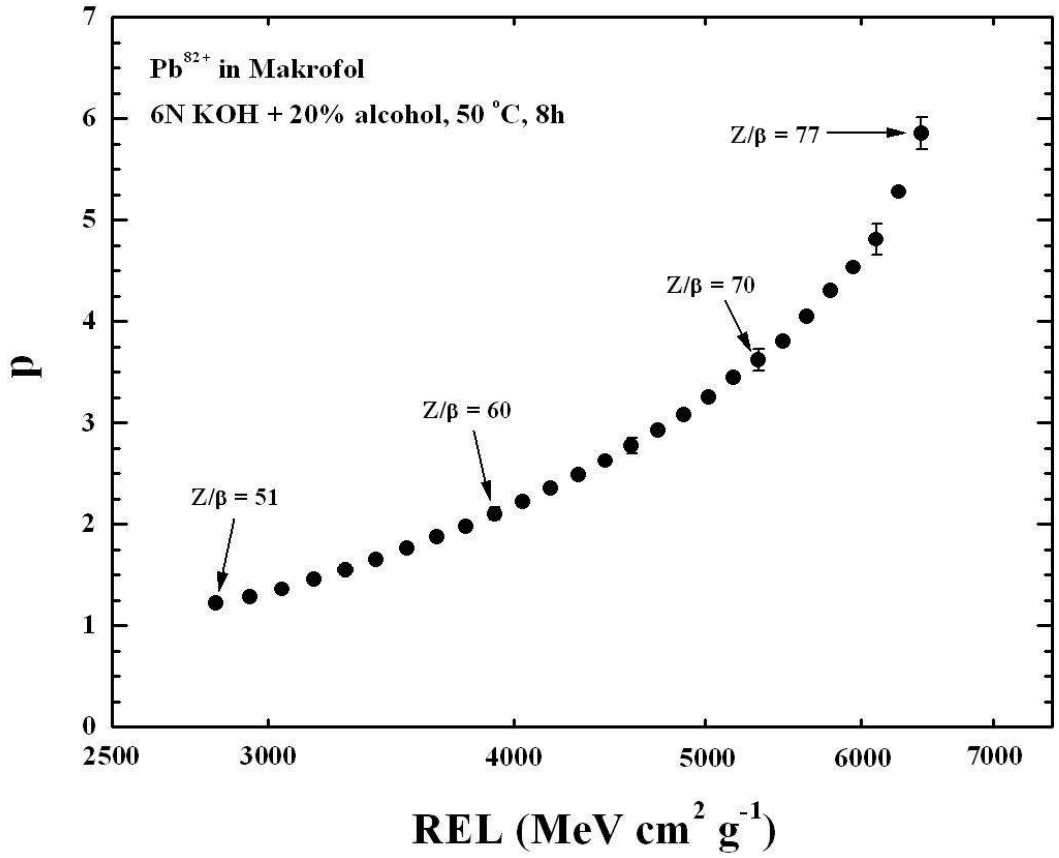

Fig. 4.24 p vs. REL for Makrofol detector exposed to relativistic Pb ions using v_B evaluated with the new method. Typical statistical standard deviations are shown at $Z/\beta = 70, 75, 77$; for $Z/\beta \leq 67$ the errors are inside the black points.

A comparison of the calibration curves for CR39 etched under soft etching conditions (with and without alcohol) is shown in Fig. 4.24. Both curves have the same response up to a charge value of 20. A sharp rise in the sensitivity is observed for CR39 etched with 1% alcohol.

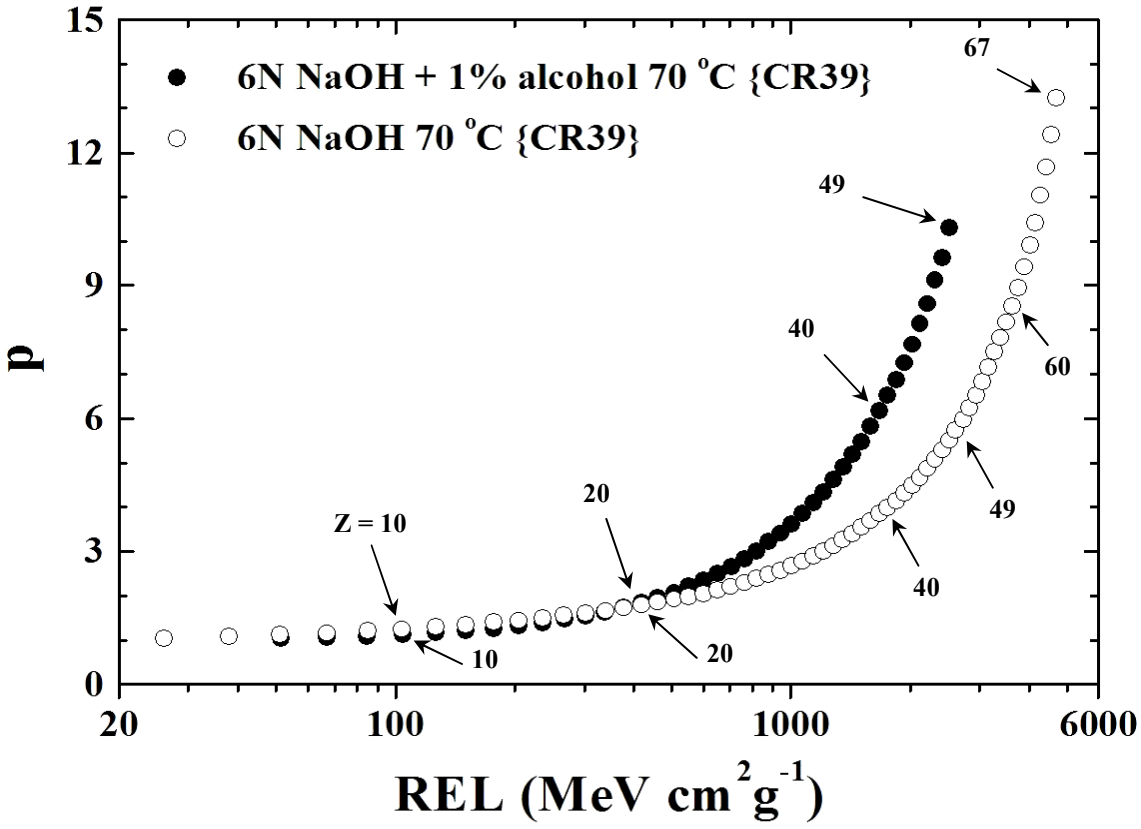

Fig. 4.25 Comparison for CR39 NTDs exposed to relativistic heavy ions and etched under different "soft" condition. Notice the p values at Z = 10, 20, 40 and 49 for two etching conditions for CR39. A sharp rise is evident for etching with alcohol after $Z/\beta > 20$.

4.7 Response Curves of CR39 to Relativistic Pb, Fe, Si and C ions

The same experimental procedure was used as mentioned above for the analysis of 158 A GeV Pb^{82+} , 0.41, 1 & 5 A GeV Fe^{26+}, 1 A GeV Si^{14+} and 0.29 A GeV C^{6+} heavy ions. For the determination of the bulk etch rate by the cone height and diameter method the CR39 sheets exposed to the relativistic Pb ions were used. For the low charge beams we used the bulk etch velocity measured by the change in thickness method (the cone height is not measurable due to the large cone opening angle; in this case cone tip is difficult to identify with optical microscope.

The distribution of bulk etch velocity of 67 CR39 NTDs is drawn in Fig 4.26. A Gaussian fit of the experimental data gives a mean value of $v_B \simeq 1.11 \pm 0.07$. The value is the same when measured using the new method (cone height and diameter measurement, see Table 4.4).

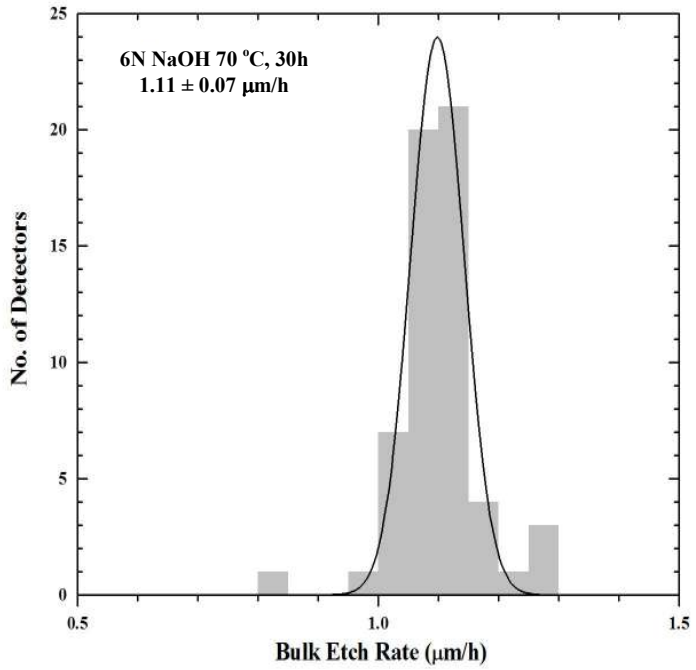

Fig. 4.26 Distribution of the bulk etch-rate for 67 CR39 detectors measured with the change in thickness method. The line is a Gaussian fit to the experimental data.

Histograms of the mean base areas for beams of 0.41 and 1 A GeV Fe and Si ions and their fragments in CR39 detectors etched in the same conditions (6N NaOH 70 ^{o}C 30 h) are drawn in the same scale for comparison, see Fig. 4.27. There are individual charge peaks with a minor shift in the mean area for the same nuclear fragment.

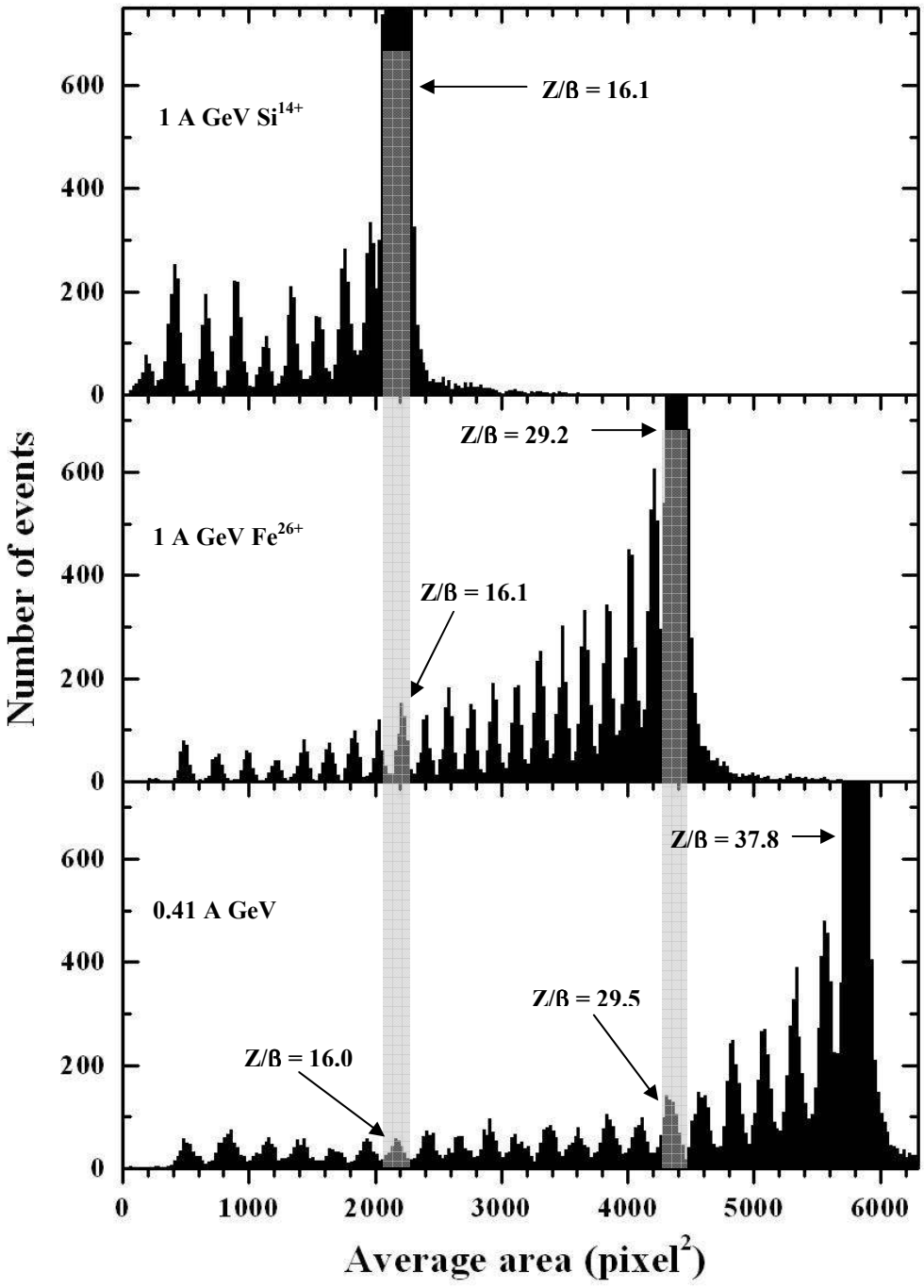

Fig. 4.27 Distribution of the etched cone base areas for CR39 NTDs located after the targets. Averages were made on three top faces. Well separated peaks are observed and a charge can be assigned to each individual peak. For a given nuclear fragment, we have about the same mean base area at different beam energies.

Figures 4.28 and 4.30 show the average base area distributions and scatter plots of 5 A GeV Fe^{26+} and of 1 A GeV Si^{14+} ions and their fragments tracked through 2 foils upstream and downstream of the target. Well separated peaks are observed and a charge can be assigned to each individual peak; some assigned charges are shown on each graph.

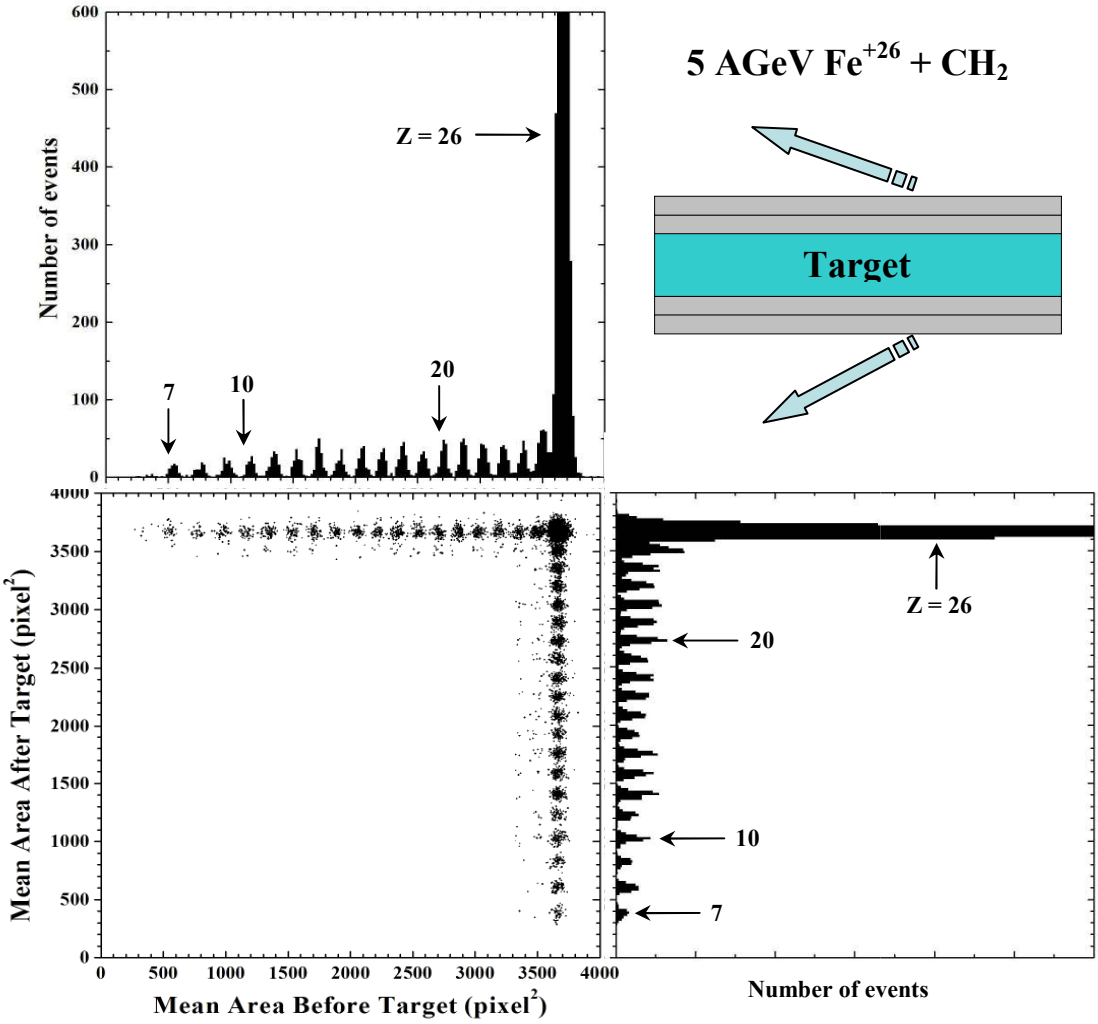

Fig. 4.28 Overall view of the analysis of 5 A GeV Fe^{26+} + CH_2: the average area distributions and the scatter plots of the CR39 sheets placed before and after the target are presented. Individual charges are clearly resolved down to Z = 7.

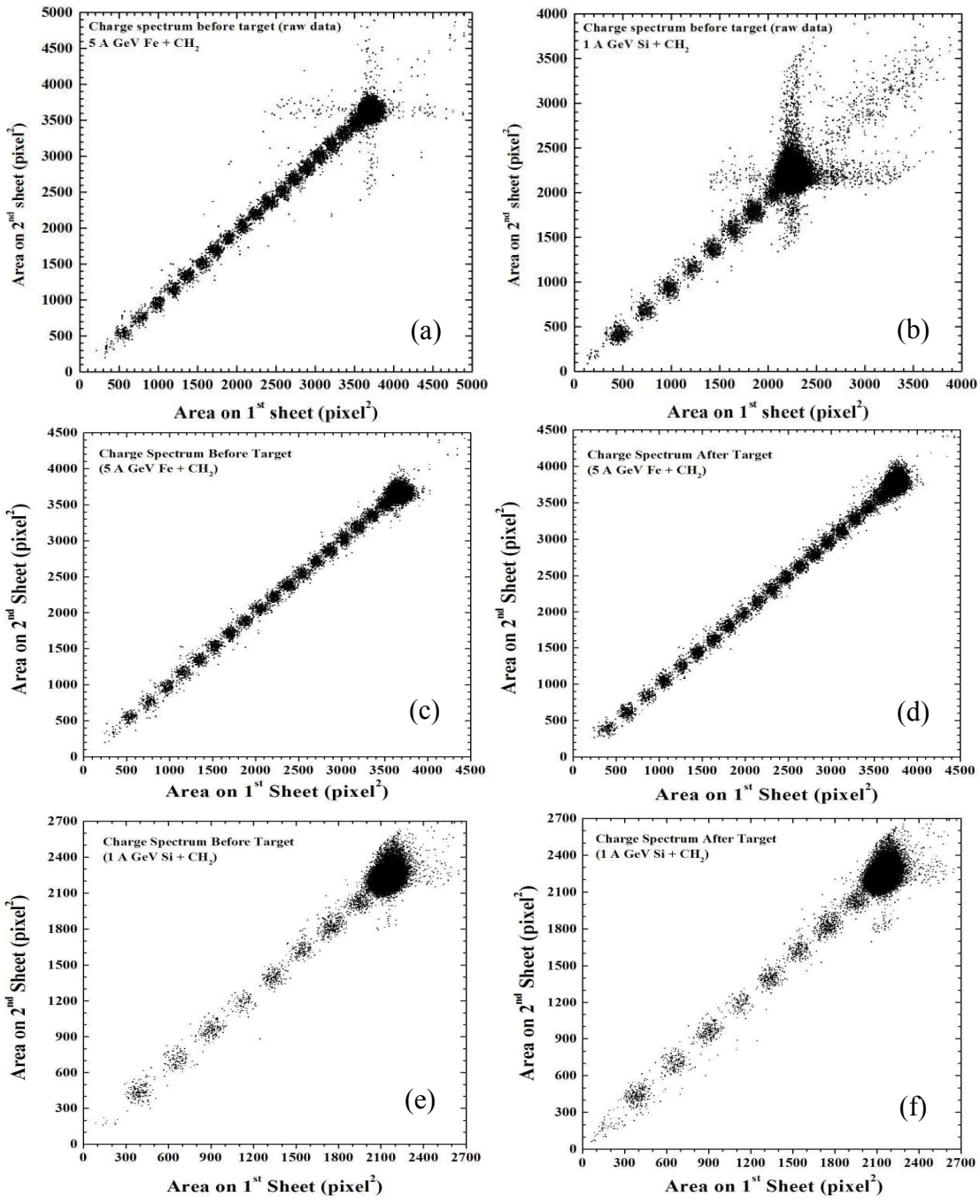

Fig. 4.29 Scatter plots of the base cone areas of the beam ions and fragments from 5 A GeV Fe^{26+} and 1 A GeV Si^{+14} in CH_2. (a, b) raw data of 5 and 1 A GeV Fe and Si ions before CH_2 target, (c,d) refined data of 5 A GeV Fe before and after the target and (e, f) are the refined data for 1 A GeV Si ions before and after the target, for details see text.

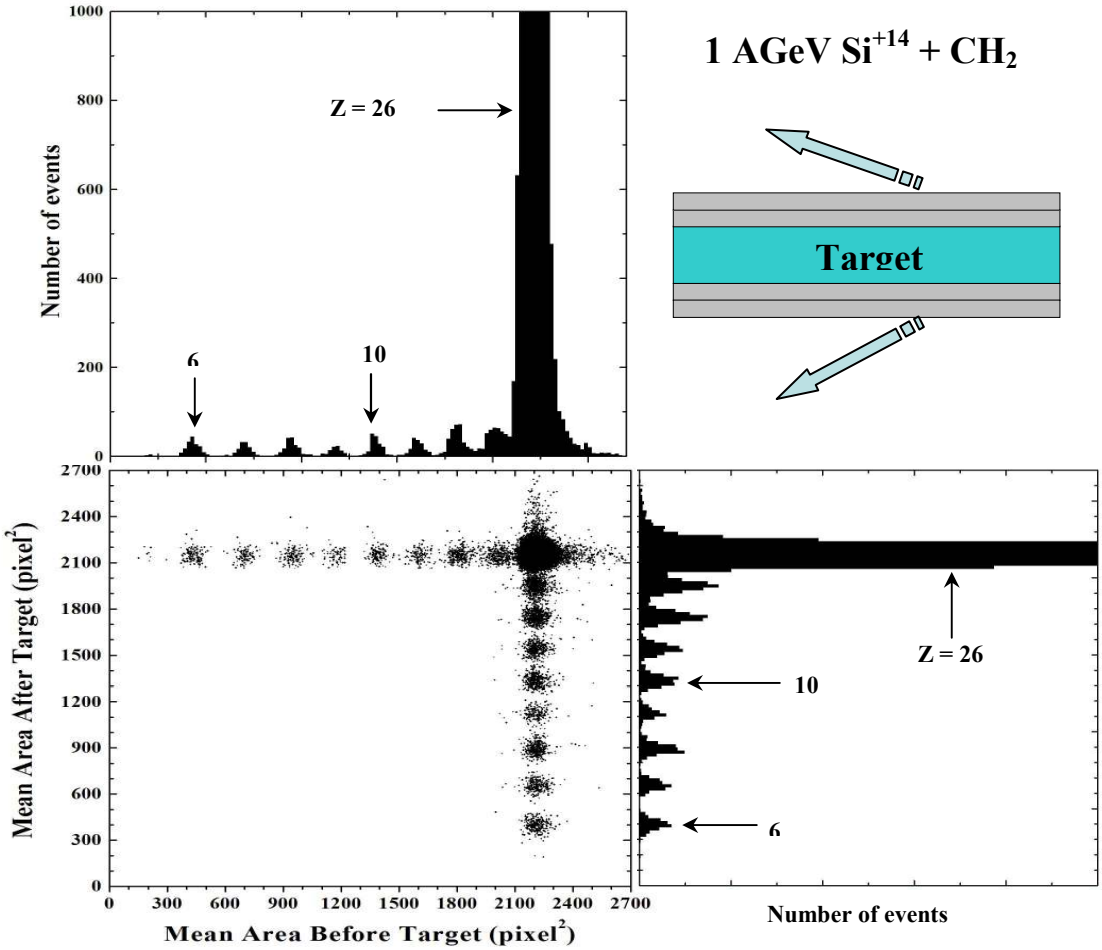

Fig. 4.30 Overall view of the analysis of 1 A GeV Si^{14+} + CH_2: the average area distributions and scatter plot of the CR39 sheets placed before and after the target are presented. Individual charges are clearly resolved down to Z = 6.

Figures 4.29 (a, b) show the scatter plots of raw data of the base cone area for 5 A GeV Fe^{26+} and of 1 A GeV Si^{14+} ions and their fragments on two front faces before a CH_2 target. Fig. 4.29 (c, d, e, f) shows the scatter plots for Fe and Si ions and their fragments after applying cuts on central brightness, eccentricity and the minimum difference in the area of the two sheets have been applied. Each cluster of scatter points corresponds to a charge. Twenty charge states are clearly visible for 5 A GeV Fe^{26+} and ten charge states for 1 A GeV Si^{14+}.

4.8 Charge Resolution

In this section the charge resolution and the response of the CR39 NTDs exposed to a wide range of relativistic heavy ions and their fragments will be discussed. Many charged fragments were produced in the fragmentation of incident ions inside the target.

Fig. 4.31 shows plots of the mean base areas of the fragments vs the assigned charges for the exposed detectors to relativistic ions as discussed in the previous section.

The charge resolution σ_z of the CR39 was calculated using eq. 4.6. The mean base areas for each assigned charge (z) and the charge resolutions (σ_z) are given in Table 4.5.

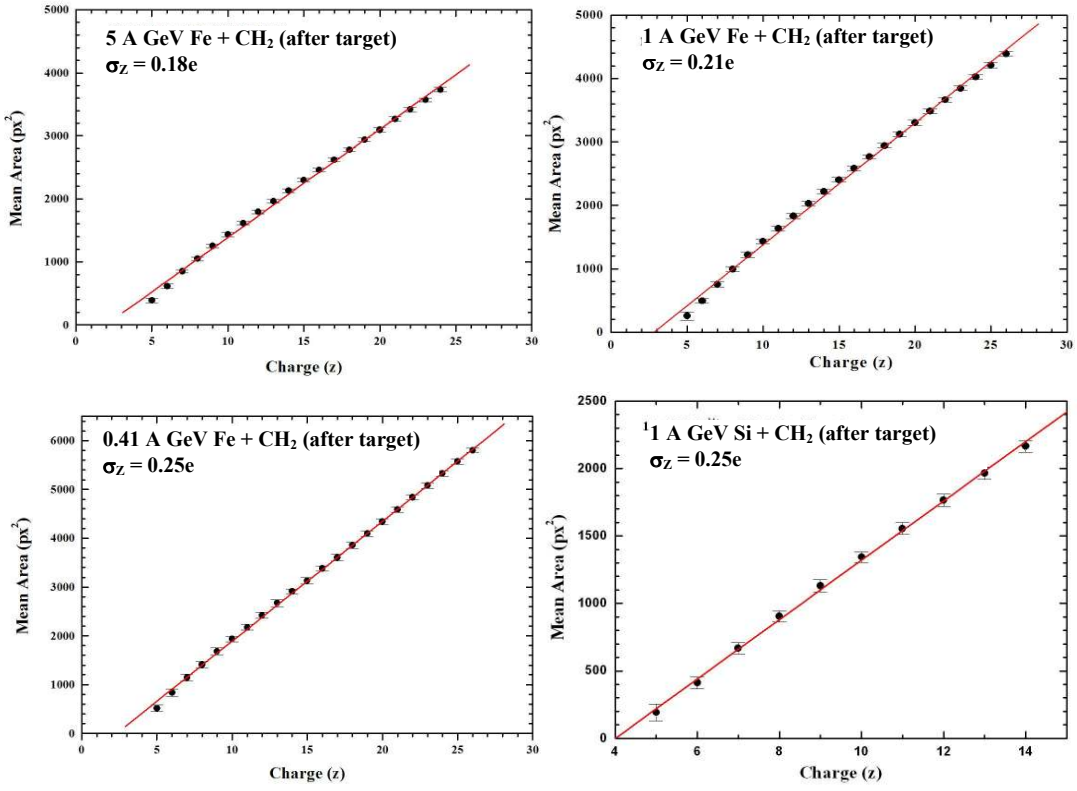

Fig. 4.31 Nuclear fragment charges vs etch pit mean base area for (a) 5 A GeV Fe^{26+}, (b) 1 A GeV Fe^{26+}, (c) 0.41 A GeV Fe^{26+} and (d) 1 A GeV Si^{14+} in CR39 NTDs.

Table 4.5 Mean base areas and charge resolutions σ_Z of nuclear fragment measured in CR39 NTDs using high energy Fe^{26+}, Si^{14+} and C^{6+} ion beams on a CH_2 target.

Z	*5 AGeV Fe^{26+}*		*1 AGeV Fe^{26+}*		*0.41 AGeV Fe^{26+}*		*1 AGeV Si^{14+}*		*0.29 AGeV C^{6+}*	
	Mean Area (pixel^2)	**σ_Z**	**Mean Area (pixel^2)**	**σ_Z**	**Mean Area (pixel^2)**	**σ_Z**	**Mean Area (pixel^2)**	**σ_Z**	**Mean Area (pixel^2)**	**σ_Z**
4	-	-	-	-	-	-	-	-	495	0.13
5	-	-	257	0.24	515	0.28	192	0.28	913	0.14
6	-	-	490	0.19	838	0.31	412	0.20	1278	0.11
7	391	0.22	746	0.22	1145	0.28	667	0.19		
8	612	0.20	988	0.21	1408	0.26	904	0.19		
9	850	0.14	1216	0.25	1679	0.29	1131	0.21		
10	1047	0.17	1428	0.21	1936	0.22	1344	0.18		
11	1253	0.16	1633	0.21	2173	0.26	1554	0.20		
12	1434	0.17	1829	0.20	2422	0.23	1765	0.21		
13	1614	0.16	2029	0.20	2669	0.30	1966	0.21		
14	1790	0.19	2214	0.19	2907	0.21	2165	0.20		
15	1960	0.18	2397	0.21	3130	0.28				
16	2128	0.18	2581	0.20	3378	0.22				
17	2297	0.18	2764	0.20	3606	0.28				
18	2458	0.18	2939	0.19	3855	0.24				
19	2620	0.18	3121	0.23	4095	0.25				
20	2782	0.17	3302	0.20	4336	0.23				
21	2939	0.18	3482	0.22	4589	0.24				
22	3095	0.17	3662	0.21	4840	0.22				
23	3265	0.21	3841	0.20	5082	0.23				
24	3418	0.19	4029	0.24	5326	0.24				
25	3570	0.19	4209	0.16	5571	0.23				
26	3733	0.21	4385	0.21	5804	0.18				

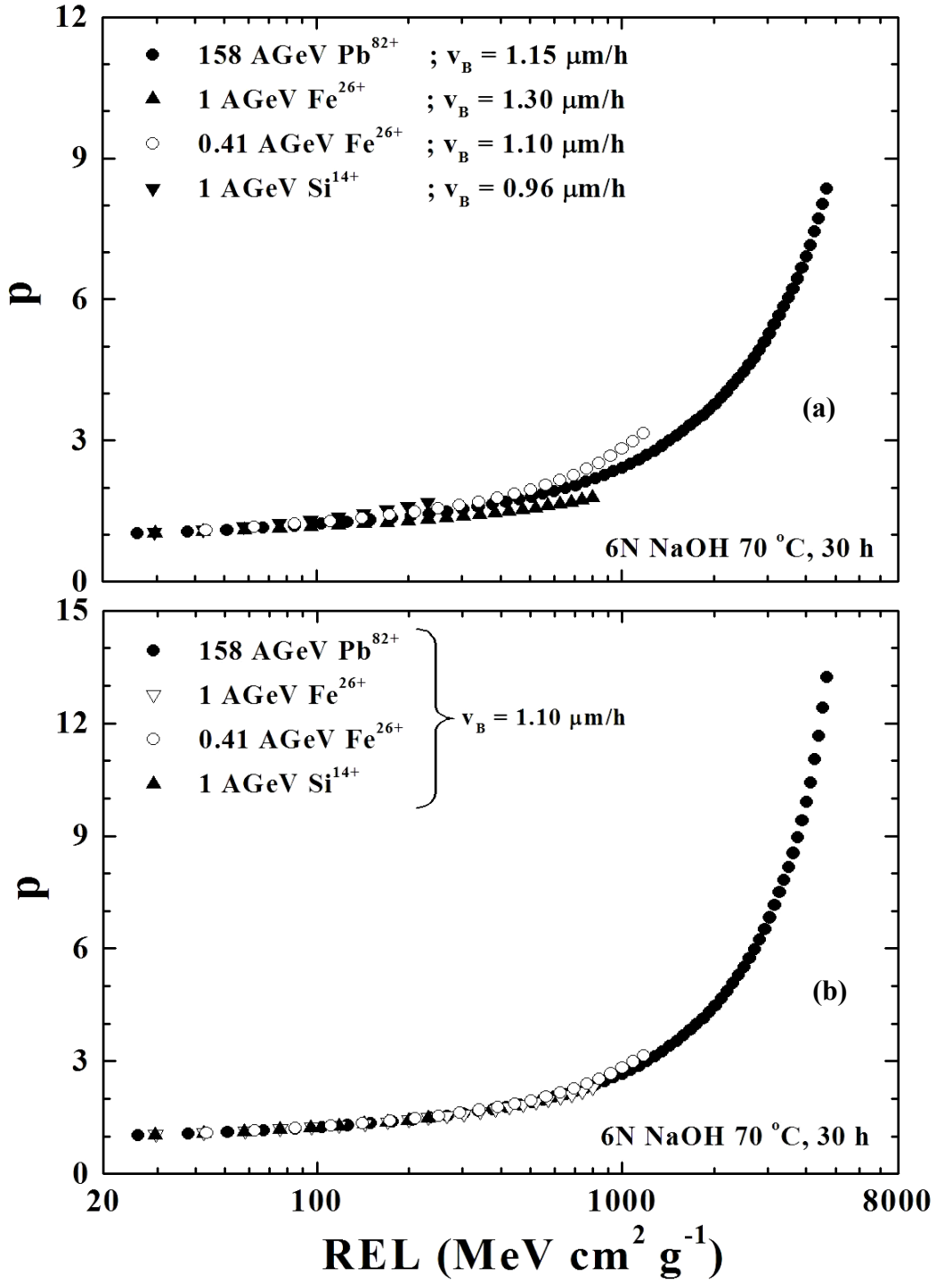

Fig. 4.32 p vs REL for CR39 NTDs exposed to Pb, Fe, Si and C ions of different energies. (a) by thickness method and (b) by new method for computing the bulk etch velocity v_B.

Better charge resolution σ_Z ~0.13 to 0.18e can be achieved by measuring three top faces of CR39 sheets exposed to 0.29 A GeV C and 5 A GeV Fe ions and their fragments. A lower charge resolution ($\sigma_Z = 0.21 \pm 0.03$) has been obtained for 1 A GeV Fe and Si ions and their fragments measured on three front faces of CR39 sheets. The charge resolutions can be improved by measuring more faces of CR39 sheets.

The etched rate ratio p was calculated by the old and by the new method (track diameter and cone height measurements). Fig. 4.32a,b show p vs REL for C^{6+}, Si^{14+}, Fe^{26+} and Pb^{82+} ions and their fragments in CR39. It is observed that all the experimental data points are not lying on one curve because of different bulk etch-rate velocities.

Fig. 4.32b shows the p vs REL, with p calculated by taking the mean $v_B = 1.10 \pm 0.02$ by the new method (see Table 4.3). All the experimental data points are on a single curve. The REL of charged particles can be used as a convenient criterion to predict the formation of an etchable track in plastics.

5. The SLIM experiment

5.1 Introduction

The SLIM experiment, planned for the search for IMMs and SQM, is based on 440 m^2 of NTDs installed at the Chacaltaya high altitude cosmic ray laboratory (Bolivia, 5230 m a.s.l.) since 2000, Fig. 5.1a, and 100 m^2 more installed at Koksil, Himalaya (Pakistan, 4275 m a.s.l.) since 2002, Fig. 5.1b. The detectors are organized in wagons (modules) of 24 cm x 24 cm, each made of 3 layers of CR39 (1.4 mm thick), 3 layers of polycarbonate (Makrofol, 0.5 mm thick) and of an aluminium absorber (1 mm thick); each module is sealed in an aluminized plastic bag filled with dry air at 1 atm pressure; the composition of a SLIM wagon is shown in Fig. 5.2b. Since the atmospheric pressure at Chacaltaya is ~0.5 atm, a test was made in which some aluminized plastic bags filled with 1 atm of dry air were sealed and placed in a chamber at a pressure of about 0.3 atm for three weeks; no leakage was observed.

Fig. 5.1 The sites of the SLIM experiment: (a) Chacaltaya, Bolivia (5230 m a.s.l.) and (b) Koksil, Himalaya, Pakistan (4275 m a.s.l.).

The CR39 NTDs are used for the possible detection of Dirac charge ($g = g_D$) MMs with β around 10^{-4} and $\beta > 10^{-3}$ (most of the whole β range, $\beta > 10^{-4}$, for magnetic charges $g \geq 2g_D$, dyons and for SQM). The second and third layers of CR39 and all Makrofol NTDs are used for confirmation of possible candidates.

The radon concentration in the experimental sites was measured using E-PERM (at the Chacaltaya site) and CR39 radon dosimeters (at the Koksil site). It was found to be about 40 - 50 Bq/m^3 at both places; such levels of radon concentrations do not give any major problem in terms of background tracks in the detectors.

The cosmic ray neutron flux with energy $1 < E_n < 20$ MeV was also measured with BF_3 gaseous detectors (Chacaltaya site) and with CR39 nuclear track detectors (Koksil site). We obtained $\Phi_n = (1.7 \pm 0.8)\ 10^{-2}$ cm^{-2} s^{-1}, in agreement with other reported neutron flux data at the Chacaltaya altitude. At Koksil a flux of $(6.0 \pm 1.0)\ 10^{-3}$ cm^{-2}h^{-1} was measured. The neutron flux could give some background problems.

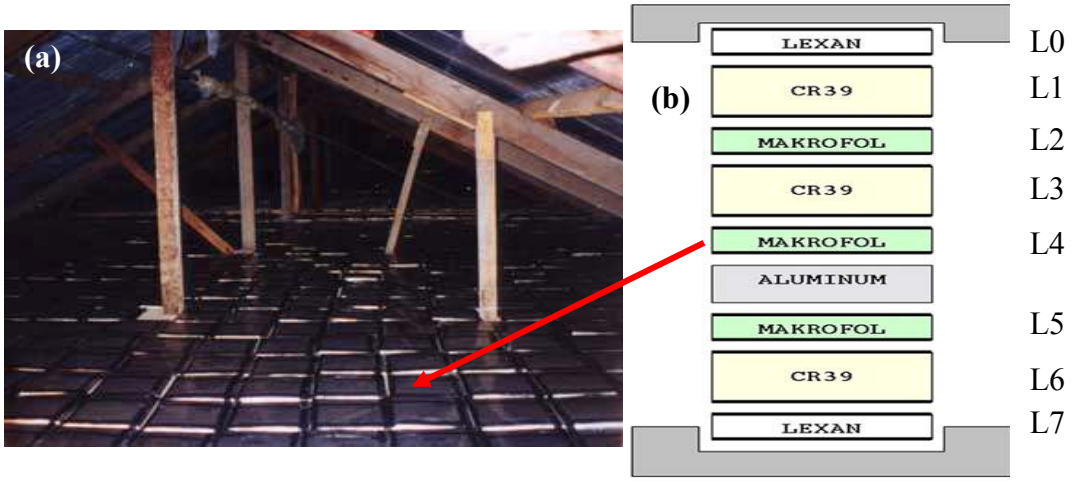

Fig. 5.2 (a) The SLIM modules installed at Chacaltaya and (b) sketch of the composition of one module. The whole module is enclosed in an aluminized plastic bag filled with dry air at 1 atm pressure.

The CR39 and Makrofol detector calibrations are discussed in chapter 4. For soft and strong etching conditions with alcohol the thresholds for CR39 are at REL

~50 MeV cm^2 g^{-1} and ~300 MeV cm^2 g^{-1}, respectively. The Makrofol polycarbonate has a higher threshold, at REL ~2.5 GeV $cm^2 g^{-1}$ [90, 92, 72, 73].

5.2 Analysis of SLIM NTDs

After an exposure of ~4 years at the high altitude labs, the SLIM modules were brought back to Bologna, Italy (from Chacaltaya) and to PINSTECH, Pakistan (from Koksil). The exposed SLIM wagons were etched in the Bologna and PINSTECH etching laboratories. Three fiducial holes of 2 mm diameter are drilled in each wagon with a precision drilling machine to an accuracy of 100 μm. The bags are opened and the detector layers are labelled (see Fig. 5.2b). The thickness of the top CR39 (labelled L1) is measured at 8 uniformly distributed positions before etching. It is etched in "strong" etching conditions (8N KOH + 1.5% alcohol, 75 ^oC 30 h) to reduce the thickness from 1.4 mm to ~0.9 mm. MMs and nuclearites have a constant REL therefore one expects a signal in the form of either a hole or collinear etched holes of the same size on both sides of the detector, depending on the etching conditions. After etching the L1 sheets are scanned with a stereo binocular microscope at 8× magnification (0.8x objective and 10x eye piece) looking for tracks as shown in Fig. 5.3: any "interesting track" is marked on each sheet for further analysis.

Marked tracks are then observed with an optical microscope at 200-400x global magnification and classified either as defects or signal tracks. Signal tracks are further observed at a higher magnification and the minor *axes* of the base-cone ellipse in the front (A_{front}) and back (A_{back}) sides *are* measured. We require that $|A_{front}/A_{back}-1| \leq 3$ times the standard deviation of the difference.

Different track shapes were observed in the top CR39 layer of the SLIM modules, see the photos in Fig. 5.4. They are all from low energy stopping particles entering from the top or bottom side of the CR39 sheets; they are due to nuclear recoils induced by cosmic rays neutrons, muons and pions.

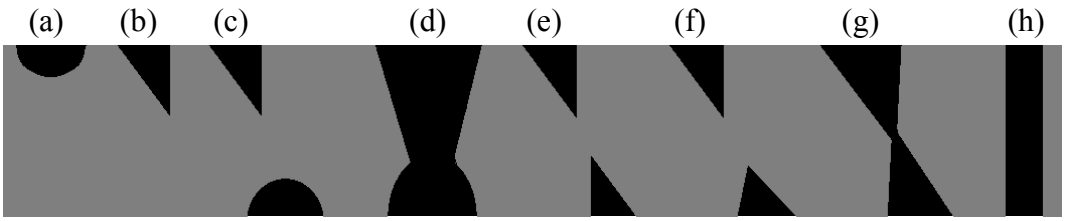

Fig. 5.3 Classifications of tracks in the SLIM CR39 NTDs after strong etching (cross sectional view); (a) a "bubble" from a plastic defect, (b) a track due to a stopping particle, (c) on one side a stopping particle track and on the other side an over etched track or a bubble, (d) a hole due to an end of range and an over etched track, (e) accidental coincidence of two stopping particle tracks, (f) two end of range tracks or a track, (g) and (h) a high REL candidate track at the different etching steps.

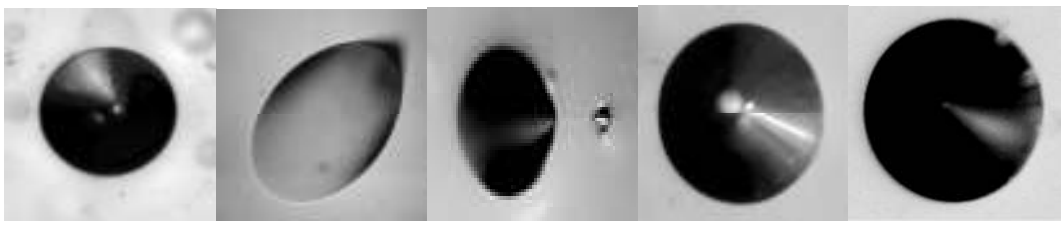

Fig. 5.4 Different track shapes as observed in the SLIM CR39 sheets after strong etching.

In order to evaluate the p values and the incident angles θ for the front and back sides, the track minor and major axes are measured. A track is defined as a "candidate" if p and θ on the front and back sides are equal to within 15%. For each candidate the azimuth angle φ and its position P referred to the fiducial marks are determined. The uncertainties Δθ, Δφ and ΔP define a "coincidence" area (< 0.5 cm^2) around the candidate expected position in the other layers of the SLIM modules (see Fig. 5.5).

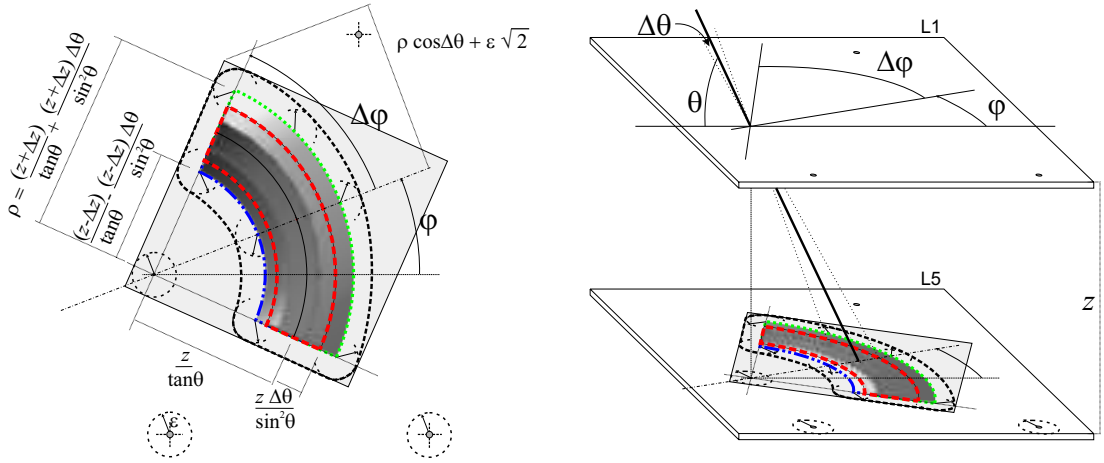

Fig. 5.5 The procedure used for the 'confidence' area in which a possible candidate track located on the top layer will be searched for in other layers of the same module.

The lowermost CR39 layer is then etched in "soft" conditions (6N NaOH + 1% ethyl alcohol, 70 ^{o}C 40h) and an accurate scanning with an optical microscope at high magnification is done in a squared region around the candidate expected position, which includes the "confidence" area. If a two-fold coincidence track was detected all geometrical parameters are measured; the middle CR39 layer would also be analyzed using the same procedure.

5.2.1 Non Confirmable Strange Events

In the past, a number of magnetic monopoles and other exotic candidate events were quoted and few results were also published [93], but none of these results were confirmed.

We observed a strange event in the first layer (L1) of the SLIM module 7408 after strong etching of the CR39 sheet.

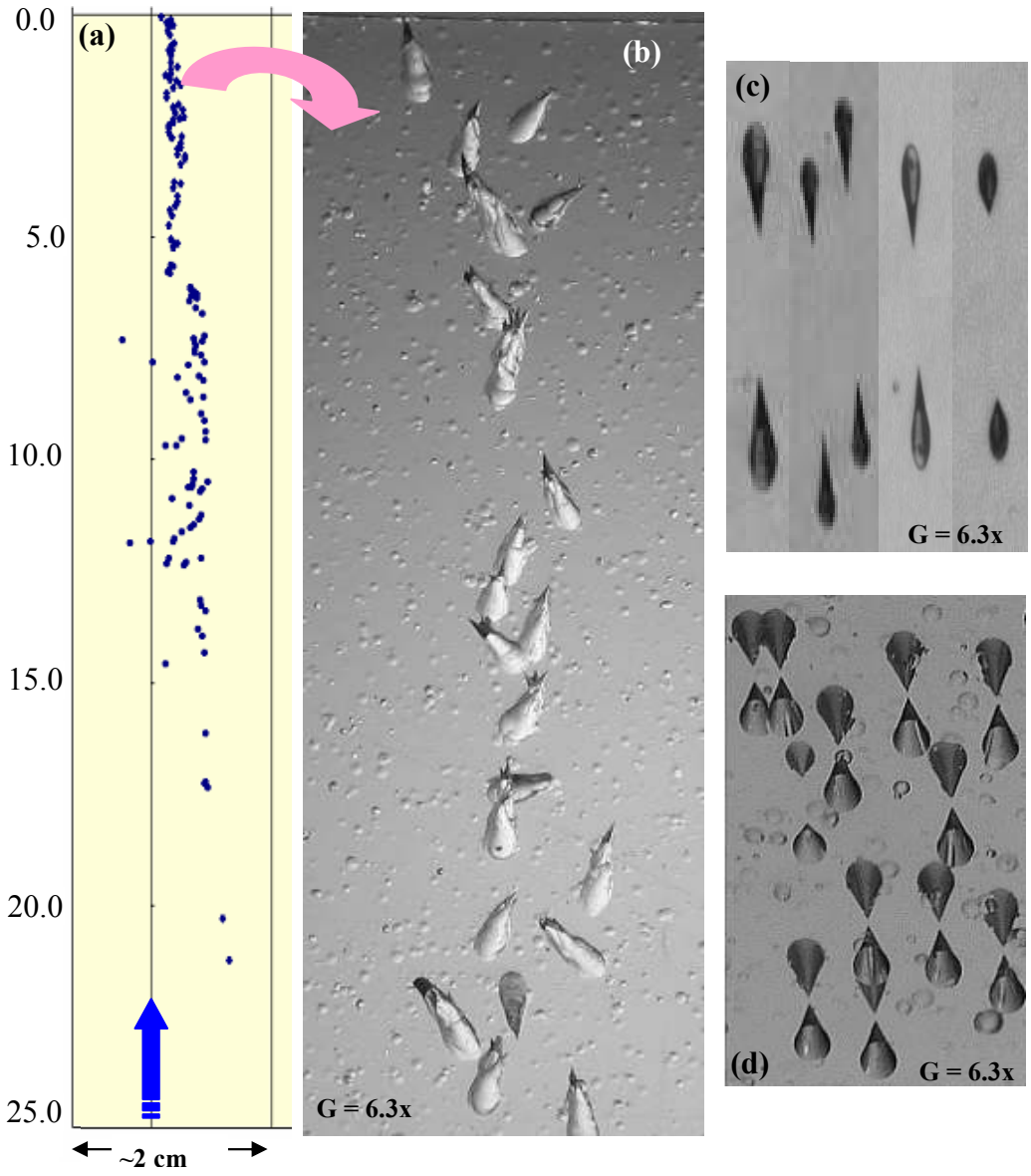

Fig. 5.6 (a) Global view of the event/background tracks in the L1 layer of wagon 7408 exposed at Chacaltaya from 20-2-01 to 28-11-05 (etched on 9-6-06), (b) microphotographs of the 1-22 tracks at the top of Fig. (a). (c) Normal tracks of 158 A GeV $^{+82}$Pb ions and their fragments from a CERN-SPS exposure (soft etching), and (d) of 400 A MeV $^{+26}$Fe ions and their fragments from the HIMAC accelerator, Japan (strong etching).

We found a sequence of many tracks along a 20 cm direction of the strange event (see Fig. 5.6a, b); each of them looked complicated and very different in shape

from the usual heavy ion tracks in CR39. For comparison tracks from 158 A GeV Pb ions and their fragments and tracks from 400 A MeV Fe ions and their fragments are shown in Fig. 5.6c, d, respectively. We measured the track lengths and the angles of few tracks along the strange event; the average total cone length is L = 651μm and the average zenith angle is 38°. In Fig. 5.7 are shown seven tracks of the stranger event in the L1 sheet of module 7408. Notice their very strange shapes: the tracks seem to be made by several prongs, with some ending their range and others with very sharp cones at the end of their tracks.

Fig. 5.8 shows the SLIM module layout in one of the "halls" at Chacaltaya. Since the "event" in the L1 sheet of module 7408 is rather peculiar, we immediately started a series of cross checks analyzing all the stacks and sheets around stack 7408 (within a ~1m distance from 7408).

All the sheets from the selected wagons were etched softly in order to follow the evolution of the tracks. We found an anomalous scratch-like event on the top face of L6 (CR39 bottom layer) layer of module 7410 after 30 h of etching (Fig. 5.9a).

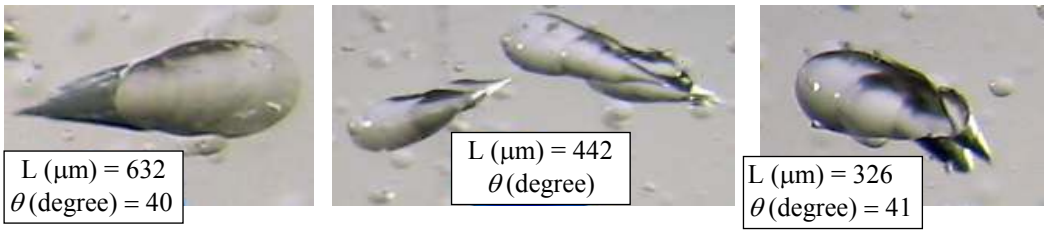

Fig. 5.7 Micro photographs of selected tracks of the stranger/background event (G = 16x).

We decided to further etch strongly the 7410-L6 layer in short time steps (5 hr.) and to follow the evolution of the "tracks" after each etching step, systematically making photographs with a stereo-microscope. After 5 h of additional strong etching the "tracks" start to look-like those in the 7408-L1 layer, see Fig. 9b. After more 4 and 10 hours of strong etching (Figs. 5.9 c,d) the tracks are even more similar to those in the L1 sheet of module 7408.

Fig. 5.8 *(a) Layout of the SLIM modules near module 7408 and (b) the positions of the SLIM modules inside a wooden box during the flight Bologna-La Paz and La Paz-Bologna.*

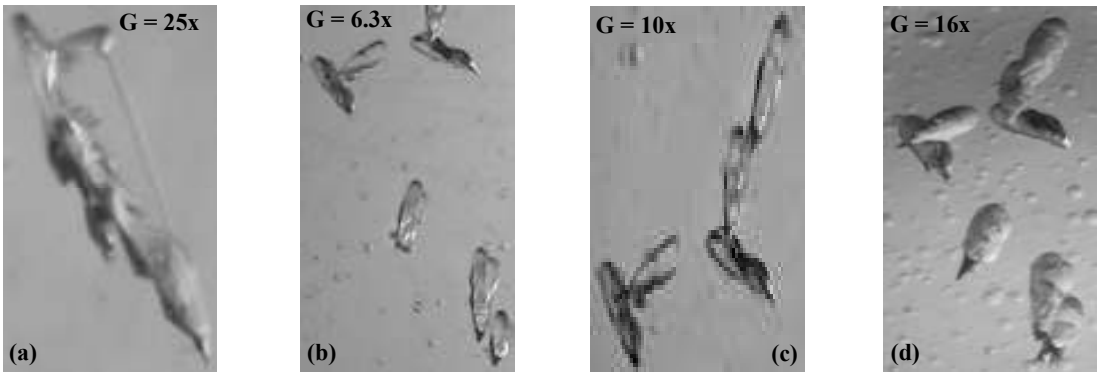

Fig. 5.9 *Examples of "tracks" in the L6 layer of wagon 7410 (see Fig. 5.6): (a) after 30 h of soft etching, observed at a magnification of 25x, (b) after 5 more hours of strong etching, (c) after 4h of more strong etching and (d) after 10h of more strong etching.*

The presence of this second event/background and its evolution with increasing etching casts stronger doubts on the first event/background.

Moreover we inspected before and after etchings all the sheets in the modules located close to 7408. We found at least one small translucid spot on one un-etched foil, suggestive of a small piece of glass on the surface: this background disappeared after the first soft etching; the same happened for a couple of other surface defects. For three single surface impurities observed before etching in modules 7325 (L3), 7332 (L3) and 7339 (L3), we noticed that after soft and strong etching they yielded tracks which resemble those in Fig. 5.6 and 5.9.

The presence of the second "event/background" in stack 7410 and the observations made after different etching times and the three single background tracks cast strong doubts on an event interpretation and supports a "background" interpretation of the first "event". The background may have originated in the fabrication of the CR39: we made different hypotheses and we checked them with the Intercast Co. The most plausible hypothesis seems to be the following: the monomer solution is poured within two casting glass plates separated by a gasket. At the end of the curing cycle, at the moment of detachment of the foil from the glass moulds and the gasket, some small pieces of the not perfectly cured material around the gasket could have been electrostatically deposited on the CR39 surface; then they may have been pressed onto the surface of CR39 by the rolling machine which presses a thin transparent protective film on both sides of CR39.

We have analyzed more than 400 m^2 of CR39 using different etching conditions and we have not seen before any of the above mentioned cases. We conclude that we may have seen a very rare manufacturing defect involving 1 m^2 of CR39.

5.3 SLIM Acceptance and Limits for the Search of IMMs and Nuclearites

5.3.1 Acceptance of the Detector

The acceptance of the SLIM detectors was calculated by assuming an isotropic flux of magnetic monopoles. The geometrical acceptance of a NTD for an isotropic flux of particles is given by

$$S\Omega = \int_0^{\theta_c} \cos\theta \sin\theta d\theta = 2\pi S\left(1 - \cos^2 \theta_c\right) \tag{5.1}$$

where S is the detector area of the and θ_c is the limiting angle for monopoles. The critical or limiting angle is (eq. 2.11)

$$\sin\theta_c = -\cos\theta_c = \frac{1}{p} \tag{5.2}$$

By comparing eqs. 5.1 and 5.2, the detector acceptance for a downgoing isotropic flux ($\Omega = \pi$) is given by

$$S\Omega = \pi S\left(1 - \frac{1}{p^2}\right) \tag{5.3}$$

From the detector calibrations, p vs REL, in soft etching conditions (see Fig. 4.24) and the REL vs β acceptance for MMs (see Fig. 3.7) we computed the acceptance of the SLIM detector for downgoing IMMs with $g = g_D$, $2g_D$, $3g_D$ and for dyons; the results are shown in Fig 5.10a,b (in soft and strong etching conditions).

Since no IMM candidate was found the flux upper limit at 90% confidence level (C.L.) is

$$\Phi = \frac{2.3}{(S\Omega.\Delta t)\varepsilon} \tag{5.4}$$

where Δt is the exposure time and ε is the scanning efficiency of the detector, which double scannings we estimated to be ~99% for IMMs.

5.3.2 SLIM Limits

We have analyzed an area of 380 m^2 with an exposure time of 4.04 y at Chacaltaya. No IMMs and nuclearite candidates were found; the 90% C. L. flux upper limits for downgoing fast IMM's with β >0.02 is at the level of $\Phi < 1.51\ 10^{-15}$ cm^{-2} sr^{-1} s^{-1}. The flux upper limits for IMMs with g = g_D, $2g_D$, $3g_D$ and M+p from above vs β are plotted in Fig 5.11.

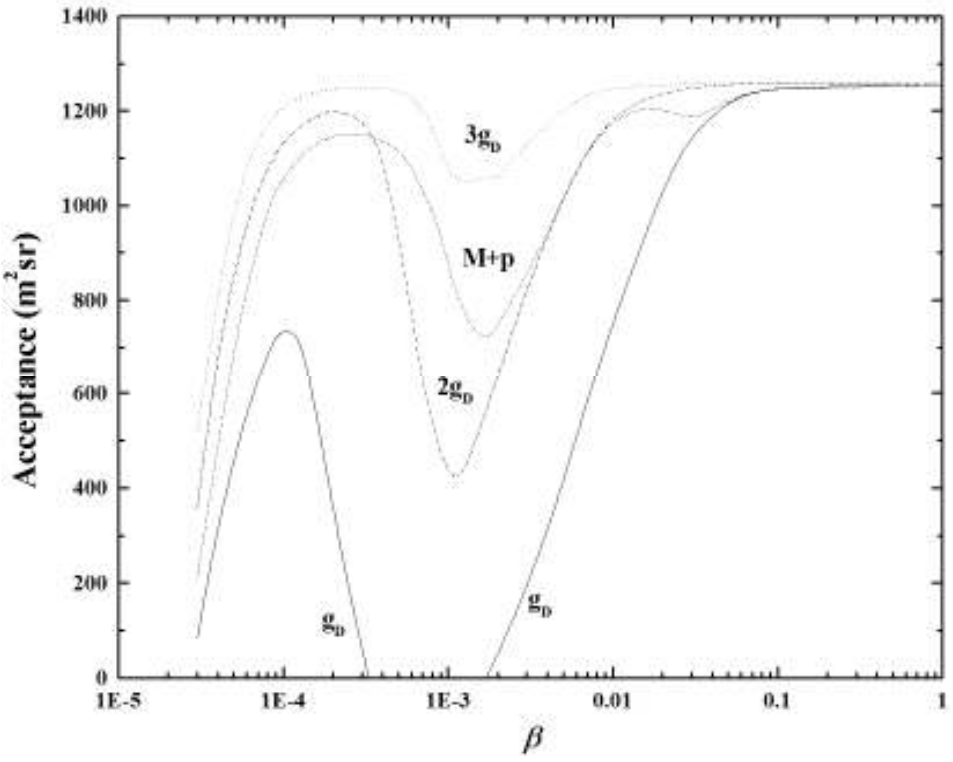

Fig. 5.10a SLIM detector acceptance (for 400 m^2) for downgoing IMMs with g = g_D, $2g_D$, $3g_D$ and dyons (M+p) (soft etching conditions).

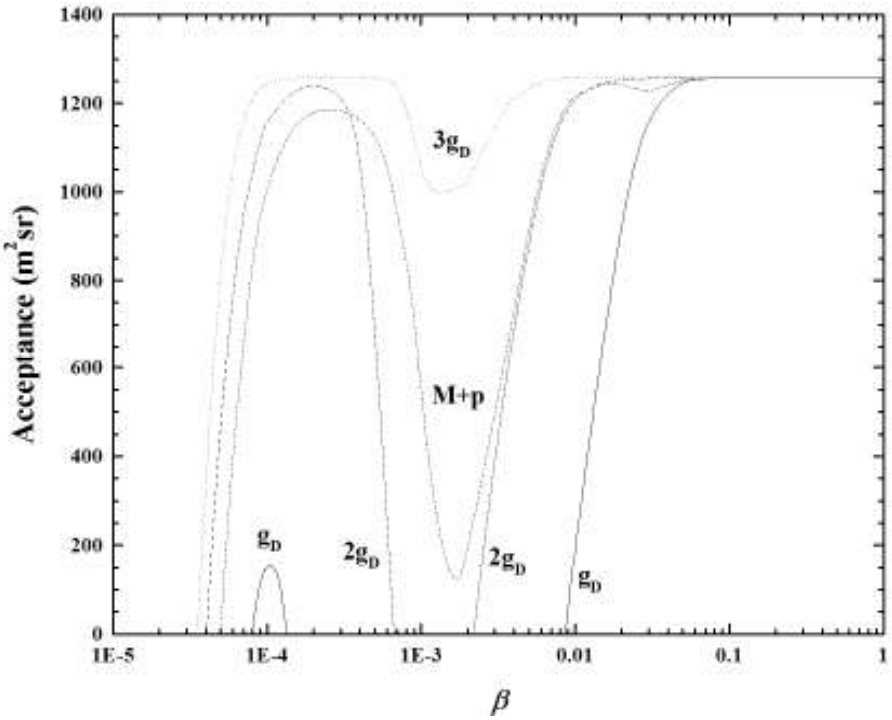

Fig. 5.10b "Strong" etching SLIM detector acceptance (for 400 m^2) for downgoing IMMs with g = g$_D$, 2g$_D$, 3g$_D$ and dyons (M+p) (strong etching conditions).

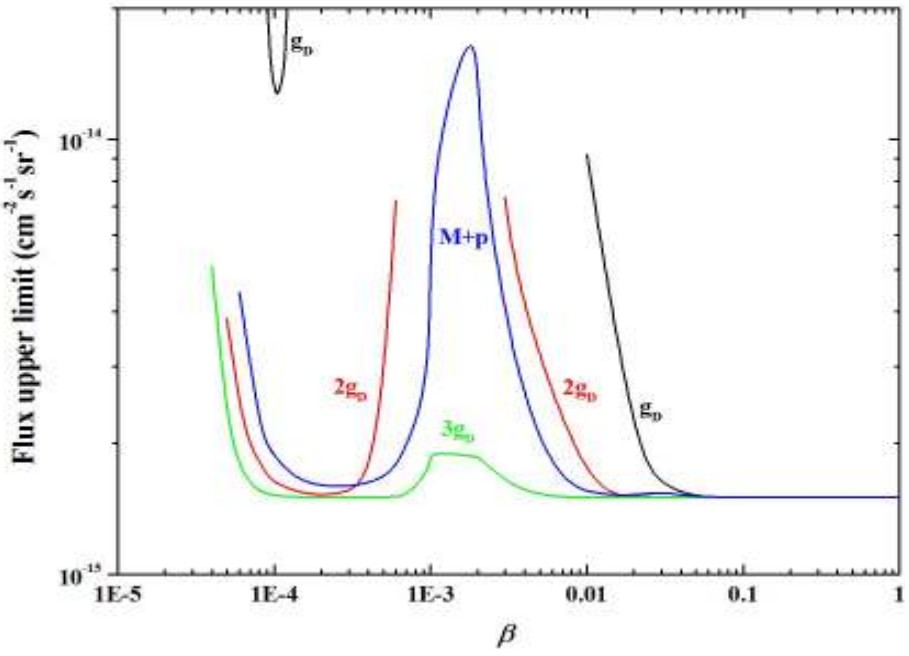

Fig. 5.11 90% C.L. flux upper limits for downgoing intermediate mass magnetic monopoles with g = g$_D$, 2g$_D$, 3g$_D$ and M + p (strong etching condition) (380 m^2 analyzed).

6. Fragmentation Cross Sections

6.1 Introduction

The availability of relativistic heavy ion beams at the CERN SPS, BNL and HIMAC facilities have made it possible to investigate the projectile fragmentation on different targets and for different incoming energies. Experimental results on charge changing cross sections give information on "peripheral reactions" at relativistic energies. The total reaction cross sections can give important informations on many fields, including cosmic ray propagation, appropriate radiation shielding in space or at accelerators, radiobiological effectiveness, etc. The fragmentation cross sections are needed to evaluate the changes in composition undergone by cosmic ray particles in the collisions with the atomic nuclei of the interstellar medium. Plans for the construction of Ultra Relativistic Heavy Ion colliders must take into account the expected large total dissociation cross sections, since this process can be an important mechanism for beam losses in such machines.

A number of authors [94-98] have successfully used NTDs for the systematic measurement of nuclear fragmentation cross sections. For this purpose we have used CR-39 detectors which can detect a wide range of charges down to Z=5e in the relativistic energy region [12, 88].

Based on the identification of the charges of the fragments we have calculated the total charge changing cross sections of Lead, Iron and Silicon ions in different target materials. Section 6.2 illustrates the experimental procedure; in the next section, the results on calibrations and on total and partial cross sections are discussed.

The fragmentation process takes place when a beam of heavy ions is incident on a target. The emitted fragments are classified as projectile and target fragments. The target fragments carry a relatively small momentum. The projectile fragments

travel with nearly the velocity of the beam, with small deflections, and have a lower charge compared to that of the incident nuclei.

Fragmentation of relativistic ions occurs in targets through two mechanisms. One is the electromagnetic dissociation (EMD) and the other is nuclear spallation (NS). The first channel plays an important role in the case of heavy projectiles and heavy targets: it occurs when a projectile nucleus passes close to a heavy target nucleus. For relativistic ions one has a violent electromagnetic pulse incident on the projectile [95]. For lighter targets, the role of EMD in fragmentation is much weaker.

6.2 Nucleus-Nucleus Total Charge Changing Cross sections

The expression for the total reaction cross sections, derived by Bradt and Peters [99], gives relatively accurate values for the total charge changing cross sections. In this model the incident and target nuclei are represented as two hard spheres colliding with a small overlap; the total cross section is

$$\sigma(A_P, A_T) = \pi r_o^2 \left(A_P^{1/3} + A_T^{1/3} - b_o\right)^2 \qquad (6.1)$$

A_P and A_T are the projectile and target mass numbers, respectively; b_o is the overlap or transparency parameter (see Fig. 6.1); r_o is the constant of proportionality for the nuclear radius $r_i = r_o A_i^{1/3}$; both b_o and r_o are energy-independent parameters.

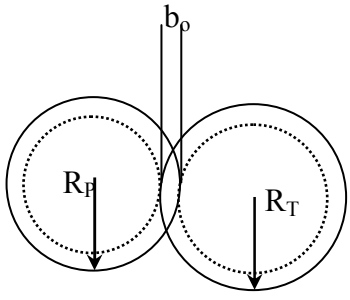

Fig. 6.1 The geometric view of nucleus – nucleus interaction. The figure shows the projectile and target nuclei of radii R_P and R_T, and the overlap parameter b_o.

A modified form of the Bradt-Peters formula was suggested by Barshay et al., [99] to account for the observed nucleus-nucleus reaction cross sections

$$\sigma_{tot} = \pi r_o^2 \left(A_P^{1/3} + A_T^{1/3} - b_o \left(A_P^{-1/3} + A_T^{-1/3} \right) \right)^2 \qquad (6.2)$$

Sihver et al. [99] used this formulation: however, instead of a constant value of b_o, they parameterized it as a first order polynomial in $\left(A_P^{-1/3} + A_T^{-1/3} \right)$, while maintaining the assumption that it is energy-independent (for E ≥ 100 A MeV), they find $b_o = 1.581 - 0.876\left(A_P^{-1/3} + A_T^{-1/3} \right)$

6.2.1 Exposure and Data Analysis

Six stacks composed of CR39 NTDs, of size 11.5 x 11.5 cm^2, and different targets were exposed at the CERN-SPS to 158 A GeV Pb^{82+} ions (see Fig. 6.2). Twelve stacks composed of CR39 and with different targets were exposed to 10, 5, 3, 1 and 0.3 A GeV Fe^{26+} ions, 5, 3 and 1 A GeV Si^{14+} ions at BNL, 0.41, 0.14 A GeV Fe^{26+} ions and 0.29 A GeV C^{12+} ions at HIMAC, Japan (see Fig. 6.3).

For the CERN exposures, three CR39 sheets, 1.4 mm thick, were placed in the A and B sections of Fig. 6.2. Twelve CR39 sheets, 0.6 mm thick, were located between "A" and the target 'a' section, and 24 CR39 sheets, 0.6 mm thick, were placed after the target 'b'. The 3 CR39 sheets in 'A' detected the total number of incoming Pb ions. The 12 CR39 sheets in 'a' detected the incident beam ions and fragments produced in the CR39. The target thickness was typically one half of the ion mean free path. The 24 CR39 sheets in 'b' recorded the surviving beam ions and their fragments. The exposures were done at normal incidence, with a density of ~2000 ions/cm^2. Table 6.1 gives information on the target parameters of each stack.

For the Fe and Si exposures at BNL we placed three CR39 sheets, 0.65 mm thick, before the target and nine sheets after the target; for the Carbon exposure at HIMAC, one CR39 sheet was placed before and three sheets after the target.

The CR39 sheets exposed to the 158 A GeV lead beam were etched for 268 h

in a 6 N NaOH solution at 45 ^{o}C. Three CR-39 sheets from the stack with the Cu target were etched for 72h in 4N KOH water solution at 45^{o} C. For the Iron and Silicon exposures, the CR39 NTDs were etched for 30 h in 6N NaOH at 70 ^{o}C.

The base area of the etch-pit cones, their eccentricity and central brightness were measured with the ELBEK automatic image analyzer system, which also provides the absolute coordinates of the etched tracks; this allows the tracking of the beam ions and their fragments through the CR39 detectors [12]. Fig. 6.4 shows the average track area distribution of 158 A GeV Pb ions and their fragments after interacting in 1 cm thick Al target. The average is made on 8 to 12 faces (6 front and 6 back faces) of CR39 sheets.

Table 6.1 Atomic mass A_T, atomic number Z_T, density ρ_T, thickness of the target t, thickness of the CR39 before and after the target [$t_{(CR39)b}$ and $t_{(CR39)a}$]. The uncertainties on the thickness are ≥10 μm.

Target	A_T	Z_T	ρ_T (gcm^{-3})	t (cm)	$t_{(CR39)b}$ (cm)	$t_{(CR39)a}$ (cm)
H	1	1	-	-	-	-
CH_2	4.7	2.7	0.952 ± 0.002	1.02	0.73	1.35
CR39	7.4	4.0	1.320 ± 0.003	3.07		
C	12	6	1.733 ± 0.004	1.01	0.69	1.48
Al	27	13	2.692 ± 0.002	1.04	0.72	1.50
Cu	63.5	29	8.901 ± 0.002	0.99	0.72	1.51
Pb	207	82	11.331 ± 0.003	0.98	0.72	1.53

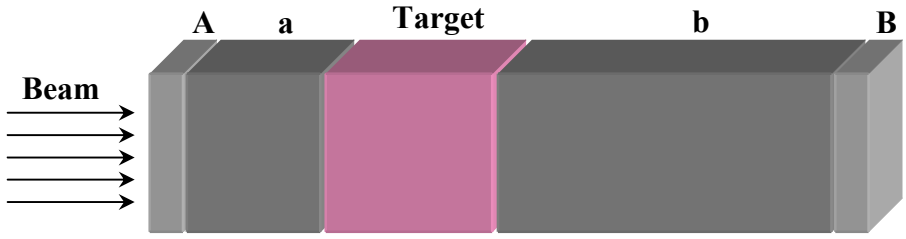

Fig. 6.2 Sketch of a stack showing the target-detector configurations used for the exposures to the relativistic Pb beam at CERN. 'A', 'a' and 'B', 'b' are different sections of the stack.

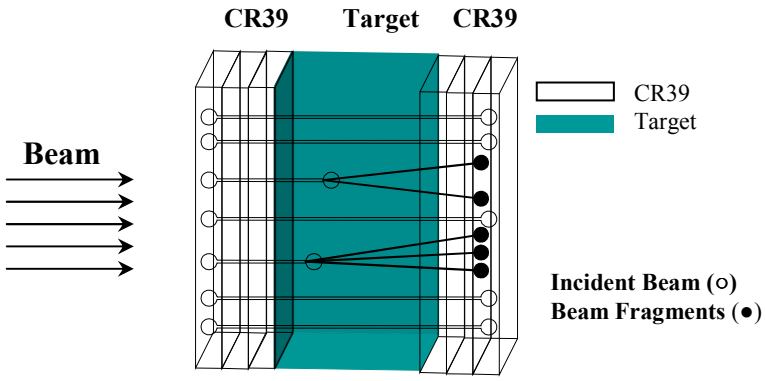

Fig. 6.3 *Sketch of a stack showing the target-detector configuration used for the exposures to relativistic Fe and Si ions at HIMAC, Chiba, Japan.*

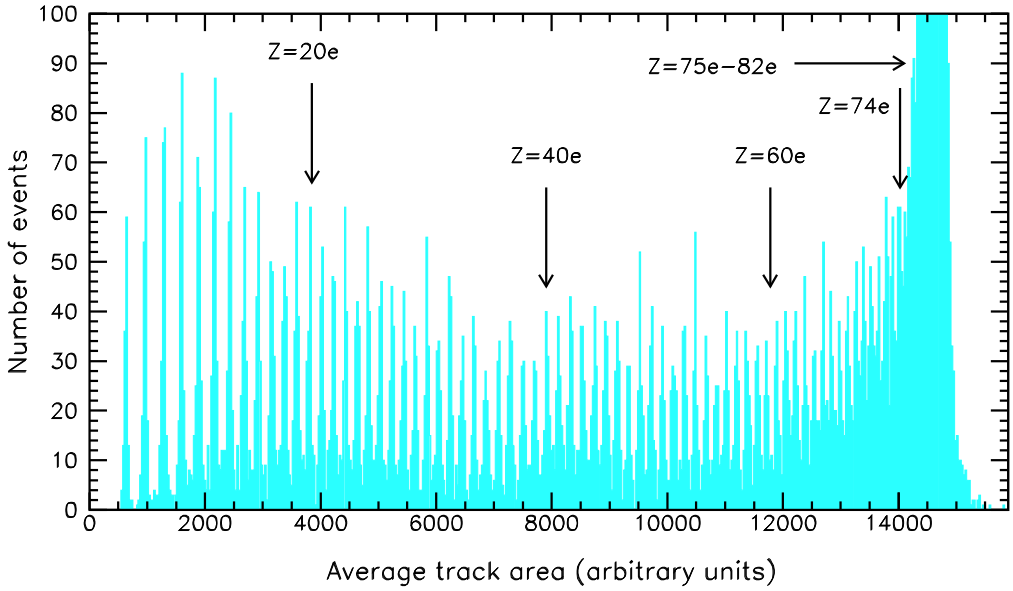

Fig. 6.4 *The average cone base area distribution on 8 faces out of 12 measured of CR39 NTDs after the Al target for 158 A GeV lead ions and their fragments.*

For the reconstruction of the path of projectiles and fragments, a tracking procedure was applied; the average track area was computed for each reconstructed ion path by requiring the existence of signals in eight out of twelve faces for the Pb ion beams and at least two out of three faces for the Fe, Si and C beams. Well separated charge peaks can be seen up to $Z = 74e$ in the case of the lead exposure (Fig. 6.4). The charge resolution obtained on a single face is about 0.19e.

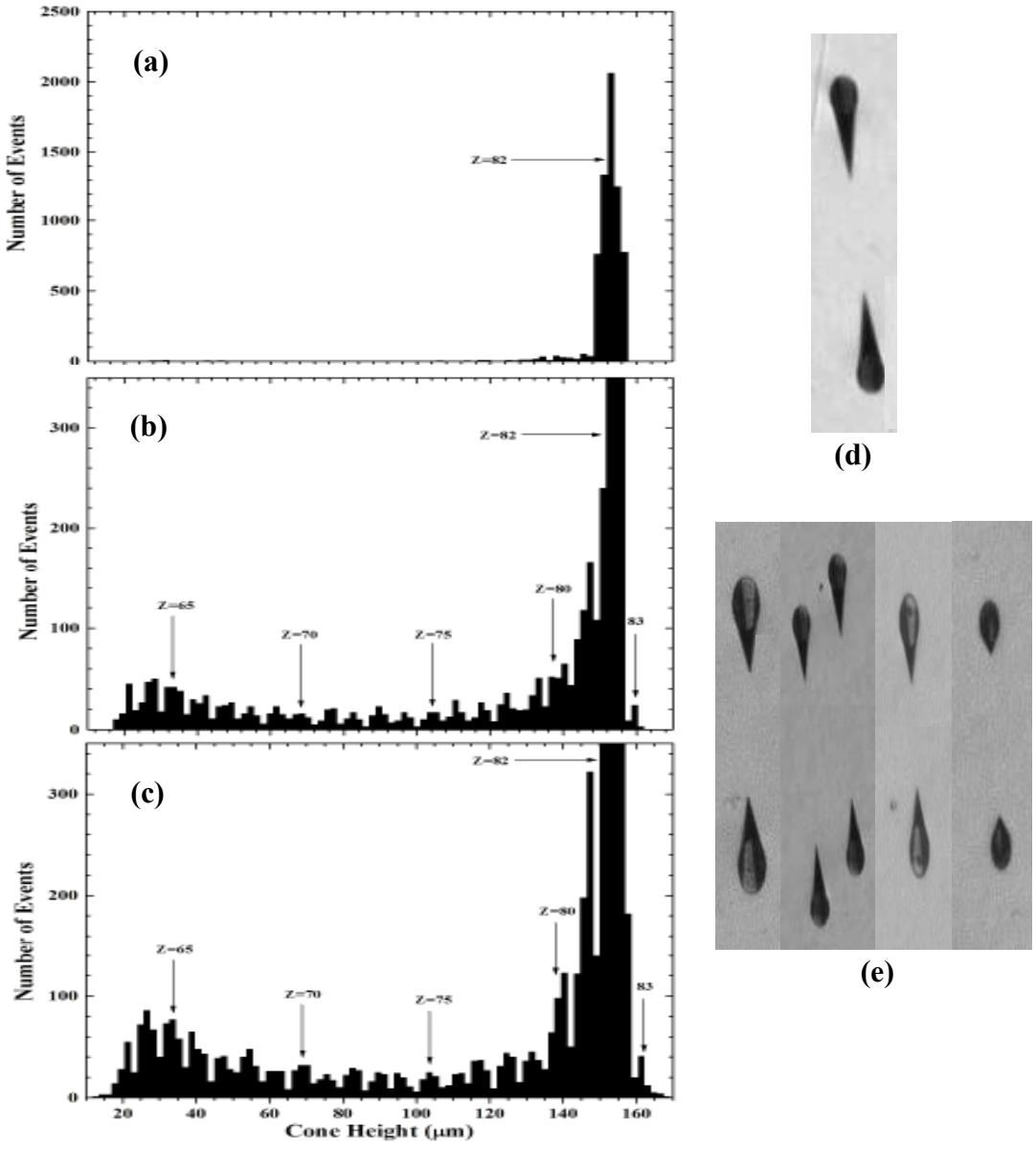

Fig. 6.5 Cone height distribution (a) of Pb beam ions before the target, (b) lead ions and their fragments detected immediately after the thick copper target and (c) the survived beam ions and the fragments produced in the Cu and CR39 targets located in the last part of the stack. (d) Microphotographs of Pb ion tracks in CR39 before the target and (e) tracks of survived Pb ions and beam fragments after the target. The microphotographs were taken by placing the detector at an angle of about 40^o with respect to the microscope objective.

For better separation of high Z fragments we used the cone height measurement technique, as explained in the calibration sections in chapter 4. The cone heights of tracks in three CR-39 foils (one before and two after the Cu target) were measured manually with an optical microscope (approximately 6300 etched cones were measured in each foil). It was observed that the cone length increases with increasing ion charges (see Fig. 4.22). Thus the measurements of the charge changing nuclear fragmentation cross section can be made from a change in cone lengths. The etched cone lengths were measured with an optical microscope with a magnification of 40x. The single measurements yield a resolution of $\sigma_L \simeq 2.5$ μm (σ_Z ~0.18e) at Z = 82, see Fig. 6.5a.

In Fig. 6.5b,c at Z = 83 there is a peak which corresponds to a charge pick-up reaction. The peaks with Z = 63 - 81 are due to the fragments produced in the interaction of Pb ions with the copper target.

The cross sections of lead ions in CR39 ($C_{12}H_{18}O_7$) were measured via the 'a, b' sections in Fig. 6.2 using eqs. 6.3 and 6.4; the cross sections on other simple targets were computed using eq. 6.5.

$$N_a = N_A e^{-\rho_{CR39} t_{CR39(a)} N_{av} \sigma_{CR39} / A_{CR39}} \tag{6.3}$$

$$N_b = N_B e^{\rho_{CR39} t_{CR39(b)} N_{av} \sigma_{CR39} / A_{CR39}} \tag{6.4}$$

N_A and N_B are the numbers of lead ions entering and leaving a stack; N_a and N_b are the numbers of lead ions immediately before and after a target; N_{av} is Avogadro's number; ρ_{CR39} and A_{CR39}, are the density and the average atomic mass number of the CR39 detector, $t_{\mathrm{CR39(A)}}$, $t_{\mathrm{CR39(B)}}$ are the thicknesses of CR39 in the A and B sections of the stack (see Fig 6.2 and Table 6.1).

The total charge changing cross sections were determined using the survival fraction of lead ions on different targets using the following relation:

$$\sigma_{(tot)} = \frac{A_T \ln(N_b/N_a)}{\rho\ t\ N_{av}} \tag{6.5}$$

The charge changing cross section on Hydrogen target was computed from the measured total cross sections on the CH_2 and C targets using the relation

$$\sigma_H = 0.5(3\sigma_{CH_2} - \sigma_C) \tag{6.6}$$

σ_{CH_2} is the average nuclear cross section in the CH_2 molecule, averaged over the number of atoms in each molecule. The systematic uncertainties are estimated to be smaller than 5%; their main contributions are due to two different experimental measurements (the average base area and the average cone height measurements) and to the uncertainties on densities and thicknesses of the materials. The statistical uncertainties on σ_{tot} are estimated via the following eqs. 6.5a

$$\delta\sigma_{(tot)} = \frac{\delta S}{x\ S} \tag{6.5a}$$

where $x = A_T/\rho\ t\ N_{av}$ and $S = N_b/N_a$.

The uncertainties for the Hydrogen target are calculated as

$$\delta\sigma_H = \sqrt{\left(\frac{3}{2}\delta\sigma_{CH_2}\right)^2 + \left(\frac{1}{2}\delta\sigma_C\right)^2} \tag{6.6a}$$

The measured total charge changing cross sections inclusive of nuclear and electromagnetic effects in ‘‘simple’’ and ‘‘composite’’ targets are given in the 3rd column of Table 6.2 and graphically shown in Fig. 6.6; data of Au ions on various targets [101-103].

We recall that, the measured total charge changing fragmentation cross sections, are due to the removal of at least one proton from the incoming beam ion [100].

Table 6.2 The measured total charge changing cross sections (using eq. 6.5) and σ_{nucl} and σ_{EMD} computed using the result of the fit to eq. 6.7 for Pb ions on different targets. The cross sections on CR39 and CH_2 are averaged over the number of atoms in each molecule. The quoted uncertainties are statistical only.

Target	A_T	$\sigma_{tot(exp.)}$ (mb)	σ_{nucl} (mb)	σ_{EMD} (mb)
H	1.0	1944 ± 256	*1909*	2
CH_2	4.7	2266 ± 156	*2366*	10
CR39	7.4	2642 ± 81	*2825*	22
C	12.0	2910 ± 210	*2565*	47
Al	27.0	3804 ± 164	*3406*	205
Cu	63.5	5089 ± 274	*4315*	943
Pb	207	12847 ± 638	*6357*	6794

Fig. 6.6 shows the total charge changing cross sections of 158 A GeV lead ions vs target mass A_T. Our results are almost independent of energy. For a target mass A_T = 207 the cross section is ~1.8 times larger than the corresponding value for 10 *A* GeV Au beam; the difference is probably due to the increase of the electromagnetic contribution with energy.

The total charge changing cross section has two components, σ_{nucl}, and σ_{EMD} The nuclear spallation σ_{nucl} is given by the Bradt-Peters eq. 6.1. The total cross section including electromagnetic dissociation can be expressed as

$$\sigma_{tot} = \sigma_{nucl} + \sigma_{EMD} = \pi r_o^2 (A_T^{1/3} + A_P^{1/3} - b_o)^2 + \alpha Z_T^{\delta} \qquad 6.7)$$

where A_P and A_T are the atomic masses of projectile and target, Z_T is the atomic number of the target. Our total charge changing cross section data shown in Fig. 6.6, together with the data from ref. [101-103] have been fitted to eq. 6.7. The result with the free parameter r_o, b_o, α and δ. The fit has χ^2 /D.o.F. = 0.7 of the fit is the solid line in Fig. 6.6. The values of the fitted parameters are r_o = 1.31 ± 0.02 fm, b_o = (0.96 ± 0.03), α = (1.57 ± 0.17) mb and δ = 1.9.

Fig. 6.7 shows the average base area distribution in CR39 for Fe and Si ion beams and their fragments after the CH_2 target. The numbers of events in the incident peak and in the peak after the target are used for the determination of the total charge changing cross sections in CH_2 using relation 6.5.

For the Fe and Si ions the fragmentation cross section is calculated via eq. 6.1 [104]; using the parameters $r_o = 1.35 \pm 0.02$ fm and $b_o = 0.83 \pm 0.12$ obtained in ref. [104], with fits for nuclei with $Z \leq 26$.

Table 6.3a,b,c gives the results of a series of measurements using the setup shown in Fig. 6.3.

Table 6.4 and 6.5 give the comparison of our measured cross sections with the data of Webber et al [105] for Fe and Si beam ions at different energies. The results are in good agreement within the quoted errors.

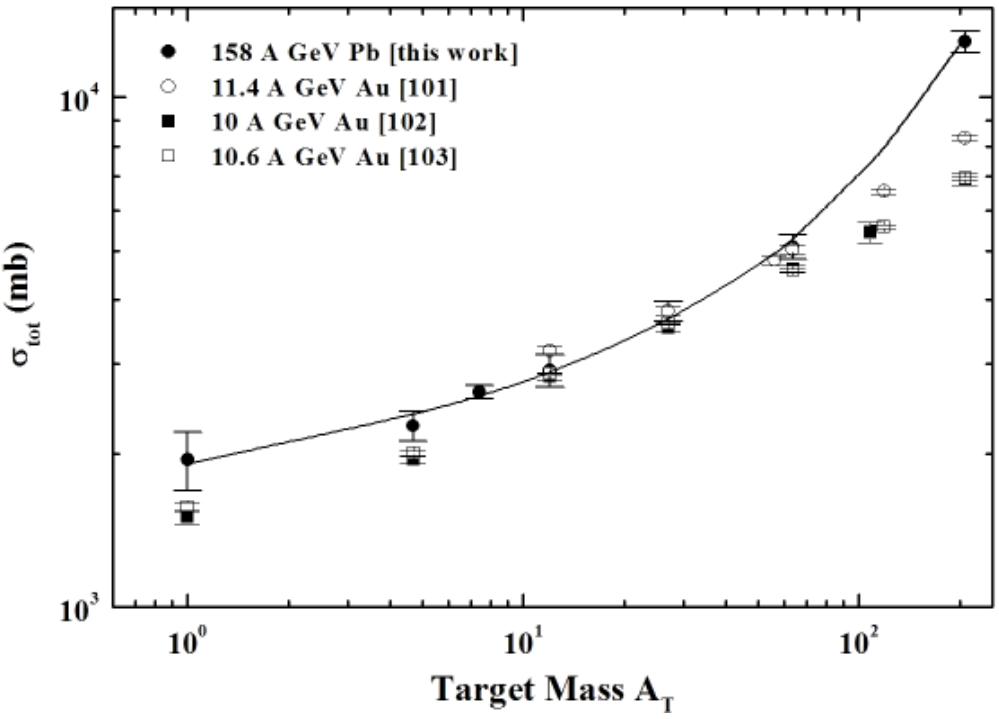

Fig. 6.6 Measured fragmentation charge-changing cross sections of 158 A GeV Pb ions versus targets mass number; the solid line is the fit of the measured data to eq. 6.7. The lower energy data from [101-103] are also shown.

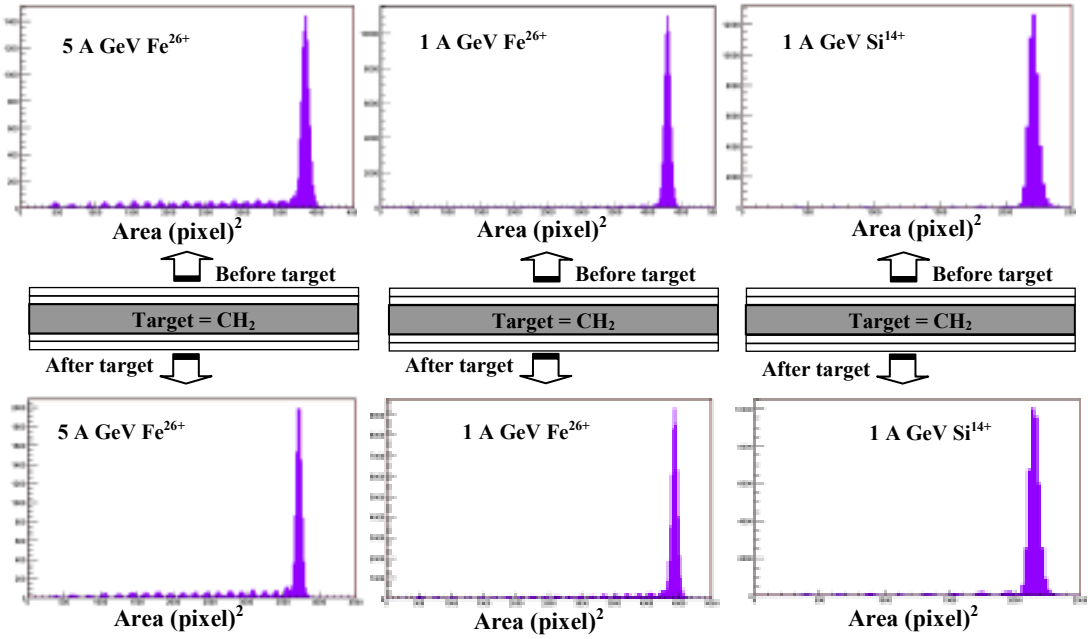

Fig. 6.7 *Average base area distributions of Fe^{26+} and Si^{14+} ions and fragments in CR39. The average is made on two front sheets of CR39 before and after the CH_2 target.*

Table 6.3a The measured total charge changing cross sections (eq. 6.5) with statistical standard deviations (eq. 6.5a) and the computed σ_{nucl} using eq. 6.1 for Fe^{26+} on different targets.

Energy (A GeV)	Target	A_T	(N_b/N_a)	$\sigma_{tot(exp.)}$ (mb)
10	**CH_2**	4.7	1.166	1147 ± 97
10	**CR39**	7.4	1.029	1105 ± 366
5	**CH_2**	4.7	1.137	1041 ± 130
5	**CR39**	7.4	1.028	1170 ± 478
3	**CH_2**	4.7	1.180	904 ± 140
3	**CR39**	7.4	1.071	1166 ± 67
1	**CH_2**	4.7	1.160	1105 ± 60
1	**CR39**	7.4	1.029	1113 ± 176
1	**Al**	27	1.120	1870 ± 131
0.41	**CH_2**	4.7	1.162	948 ± 54
0.41	**CR39**	7.4	1.033	1285 ± 245
0.30	**CH_2**	4.7	1.124	949 ± 61
0.30	**CR39**	7.4	1.033	1174 ± 192

Target	σ_{nucl} (mb)
CH_2	*1246*
CR39	*1396*
Al	*2053*

Table 6.3b The measured total charge changing cross sections and the computed σ_{nucl} using eq. 6.1 for Si^{14+} ions on different targets.

Energy (A GeV)	Target	A_T	(N_b/N_a)	$\sigma_{tot(exp.)}$ (mb)
5	**CH_2**	4.7	1.149	757 ± 168
5	**CR39**	7.4	1.018	807
3	***CR39***	7.4	1.025	754
3	***Al***	27	1.153	1533 ± 82
1	**H**	1.0	-	483 ± 76
1	**CH_2**	4.7	1.089	694 ± 46
1	**CR39**	7.4	1.020	834
1	**C**	12	1.103	1117 ± 62
1	**Al**	27	1.088	1397 ± 138

Target	σ_{nucl} (mb)
H	*588*
CH_2	*861*
CR39	*986*
C	*1155*
Al	*1548*

Table 6.3c The measured total charge changing cross sections and the computed σ_{nucl} using eq. 6.1 for 290 A MeV C^{6+} ions on different targets.

Target	A_T	(N_b/N_a)	$\sigma_{tot(exp.)}$ (mb)
CH_2	4.7	1.058	460 ± 53
CH_2	4.7	1.065	513 ± 52
Al	27	1.072	1155 ± 108

Target	σ_{nucl} (mb)
CH_2	*562*
Al	1136

Table 6.4 Measured total charge changing cross sections for Fe^{26+} ions of different energies on CH_2 targets. For comparison the results of Webber et al. are also given.

W.R. Webber et al. [105]	
Energy (A MeV)	**$\sigma_{tot(exp.)}$ (mb)**
400	2846
600	2958
810	2958
1180	2962
1600	3016

This work	
Energy (A MeV)	**$\sigma_{tot(exp.)}$ (mb)**
300	2847
410	2843
1000	3316
5000	3122
10000	3439

Table 6.5 Measured total charge changing cross sections for Si^{14+} ions of different energies on CH_2, C and H targets. For comparison the results of Webber et al are also given.

W.R. Webber et al. [105]			
Energy (A MeV)	$\sigma_{tot(exp.)}$**(mb)**		
	CH_2	***C***	H
570	1933	1176	379
830	1956	1183	387
1350	2027	1215	407
770 [107]	1980	1215	385
1296 [107]	2037	1229	403
1450 [108]	1961	1185	388

This work			
Energy (A MeV)	$\sigma_{tot(exp.)}$**(mb)**		
	CH_2	***C***	H
1000	2083	1127	478
5000	2272	-	-

Table 6.6 Measured total charge changing cross sections for C^{6+} ions of different energies on CH_2 and Al targets (measurements from ref. 105-107 and our results).

Energy (A MeV)	$\sigma_{tot(exp.)}$**(mb)**	
	CH_2	***Al***
267 [106]	1075	1215
498 [106]	1135	1103
296 [105]	974	-
326 [105]	988	-
310 [107]	1030	-

This work		
Energy (A MeV)	$\sigma_{tot(exp.)}$**(mb)**	
	CH_2	***Al***
290	1194	1144

6.3 Partial Charge Changing Cross Sections

If the thickness of the target is small compared to the mean free path of the fragments in that material, the fragmentation cross sections can be calculated using the simple relation [18].

$$\sigma(Z_i, Z_f) \approx \frac{1}{Kt}\frac{N_f}{N_i} \tag{6.8}$$

$\sigma(Z_i, Z_f)$ is the partial fragmentation cross section of a relativistic ion Z_i into the fragment Z_f, K is the number of target nuclei per cm^3, t is the thickness of the target, N_i is the number of primary ions and N_f is the number of fragments produced with charge Z_f. This expression may be valid also for a thick target, (assuming that the number of fragments before the target is zero):

From the data shown in Fig. 6.4 we may obtain the partial fragmentation cross section, using the number of events on each peak for N_f = 7 to 74 and the number of survived lead ions N_i after the target for incident 158 A GeV lead ions. For 75≤ Z ≤ 82 we measured the cone heights in one face of a CR39 sheet (see Fig. 6.5) before and after each target. Both N_f and N_i are corrected for the CR39 detector thickness before the target using eq. 6.3 and 6.4.

For the Fe and Silicon beam ions exposures, we observed that fragments are present even before the target (Fig. 6.7). In this case the partial charge change cross sections have been calculated via the relation [106]

$$\sigma_{\Delta Z} = \frac{1}{Kt}\left(\frac{Z_{out}^{f}}{Z_{s}^{p}} - \frac{Z_{in}^{f}}{Z_{in}^{p}}\right) \tag{6.9}$$

where Z_{in}^{f} and Z_{out}^{f} are the number of projectile fragments of each charge before and after the target and Z_{in}^{p} and Z_{s}^{p} are the number of incident and survived projectile ions, respectively.

The partial charge changing cross sections for 158 A GeV lead ions with seven different targets are shown in Fig. 6.8. The fragmentation cross sections for hydrogen material are calculated using eq. 6.6. The overall statistical and systematical uncertainties are about 10 - 20% (the errors from multifragmentation inside the thick target and the CR39 material, charge identification, tracking procedure are not considered).

The highest cross section is at ΔZ = -1 (Z = 81) the value decreases for ΔZ ~ -11 (Z ~71) and then a rise is noticed. The same behavior is observed in the low charge change region (Z ~7 to 30); the values decreases and then remains in the plateau region, no change in the cross section value up to Z = 60.

Table 6.7 Partial charge changing cross sections for 1.0 A GeV Fe^{26+} on CH_2 target. For comparison the results of Webber et al and Zeitlin et al are also given.

ΔZ	This Work $\sigma_{\Delta Z}$ *(mb) 1.0 A GeV*	[105] $\sigma_{\Delta Z}$ *(mb) 1.09 A GeV*	[109] $\sigma_{\Delta Z}$ *(mb) 1.05 A GeV*
-1	-	378 ± 7	374 ± 12
-2	338 ± 11	287 ± 5	299 ± 10
-3	285 ± 11	211 ± 7	220 ± 8
-4	252 ± 10	217 ± 7	225 ± 8
-5	249 ± 10	159 ± 5	170 ± 6
-6	197 ± 9	161 ± 5	164 ± 6
-7	168± 8	112 ± 7	125 ± 5
-8	132 ± 7	109 ± 7	121 ± 5
-9	175 ± 8	80 ± 5	97 ± 4
-10	107 ± 7	95 ± 6	98 ± 4
-11	152 ± 6	59 ± 7	74 ± 3
-12	105 ± 8	83 ± 9	92 ± 4
-13	103 ± 6	53 ± 6	70 ± 3
-14	81 ± 6		
-15	80 ± 6		
-16	50 ± 4		
-17	76 ± 5		
-18	86 ± 6		
-19	127 ± 7		
-20	26± 3		

We observed a significant rise in the cross section in the middle charge change region for the three targets Al, Cu and Pb (see also Fig. 6.3; a rise in the total

number of counts starts at Z = 38); this may be due to contribution of electromagnetic dissociation, see the σ_{EMD} values in Table 6.2. Binary fission may be one of possible explanations of this effect as observed at the mid charge change of the Pb incident ions. The EMD contribution for light targets is not observed (its value is within our systematic and statistical uncertainties, see Table 6.2).

The measured partial charge changing cross sections for Fe and Si beam ions with CH_2 are shown in Tables 6.7 and 6.8. For comparison the results of Webber et al and Zeitlin et al are also given for the same Fe beam energy region [105, 109]. We observed the same behavior for the partial cross sections; the maximum cross section is at $\Delta Z = -1$. Our results and those of Webber et al and Zeitlin et al at ~1 A GeV Fe ions have the same trend, a high value at one charge change and then the cross section decreases as the charge of the fragment decreases. We observed a 2nd high cross section at $\Delta Z = -11$; other authors observed the same effect at $\Delta Z = -10$. We observe a third high value at $\Delta Z = -19$. For the 1 A GeV Si^{14+} ions we observe the same trend: maximum cross section at $\Delta Z = -1$, then a decrease and a 2nd high value at $\Delta Z = -6$.

Table 6.8 Partial charge changing cross sections for 1.0 A GeV Si^{14+} ions on CH_2 target.

ΔZ	$\sigma_{\Delta Z}$ (mb)
-1	293 ± 18
-2	177 ± 12
-3	123 ± 11
-4	122 ± 11
-5	62 ± 8
-6	117 ± 11
-7	83 ± 9
-8	90 ± 10

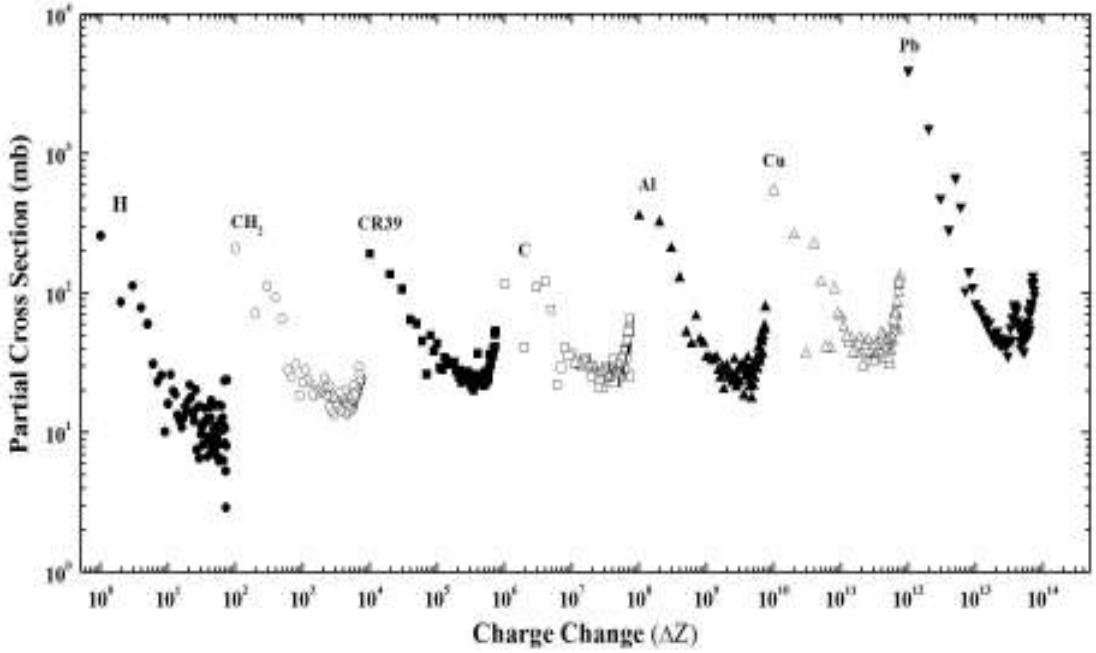

Fig. 6.8 Partial charge changing cross sections for 158 A GeV lead ions on targets from H to Pb; Charge states are between ΔZ = -1 to 75. For better visibility are multiplied the charge change by a factor of 100: 10^0-10^2 for H; 10^2-10^4 CH_2; 10^4-10^6 CR39; 10^6-10^8 C; 10^8-10^{10} Al; 10^{10}-10^{12} Cu; 10^{12}-10^{14} Pb.

7. Conclusions

The surface quality of the CR39 and Makrofol Nuclear Track Detectors were improved by new etching conditions as compared to previous standard etching conditions; the new methods remove background and enhance the sharpness of the tracks. A high sensitivity was achieved by the improved etching and measuring methods for CR39 compared to previous standard one. The polycarbonate Makrofol NTD was calibrated for the first time over a large energy loss range: a detection threshold of $Z \sim 50$ was achieved for relativistic charged particles.

The addition of small fractions of ethyl alcohol in the etching solutions is very useful in experiments having a significant background originated by local sources of charged particles (e.g. the high altitude large area detectors like SLIM) and in the case of cosmic ray long duration balloon and space experiments, where the presence of many low energy particles may endanger the study of cosmic abundances of primary ions.

New calibrations for CR39 and Makrofol NTDs were performed with In^{49+}, Pb^{82+}, Fe^{26+} and Si^{14+} relativistic ions making use of new etching methods. Calibration curves of p vs REL were obtained for wide ranges of charge and energy.

A search for Intermediate Mass Magnetic Monopoles and Strange Quark Matter was performed with 400 m^2 of CR39 NTDs, with an average exposure time of 4 years, (SLIM experiment). The exposed NTDs were analyzed using the new strong etching and improved measuring methods. No survival candidate was found; the present 90% CL upper flux limits for downgoing IMMs is 1.55×10^{-15} $cm^{-2}s^{-1}sr^{-1}$ (Fig. 5.11). Similar upper limits are also valid for downgoing nuclearites and Q-balls of any speed. A detailed discussion was made on a strange non reproducible candidate.

A study of the total and partial charge changing cross sections of relativistic lead, iron, silicon and carbon ions on different targets was performed. It was observed that the

total charge changing cross sections increase with target mass and energy; the highest values are observed for Cu and Pb targets and this is mainly due to electromagnetic dissociation (see Fig. 6.6). It was also observed that the total charge changing cross section is energy independent for light target materials as CH_2 and CR39. A high partial charge changing cross section for lead, iron and silicon ions was observed for $\Delta Z \sim 1$; the value decreases as the charge change ΔZ increases.

The measured cross section data indicate that passive NTDs, especially CR39, can be used effectively for studies of the total and partial charge changing cross sections, also in comparison with active detectors.

References

1. D. A. Young, Nature 182 (1958) 375.
2. E. C. H. Silk and R. S. Barnes, Phil. Mag. 4 (1959) 970.
3. R. L. Fleischer et al., Nuclear Tracks in Solids: Principles and Applications, University of California Press, Berkeley (1975).
4. R. L. Fleischer et al., Ann. Rev. Nucl. Sci. 15 (1965a) 1.
5. P. B. Price et al., Proc. 11th Int. Conf. on Cosmic Rays, Budapest (1970) 417.
6. G. Siegman et al., Proc. 9th Int. Conf. Solid State Nuclear Track Detectors, Suppl. 1 Nucl.Tracks (1976) 1059.
7. S. Cecchini., et al., Il Nuovo Cimento 109A (1996) 1119.
8. S. Manzoor et al., Nucl. Instrum. Meth. A453 (2000) 525.
9. B. G. Cartwright et al., Nucl. Instrum. Meth. 153 (1978) 457.
10. G. Tarle, Proc. 17th Int. Cosmic Rays Conf., Paris 8 (1981) 174.
11. P. B. Price and D. O'Sullivan, Proc. 11th Int. Conf. on Solid State Nuclear Track Detectors, Bristol (1981) 929.
12. G. Giacomelli et al., Nucl. Instrum. Meth. A411 (1998) 41.
13. E. V. Benton and W. G. Nix, Nucl. Instrum. Meth. 67 (1969) 343.
14. D. Sampsonidis et al., Phys. Rev. C51D (1995) 3304.
15. C. Brechtmann and W. Heinrich, Z. Phys. A330 (1988) 407.
16. C. Lewenkopf et al., Phys. Rev. C44 (1991) 1065.
17. S. E. Hirzebruch et al., Nucl. Instrum. Meth. B74 (1993) 519.
18. H. Dekhissi et al., Nucl. Phys. A662 (2000).
19. R. Brandt, Nucl. Instrum. Meth. 173 (1980) 111.
20. B. Grabez et al., Nucl. Instrum. Meth. 211 (1983) 209.
21. H. Khan et al., Kerntechnik 49 (1987) 209.
22. H. A. Khan et al., Phys. Rev. C28 (1983) 1630.
23. H. A. Khan, N. A. Khan and R. J. Peterson, Phys. Rev. C35 (1987) 645.
24. I. E. Qureshi et al., Nucl. Phys. A477 (1988) 510.

25. H. Drechsel et al., Nucl. Instrum. Meth. 227 (1984) 342.
26. A. Noll et al., Nucl. Tracks Radiat. Meas. 15 (1988) 265.
27. W. Heinrich et al., Nucl. Tracks Radiat. Meas. 15 (1988) 393.
28. S. Cecchini et al., Astropart. Phys.1 (1993) 369.
29. S. Cecchini et al., Il Nuovo Cimento 24C (2001) 639.
30. T. Chiarusi et al., Rad. Meas. 36 (2003) 335.
31. B. A. Weaver et al., Nucl. Instrum. Meth. B145 (1998) 409.
32. B. A. Weaver and A. J. Westphal, Nucl. Instrum. Meth. B187 (2002) 285.
33. B. A. Weaver and A. J. Westphal, Nucl. Instrum. Meth. B207 (2003) 322.
34. M.R. Shavers et al., Advances in Space Research 34 (2004) 1333.
35. Y. Koike et al., Acta Astronautica 56 (2005) 367.
36. M. Casolino et al., Advances in Space Research 37 (2006) 1685.
37. T. Nakamura and L. Heilbronn, Nucl. Instrum. Meth. A562 (2006) 706.
38. M. Durante and A. Kronenberg, Advances in Space Research 35 (2006) 180.
39. A. Denker et al., Nucl. Instrum. Meth. B240 (2005) 61.
40. U. Amaldi and G. Kraft, Rep. Prog. Phys. 68 (2005) 1861.
41. G. Somogyi, Nucl. Track Detection 1 (1977) 3.
42. G. Somogyi G. and I. Hunyadi, Proc. 10th Int. Conf. Solid State Nuclear Track Detectors, Suppl. 2 (1980) 443.
43. G. Somogyi, Proc. 11th Int. Conf. Solid State Nuclear Track Detectors (1981) 101.
44. S.A. Durrani and R.K. Bull, Solid State Nuclear Track Detection, Pergamon Press, Oxford, (1987).
45. B. E. Fischer and R. Sphor, Rev. of Modern Phys. 55 (1983) 907
46. R.L Fleischer et al., Phys. Rev. 133 (1964) 1443.
47. R.L. Fischer et al., Phys. Rev.156 (1967) 353.
48. W. Enge et al., Nucl. Instrum. Meth. 127 (1975) 125.
49. H. A. Khan, Nucl. Instrum. Meth. 109 (1973) 515.
50. H. A. Khan and S. A. Durrani, Nucl. Instrum. Meth. 101 (1972) 583.
51. B. Dorschel et al., Radiat. Protection Dosimetry 82 (1999) 85.

52. P. A. M. Dirac, Proc. Roy. Soc. Lond. 281B (1931) 60.
53. G. ’t Hooft, Nucl. Phys. B29 (1974) 276.
M. Polyakov, JETP Lett. 20(1974|) 194.
N. S. Craigie et al., Theory and Detection of MMs in Gauge Theories, World Scientific, Singapore (1986).
54. G. Giacomelli, Lectures at the Lake Louise Workshop (1994).
55. G. Giacomelli et al., hep-ex/011209; hep-ex/0302011; hep-ex/0211035; hep-ex/0506014.
56. M. Bertani et al., Europhys. Lett. 12 (1990) 613.
57. G. Giacomelli, L.Patrizii, Lecture at the Summer School on Astroparticle Physics and Cosmology ICTP, Trieste(2002), hep-ex/0302011.
58. G. Giacomelli, Riv. Nuovo Cimento, 7N12 (1984) 1.
59. J. Derkaoui et al., Astropart. Phys. 9 (1998) 173; Astrop. Phys. 9 (1999) 339.
60. M. Ambrosio et al., Eur. Phys. J. C25 (2002) 511; Phys. Lett. B406 (1997) 249; Phys. Rev. Lett. 72 (1994) 608.
61. (Ohya collab.) S. Orito et al., Phys. Rev. Lett. 66 (1991) 1951.
62. (Baksan collab.) E. N. Alexeyev et al., 21st ICRC, 10 (1990) 83; V. A. Balkanov et al., Proc. Of ICRC 2001; Prog. Part. Nucl. Phys. 40 (1998) 391.
63. (Baikal collab. And AMANDA collab.) V. Aynutdinov et al., astro-ph/0507713; Pro. Part. Nucl. Phys. 40 (1998) 391.
64. P. B Price, Phys. Rev. D38 (1988) 3813.
D. Ghosh and S. Chatterjee, Europhys. Lett. 12 (1990) 25.
65. T.W. Kephart and T.J. Weiler, Astropart. Phys. 4, 271 (1996).
66. T.J. Weiler and T.W. Kephart, Nucl. Phys. B (Proc. Suppl.) 51 B, 218 (1996)
67. S. Balestra et al., hep-ex/060236; hep/ex-0506075.
68. E. N. Parker, Astrophysics J. 122 (1955) 293; Astrophysics J. 160 (1970) 383.
69. F. C. Adams et al., Phys. Rev. Lett. 70 (1993) 2511.

70. S. P. Ahlen, Phys. Rev. Lett. 72 (1994) 608; M. Ambrosio et al., Astrop. Phys. 6 (1997) 113; Nucl. Instrum. Meth. A486 (2002) 663; Astrop. Phys. 4 (1995) 33; Astrop. Phys. 18 (2002) 27.
71. G. F. Drell et al., Nucl. Phys. B209 (1982) 45.
72. S. Cecchini et al., Il Nuovo Cimento A109 (1996) 1119.
S. Cecchini et al., Radiation Measurements 40 (2005) 405.
73. S. Manzoor et al., Radiation Measurements 40 (2005) 433.
74. S. P. Ahlen, Phys. Rev. D 17 (1978) 229.
75. S. P. Ahlen et al., Phys. Rev. D 26 (1982) 2347.
76. A. De Rujula, Nucl. Phys. B435 (1995) 257.
77. D. Bakari et al., hep-ex/0003028.
78. I. De Mitri, Ricerca di monopoli magnetici supermassivi nella radiazione cosmica, Ph.D. Thesis, University of L'Aquila (1996); P.F. Spada, Ricerca di monopoli magnetici co1 rivelatore MACRO, Ph.D. Thesis, University of Bologna (1996); R. Fantini, Ricerca di monopoli magnetici GUT con i tubi a streamer di MACRO, Ph.D. Thesis, University of Bologna (1997); T.W. Ruijgrok, J.A. Tjon, T. T. Wu, Phys. Lett. B 129 (1983) 209; S. Nakamura, Ph.D. Thesis, Search for supermassive relics by large area plastic track detectors, UT-ICEPP-88-04, University of Tokyo (1988).
79. E. Witten, Phys. Rev. D30 (1984) 272.
80. S. P. Ahlen, Phys. Rev. D 14 (1976) 2935.
81. S. Chin and R. Kerman, Phys. Rev. Lett. 43 (1979) 1292.
82. P. Haensel et al., Astro. Astrophys. 160 (1986) 121 ; P. Haensel et al. Astrophys. J. 310 (1986) 261.
83. E. Farhi and R. L. Jaffe, MIT Preprint CPT 1160 (1984); E. Farhi and R. L. Jaffe, Phys. Rev. D32 (1985) 2452.
84. A. DeRujùla and S. L. Glashow, Nature 312 (1984) 734.
85. T. Shibata, Prog.Theor.Phys. 57 (1977) 882.
86. D. Bakari et al., hep-ex/004019.
87. Ambrosio et al., MACRO Collaboration, Eur. Phys. J. C13 (2000) 453.

88. S. Balestra et al., Nucl. Instrum. Meth. B 254 (2007) 254, physics/0610227.
89. I. E. Qureshi et al., Radiat. Meas. 40 (2005) 437.
90. S. Balestra et al., Czech. J. Phys. 56 (2006) A221, hep-ex/0601019; S. Balestra et al., hep-ex/0602036.
91. S. Manzoor et al., Radiat. Meas. 40 (2-6) (2005) 433, hep-ex/0502034.
92. S. Manzoor et al., 10th Topical Seminar on Innovative Particle and Radiation Detectors, 1-5 October 2006, to be published in Nucl. Phys. A proc. Suppl., physics/0611084.
93. P. B. Price et al., Phys. Rev. Lett. 35 (1975) 487; Phys. Rev. D18 (1978) 1382;
B. Cabrera, Phys. Rev. Lett. 48 (1982) 1378.
V. V. Kopenkin et al., 28th ICRC, Tsukuba, Japan (2003) 1583.
94. C. Brechtmann and W. Heinrich, Phys. Rev. C39 (1989) 2222.
95. S. E. Hirzebruch et al., Phys. Rev. C46 (1992) 1487.
96. J. Westphal et al., Phys. Rev. C44 (1991) 1687.
97. S. E. Hirzebruch et al., Nucl. Instrum. Meth. B74 (1993) 519.
98. A. N. Golovchenko et al., Radiat. Meas. 34 (2001) 297.
99. L. Sihver et al., Phys. Rev. C 47 (1993) 1225.
100. G. D. Westfall et al., Phys. Rev. C19 (1979) 1309.
101. Y. He, P.B. Price, Z Phys. A 348 (1994) 105.
102. S. E. Hirzebruch et al., Phys. Rev. C51 (1995) 2085.
103. L. Y. Geer et al., Phys. Rev. C52 (1995) 334.
104. J. R. Cummings et al., Phys. Rev. 42 (1990) 2508.
105. W. R. Webber et al., Phys. Rev. C41 (1990) 520.
106. I. Schall et al., Nucl. Instrum. Meth. B117 (1996) 221.
107. W. R. Webber et al., ICRC proc. 3 (1985) 87.
108. A. N. Golovchenko et al., Phys. Rev. C66 (2002) 014609-1.
109. C. Zeitlin et al., Phys. Rev. C56 (1997) 388.

Figure Captions

Fig. 2.1 *A latent track is formed in (a) inorganic solids by the ionization and production of dense positive ions along the ion path and (b) the breakage of polymeric chains by the passage of charged particle.*

Fig. 2.2 *(a) Sketch of a NTD track and (b) etched α tracks in a CR39 detector.*

Fig. 2.3 *Track geometry at different dip angle conditions: (a) formation of the post etched cone for a particle with an incident angle $\theta > \theta_c$ ($v_T t > v_B t$), (b) limiting case when the incident angle $\theta = \theta_c$ ($v_T t \geq v_B t$) and (c) no track is detected if the incident angle $\theta < \theta_c$ ($v_T t \leq v_B t$).*

Fig. 2.4 *Track geometry for a charged particle impinging at normal incidence in a nuclear track detector.*

Fig. 2.5 *Geometry of a particle incident at an angle θ with respect to the detector surface.*

Fig. 3.1 *The energy losses, in MeV/cm, of $g = g_D$ MMs in liquid hydrogen vs β. Curve a) corresponds to elastic monopole–hydrogen atom scattering; curve b) to interactions with level crossings; curve c) describes the ionization energy loss.*

Fig. 3.2 *A massive GUT MM structure with different regions (for details see text).*

Fig. 3.3 *The experimental 90% C.L. upper flux limits for magnetic monopoles obtained with MACRO electronic and passive detectors; also the results obtained by other experiments, are shown.*

Fig. 3.4 *90% C.L. flux upper limits obtained with the MACRO CR39 nuclear track detector for MMs with different magnetic charges, $g = g_D$, $2g_D$, $3g_D$ and for M+p (dyon).*

Fig. 3.5 *The different regions of an Intermediate mass monopole.*

Fig. 3.6 *The downgoing MMs accessible mass regions in the plane (mass, β) for $g = g_D$ at an altitude of 20 km, for an experiment at 5230 m (SLIM) and for an underground experiment (MACRO).*

Fig. 6.8 *Partial charge changing cross sections for 158 A GeV lead ions on targets from H to Pb; Charge states are between ΔZ = -1 to 75. For better visibility are multiplied the charge change by a factor of 100: 10^0-10^2 for H; 10^2-10^4 CH_2; 10^4-10^6 CR39; 10^6-10^8 C; 10^8-10^{10} Al; 10^{10}-10^{12} Cu; 10^{12}-10^{14} Pb.*

Table Captions

Table 2.1 Etching conditions for some commonly used nuclear track detector.

Table 4.1. "Soft" etching conditions and bulk etch rates v_B for CR39 obtained with the standard method using 25 thickness measurements for each final data point. The errors are statistical standard deviations of the mean.

Table 4.2. "Strong" etching and bulk etch rates v_B for CR39 obtained with the standard methods using 9 measurements for each final data point. The errors are statistical standard deviations.

Table 4.3 Bulk etch rates v_B for CR39 and Makrofol NTDs obtained with the new and with the standard methods using 25 measurements for each data point. The errors are statistical standard deviations of the mean.

Table 4.4 Assigned charges and computed charge resolutions for In^{49+} and Pb^{82+} ions and their fragments in CR39 and Makrofol detectors. Charge resolution is estimated from eq. 4.6a but the last row was computed from eq. 4.6b.

Table 4.5 Mean base areas and charge resolutions σ_Z of nuclear fragment measured in CR39 NTDs using high energy Fe^{26+}, Si^{14+} and C^{6+} ion beams on a CH_2 target.

Table 6.1 Atomic mass A_T, atomic number Z_T, density ρ_T, thickness of the target t, thickness of the CR39 before and after the target [$t_{(CR39)b}$ and $t_{(CR39)a}$]. The uncertainties on the thickness are ≥10 μm.

Table 6.2 The measured total charge changing cross sections (using eq. 6.5) and σ_{nucl} and σ_{EMD} computed using the result of the fit to eq. 6.7 for Pb ions on different targets. The cross sections on CR39 and CH_2 are averaged over the number of atoms in each molecule. The quoted uncertainties are statistical only.

Table 6.3a The measured total charge changing cross sections (eq. 6.5) with statistical standard deviations (eq. 6.5a) and the computed σ_{nucl} using eq. 6.1 for Fe^{26+} on different targets.

ACKNOWLEDGEMENTS

This is perhaps the easiest and hardest chapter that I have to write. It will be simple to name all the people who helped me to get this work done, but it will be tough to thank them enough. I will nonetheless try…

It is difficult to overstate my gratitude to my Ph.D. supervisors, Prof. Giorgio Giacomelli, Dr. Imtinan E. Qureshi and Dr. Laura Patrizii. With their enthusiasm, inspiration, and great efforts to explain things clearly and simply the completion of this thesis would have not been possible. Throughout my thesis writing period, they provided encouragement, sound advice, good teaching, good company, and lots of good ideas.

From the formative stages of this thesis, to the final draft, I owe an immense debt of gratitude to my supervisor, Prof. Giorgio Giacomelli: his careful reading of my original manuscript and his detailed, perceptive comments contributed in many ways to the shape and clarity of the finished thesis.

I have also to thank Dr. Patrizii and Dr. Qureshi for guiding me through the writing of the thesis, and for all the corrections and revisions made to the text. It became a lighter and more concise thesis after their suggested improvements.

I must send thanks to all the SLIM team. Without their support and striving development the project would have never reached the great result it did. A special gratitude is due to Prof. Giacomelli for leading the group so far and being insatiable in the quest for improvement and knowledge. Giacomelli was also a particular good leader and motivator, enabling all the team to face the hard work with a smile on the lips. The discussions, encouragement and critiques made by all collaborators were of essence to the progress of this work.

And last but not the least Laura, not necessarily for coming along at the right time, but for the very special person she is. And for the incredible amount of patience she had with me in the last six months. It is time to start on that list of things to do.

I wish to thanks Dr. Vincent Togo and Dr. A. Kumar and Dr. M. Giorgini for many technical discussions on how to improve the thesis and for helping me get through the difficult times, and for all the emotional support, friendship, and kind-hearted they provided. Togo, Lina and Chantal, whose extreme generosity will be remembered always, I extend my deepest appreciation.

I am also grateful to the secretary Mrs. Anastasia Casoni for helping the Departments matters to run smoothly and for assisting me in many different ways.

I would also like to thank the INFN sezione di Bologna, the Physics Department of the University of Bologna and I am grateful to the Abdus Salam International Centre for Theoretical Physics, ICTP, Trieste; special thanks to Prof. G. Furlan for his kind support and help during the whole stay in Bologna. I also like to especially thank the efficient staff at ICTP, Mrs. M. Durrani, Mrs. E. Dose and Mrs B. Valassi for their care, attention and the rest for their continued moral support.

At the end, I would be offhand without mentioning my entire extended family; mother, wife and two sweet daughters, Sidra and Areeba, as they patiently allowed me to do this work.

Publications

1. V.Togo et al; The MACRO collaboration, “Calibration of CR39 and Makrofol nuclear track detectors and search for exotic particles” Nucl. Phys. B 125 Proc. Suppl. (2003) 217.
2. S. Cecchini et al; The SLIM collaboration: "Search for magnetic monopoles at a high altitude laboratory", *Proc. 28th Int.l Cosmic Ray Conf., Tsukuba, Japan, July 31 – August 7, 2003*, Universal Academy Press, Inc. (2003) 1657.
3. M. Ambrosio et al; The MACRO collaboration: “Moon and Sun shadowing effect in the MACRO detector” Astropart. Phys. 20 (2003) 145.
4. M. Ambrosio et al; The MACRO collaboration: “Measurements of atmospheric muon neutrino oscillations, global analysis of the data collected with MACRO detector” Eur. Phys. J C36 (2004) 323.
5. G. Battistoni et al; “Search for a Lorentz invariance violation contribution in atmospheric neutrino oscillations using MACRO data” Phys. Lett. B 615 (2005) 14.
6. Y. Becherini et al; “Time correlations of high energy muons in an underground detector” Astropart. Phys. 23 (2005) 341.
7. S. Cecchini, et al; “Search for intermediate mass magnetic monopoles and nuclearites with the SLIM experiment”, *Radiation Measurements* 40 (2005) 405.
8. S. Cecchini, et al; “Application of nuclear track detectors in astroparticle and nuclear physics” 9th ICATPP Conf. on Astroparticle, Particle, Space Physics, Detectors and Medical Physics Applications, Villa Erba, Como, Italy, 17-21 Oct 2005, Astroparticle, particle and space physics, detectors and medical physics applications Url-str (9) (2005) 149.

9. S. Cecchini, et al; “Cosmic ray abundance measurements with the CAKE balloon experiment” Proc. 29th Inter. Cosmic Ray Conf., Pune 3 (2005) 5, astro-ph/0510717.
10. S. Manzoor et al; “Calibration of Makrofol-De nuclear track detector using relativistic lead ions” *Radiation Measurements* 40 (2005) 433.
11. I.E. Qureshi et al; “Study of projectile fragmentation in the reaction (158 A GeV) Pb + Pb using CR-39”, *Radiation Measurements* 40 (2005) 437.
12. T. Chiarusi; “The CAKE experiment Progress and new results” *Radiation Measurements* 40 (2005) 424.
13. S. Balestra et al; “Rare particle searches with the high altitude SLIM experiment”**,** EPS Int. Europhysics Conf. on H. E. P., Lisbon, Portugal, 21-27 Jul 2005. PoS HEP (2006) 018, hep-ex/0602036.
14. S. Balestra; “Search for massive rare particles with SLIM experiment” Proc. 29th Inter. Cosmic Ray Conf., Pune 9 (2005) 223.
15. S. Balestra et al., “Search for SQM in cosmic rays at high altitude laboratories”, J. Phys. Conf. Ser. 39 (2006) 194.
16. L. Arrabito et al., “Hardware performance of a scanning system for high speed analysis of nuclear emulsions”, Nucl. Instrum. Meth. A 568 (2006) 578, physics/0604043.
17. S. Balestra et al., “Search for nuclearites with the SLIM detector**”,** Inter. Conf. on Interconnection between H. E. P. and Astroparticle Physics: From Colliders to Cosmic Rays, Prague, Czech Republic, 7-13 Sep 2005, Czech. J. Phys. 56 (2006) A221, hep-ex/0506075.
18. S. Balestra et al., “Bulk etch rate measurements and calibrations of plastic nuclear track detectors” Nucl. Instrum. Meth. B 254 (2007) 254, physics/0610227.
19. S. Manzoor et al., “Nuclear Track Detectors for Particle Searches”, 10th Topical Seminar on Innovative Particle and Radiation Detectors, 1-5 October 2006, to be published in Nucl. Phys. A proc. Suppl., physics/0611084.

20. S. Manzoor et al., “Nuclear Track Detectors for Environmental Studies and Radiation Monitoring” 10th Topical Seminar on Innovative Particle and Radiation Detectors, 1-5 October 2006, to be published in Nucl. Phys. A proc. Suppl., physics/0611278.
21. V. Togo et al., “Fragmentation studies of high energy ions using CR39 nuclear track detectors” 10th Int. Symp. on Radiat. Phys., Coimbra, Portugal, 17-22 Sept. 2006, to be published in Nucl. Instrum. Meth. A (2006), physics/0611105.

Reports, Internal Reports

1. OPERA Internal Note 77 (2006) “Measurement of the OPERA Lead α-radioactivity in Bologna”.
2. SLIM Internal Report 2006/1 “The Stranger-Rompicapo event/background”.